Michael Kügler

# Particle Detection and Experimental Evaluation of Different Material Combinations for Saturators of Particle Counting Devices

**MASTER'S THESIS**

to achieve the university degree of

Diplom-Ingenieur

Master's degree programme: Advanced Materials Science

submitted to

**Graz University of Technology**

Univ.-Prof. Mag.rer.nat. Dr.rer.nat. Alexander Bergmann

Institute of Electronic Sensor Systems

Graz, January 2018

## Affidavit

I declare that I have authored this thesis independently, that I have not used other than the declared sources/resources, and that I have explicitly indicated all material which has been quoted either literally or by content from the sources used. The text document uploaded to TUGRAZonline is identical to the present master‘s thesis.

Date

Signature

# Abstract

Air quality and the emission of particles has become a major concern over the last decade leading to stricter legislative requirements for vehicle type approval. To comply to such stricter regulations, improved measurement systems are required for exhaust analysis – especially regarding the determination of particle number (PN). A standard device to evaluate PN is a condensation particle counter (CPC). Current CPCs require an extensive pre-conditioning – including several heating and diluting steps – to remove volatile particles and comply with regulation, since only solid particles are regulated. By operating a CPC at high temperatures, volatile particles do not nucleate and the pre-conditioning becomes expandable. Hence, a more direct measurement of the aerosol is possible. This thesis contributes to such a high temperature CPC (HT-CPC) by addressing two obstacles in current research: On the one hand, it qualitatively examines the degradation of the working fluid during operation. Long term tests with different wick materials in two settings showed that the degradation can be minimized by using $N_2$ as carrier gas. On the other hand, the thesis covers the demand of a static light scattering setup that is an adequate detection method for measurements with a HT-CPC. Such a setup was realized and particle size estimations were successfully conducted with a condensation nuclei magnifier (CNM). First scattering measurements were also performed with the HT-CPC and the measured intensity is clearly tied to particle scattering. Future work should address the problem that the operation conditions of the HT-CPC could not be hold stable over time. Therefore, further modifications of the HT-CPC as well as the light scattering setup are necessary to obtain a more reliable measurement setup.

# Zusammenfassung

Der vermehrte Eintrag von Schadstoffen und Partikel in die Atmosphäre ist zu einem dringend zu lösenden Problem der Menschheit geworden. Mit immer strikteren Gesetzen und Vorgaben versucht man in vielen Bereichen die Emmissionen zu begrenzen. So wird etwa im Falle der Typisierung neuer Kraftfahrzeuge die maximal auszustoßende Partikelanzahl (PN) festgelegt. Um auch weiterhin die Vorgaben einhalten zu können, ist eine kontinuierliche Verbesserung der verwendeten Messsysteme notwendig. Momentan werden standardmäßig Kondensationspartikelzähler (CPC) zur PN-Bestimmung verwendet, die eine umfassende Vorkonditionierung des zu messenden Abgases voraussetzen. Mehrere Heiz- und Verdünnungsschritte sind notwendig, um – den Richtlinien entsprechend – volatilen Bestandteile zu entfernen und nur feste Partikel zu messen. Würde man einen CPC bei erhöhten Betriebstemperaturen verwenden, wäre eine solche Vorkonditionierung obsolet, da volatile Bestandteile nicht nukleieren könnten. Die vorliegende Arbeit trägt zur Entwicklung eines solchen Hochtemperatur-CPCs (HT-CPC) bei, indem sie sich mit zwei aktuellen Problemstellungen auseinandersetzt: Einerseits wurde der chemische Abbau des Betriebsmittel im Betrieb qualitative nachvollzogen. Langzeitmessungen mit verschiedenen Sättiger-Elementen zeigen, dass der Abbau unter Verwendung von $N_2$ als Trägergas minimiert werden kann. Andererseits wurde ein statischer Streulichtaufbau implementiert, der für die Detektion des Partikelstreulichts am HT-CPC geeignet ist. Damit wurden Partikelgrößen-Bestimmungen mit einem Nukleationskeimvergrößerer (CNM) durchgeführt. Auch erste Messungen mit dem HT-CPC sind erfolgreich und zeigen, dass die gemessene Intensität klar der Streuung von Partikeln zugeordnet werden kann. Allerdings muss die Betriebsstabilität des HT-CPCs zukünftig verbessert werden. Um einen verlässlicheren Messaufbau zu erhalten, sind daher Adaptionen des HT-CPCs als auch des Streulichtaufbaus notwendig.

# Acknowledgement

I want to thank Martin Kupper and Martin Kraft from CTR for bringing me in touch with this fascinating topic and for enabling this thesis.

Special thanks go to Alexander Bergmann and everyone at IES for providing a very nice working environment and support whenever needed.

This work was performed within the Competence Centre *ASSIC – Austrian Smart Systems Research Center*, co-funded by the Austrian Federal Ministries of Transport, Innovation and Technology (bmvit) and of Science, Research and Economy (bmwfw) and by the Federal Provinces of Carinthia and Styria within the COMET program.



Competence Centers for
Excellent Technologies

# Contents

# Index of Abbreviations

| | |
|---|---|
| **ADC** | Analog to digital converter |
| **CNC** | Condensation nuclei counter |
| **CNM** | Condensation nuclei magnifier |
| **CPC** | Condensation particle counter |
| **CSV** | Constant volume sampler |
| **DMA** | Differential mobility analyzer |
| **FPGA** | Field-programmable gate array |
| **FWHM** | Full width half maximum |
| **HEPA** | High efficiency particulate air |
| **HT-CNM** | High temperature condensation nuclei magnifier |
| **HT-CPC** | High temperature condensation particle counter |
| **L-Type** | L-shaped HT-CPC |
| **MFC** | Mass flow controller |
| **OPC** | Optical particle counter |
| **PEEK** | Polyetheretherketone |
| **PID** | Proportional-integral-derivative |
| **PM** | Particulate matter |
| **PMT** | Photomultiplier tube |

| | |
|---|---|
| **PN** | Particle number |
| **PTFE** | Polytetrafluoroethylene |
| **SPN** | Solid particle number |
| **T-Type** | T-shaped HT-CPC |
| **VPR** | Volatile particle remover |
| **XRF** | X-ray fluorescence spectroscopy |

# List of figures

# List of tables

# CHAPTER 1

# Introduction

Air quality and the emission of particulate matter (PM) has become a major concern over the last decade since it effects human health and the environment [6, 22, 24, 27, 43, 48]. PM as a blend of solid and liquid particles forms an aerosol when suspended in air/gas [15, p. 3] and is often invisible to the unarmed eye due to the size[1] of the involved particles. Only if particle concentration exceeds certain thresholds, it is commonly known as "fume, smoke, mist, fog, haze [...] or smog" [30, p. 3]. However, especially small invisible particles under 2.5 µm are regarded to be a health risk [25, p. 46, 27, p. 1, 45, pp. 2-9ff.]. Beside of natural emissions due to i.e. volcanic activities or biomass decomposition, anthropogenic emission – caused by e.g. industrial processes, domestic heating or traffic – influences the amount of PM in the atmosphere significantly [43, p. 417]. Once in the atmosphere, PM – depending on its size – can remain there from days to several weeks[2] [48, p. 2]. In this time particles are subject to atmospheric transport, can travel long distances and undergo various physico-chemical reactions[3] before showing an impact on health and environment [43, p. 417]. By establishing clean air policies and international strategies to reduce the emission of PM – e.g. agreements reached at the annual United Nations Climate Change Conference – governments worldwide try to improve air quality by limiting emissions [43, p. 417]. Along with stricter regulatory standards also measurement systems have to be improved to ensure that all standards are

[1] Unless otherwise stated the size of a particle refers to the particle's diameter in this text.

[2] In general, the smaller the particle, the longer it will remain in the atmosphere[4, p. 1329].

[3] In contrast to primary particles that are emitted directly into the atmosphere, so called secondary particle are formed from gaseous precursors – mainly "sulfur dioxide, nitrogen oxides, ammonia and non-methane volatile organic compounds" [47] in the atmosphere.

met [6, p. 937].

In the early 2000s, the PM emission was drastically reduced by the introduction of after-treatment systems in modern diesel vehicles [17, p. 50]. Consequently, the legislative requirement for vehicle type approval in regard of PM emission became insufficient. Therefore, the particle number (PN) was implemented as new regulatory metric over the last decade by EU as well as US legislation [17, p. 51].

However, defining a procedure that guarantees a reliable determination of the number of emitted particles is very challenging, since the size distribution of particles evolves over time and might depend on parameters that are difficult to control. Nanoparticles emitted by modern engines, do not form within the engine itself, but rather from emitted (gaseous) precursors in the exhaust during a non-linear gas-to-particle conversion process when the exhaust is cooled and diluted at the tailpipe [27, p. 2]. Volatile particles formed in this way, are prone to further conversion processes and their number in a sample is almost arbitrarily: Abdul-Khalek [1, pp. 7f.] found that the amount of emitted nanoparticles by engines can vary up to two order of magnitude, since the nucleation of particles strongly depends on the dilution ratio and temperature, the relative humidity, the used fuel and the residence time of the gaseous precursor in the dilution tunnel. In summery, PN of volatile material is difficult to assess and therefore, only the *solid* particle number (SPN) is currently relevant for vehicle type approval [17, p. 53].

However, SPN measurements require an extensive pre-conditioning of the exhaust to remove volatile components before the particle measurement with a CPC [11, p. 28]: In current measurement setups, the sample is taken from a quite cool position in a constant volume sampling (CSV) tunnel. Coarse particles are removed by a cyclone [5, p. 7]. To remove all volatile particles a so called volatile particle remover (VPR) unit is used [17, p. 52]. First the VPR dilutes the sample gas, then evaporates the volatile particles at temperatures up to 400 °C in a evaporation tube and finally dilutes the sample gas with cold filtered air once again to prevent re-nucleation [17, p. 52]. In this way, most of the volatile particle –forming the so called nuclei mode as explained later in detail – is removed [17, p. 53]. The cooled sample gas is eventually further diluted, before the particle concentration is measured by a CPC as shown in figure 1.1.

Despite this expensive procedure, volatile artifacts – most of them very small – can still remain and influence the measurement [11, p. 28]. To suppress these disturbances by small

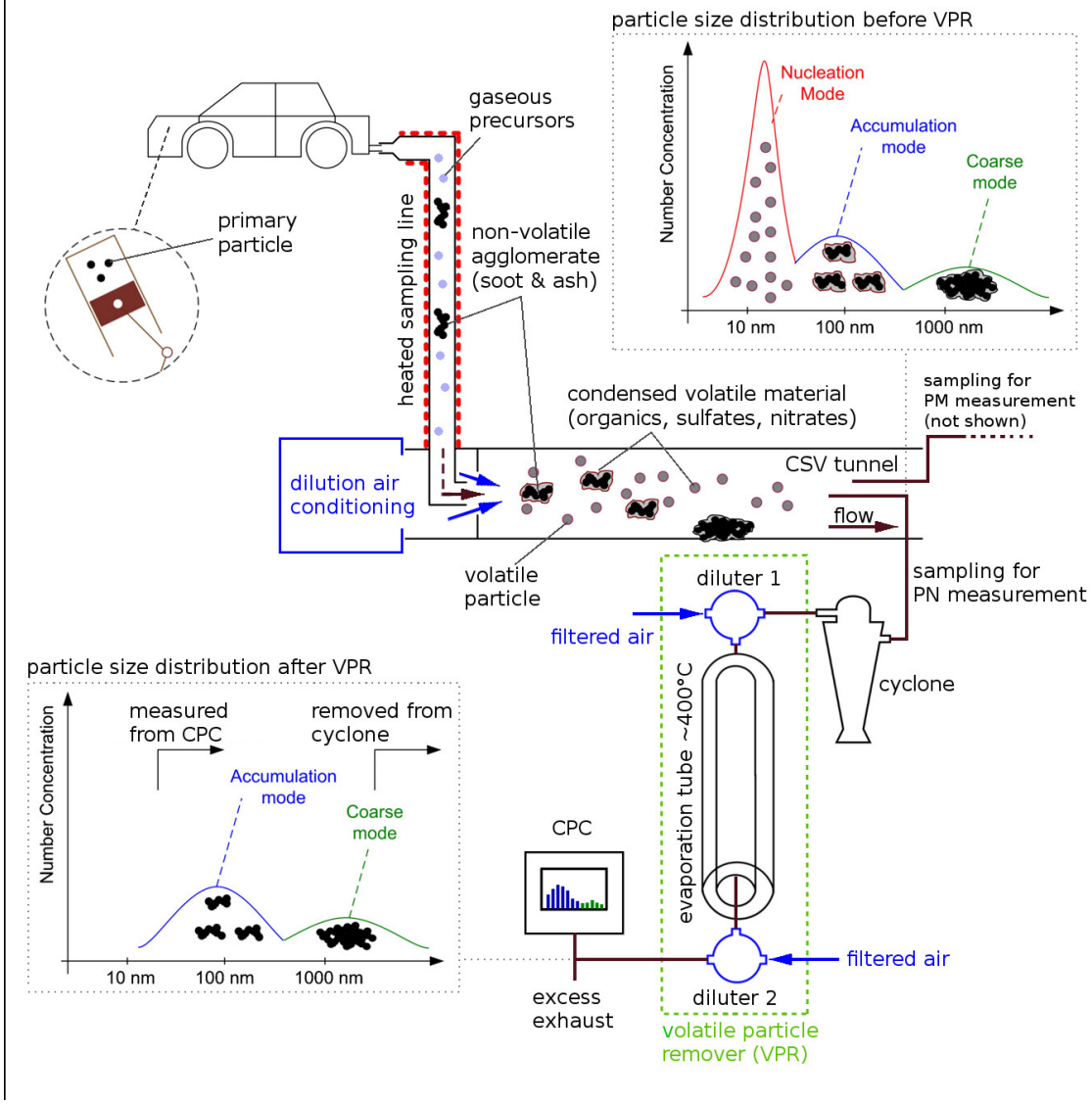


**Figure 1.1:** A typical exhaust setup for PN measurements: Primary non-volatile particles formed in an engine agglomerate on their way to the constant volume sampling (CVS) tunnel. There – due to cooling and diluting of the aerosol – volatile material condense on the present particles or volatile particle are formed from gaseous precursors. The aerosol for measurements is directly sampled from the CVS tunnel and a cyclone removes particles larger than 2.5 µm. A VPR removes all volatile particles by diluting the sample first, heating it up to around 400 °C to evaporate the volatile components and finally diluting it again to prevent re-nucleation. In this way, the nuclei mode consisting mainly of volatile particles is removed, as indicated by the two shown particle size distributions. In the end a CPC is used to measure the particle concentration. (Adapted from [16, p. 11], [5, p. 7] and [27, p. 2]).

volatile compounds as effectively as possible, a CPC with a cut-off mobility diameter of only 23 nm was stipulated by authorities [11, p. 28]. This, however, represents a major restriction, since possible solid particles below 23 nm are neglected [11, p. 28].

Due to this restrictions and shortcomings of the current PN measurement procedure, alternatives are in demand. A high temperature condensation particle counter (HT-CPC) might be a promising measurement approach in this regard. By operating a CPC at elevated temperatures, it is possible to ensure that gaseous precursors will not nucleate and form volatile particles, but stay in their vapor state instead. Hence, no expensive pre-conditioning is needed, since cooling and diluting can be restricted to a minimum.

## 1.1 Current research on high temperature condensation particle counter (HT-CPC)

A first attempt of a HT-CPC is described by Rongchai & Collings [38] in 2012[4]. Their device is operated at elevated temperatures, but follows the design of a classical conductive cooling CPC[5] as shown in figure 1.2. In contrast to the approach of a VPR – removing volatile particles by evaporation – the idea of the HT-CPC is to prevent (re-)nucleation by directly sampling hot exhaust of 400 °C. Thereby, it is not necessary to operate the device itself at this temperature, since temperatures around 150 °C to 200 °C should be sufficient to prevent re-nucleation of volatile particles [11, p. 28]. Experimental tests with volatile tetracontane and non-volatile NaCl particles proved that the HT-CPC successfully removed 99 % of all volatile particles [39, p. 3].

Due to the elevated temperatures, an adaption of certain components of the CPCs as well as a different choice of working fluid is necessary: As shown in figure 1.2, Collings et al. [11] used a diesel particle filter as saturator element to saturate the $N_2$ or filtered air carrier gas flow. The aerosol was directly injected into the thermally separated condenser. The detection was done with a thermally separated optical particle counter (OPC) unit from a TSI 3034 SMPS system at a temperature of 45 °C[6]. Although no long-term testing was done, initial experiments with working a prototype looked promising [39, p. 3]. Additionally, several potential working fluids that withstand temperatures up to 300 °C

[4] The work of Rongchai & Collings on this HT-CPC is also described in [39] and [11].

[5] A conductive cooling CPC is one of the main CPC designs as described in chapter 2.3 in more detail.

[6] A sheath flow of filtered air prevents condensation in this case. In general, the optical unit should be at least at the same temperature as the saturator to prevent condensation effectively [11, p. 30]. The laser focus was approximately 1.5 mm above the exit nozzle.

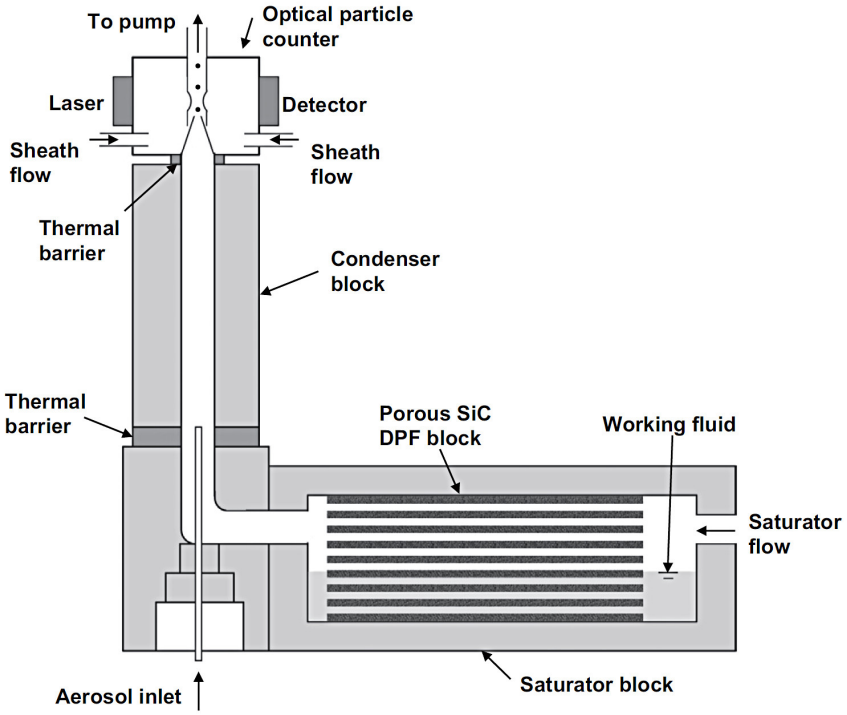


**Figure 1.2:** Schematic of the HT-CPC designed by Rongchai & Collings [11, p. 29].

were identified [11, pp. 33f.].

In 2016, Kupper et al. [32] presented two designs of high temperature condensation nuclei magnifiers (HT-CNM) that operate at 150 °C to 200 °C. Both devices – one with L-shaped (L-Type) and one with T-shaped (T-Type) geometry – are described in chapter 3.1 below in more detail. Computational fluid dynamics simulations showed "very good gas saturation in the saturator and few aerosol particle losses due to wall contacts in both geometries" [32]. Moreover, the simulation showed that with $\Delta T_{condensor-saturator} = 10\,°C$ a cut-off diameter of 10 nm should be possible. Experiments with functional demonstrators and an organic working fluid proved that heterogeneous nucleation occurs and that the scattering of laser light was observable without optical aids [32]. A more precise determination utilizing static light scattering was attempted but failed due to reflective interferences of stray light. Besides, the working fluid as well as the wick material showed degradation over time as shown in figure 1.3.

This thesis addresses the two mentioned obstacles reported by Kupper et al. [32]. Firstly, since further investigation in regard to the observed degradation is necessary, results of degradation experiments with several potential wick materials are provided in chapter 4.3. Secondly, due to the fact that the used static light scattering setup proved to be inadequate

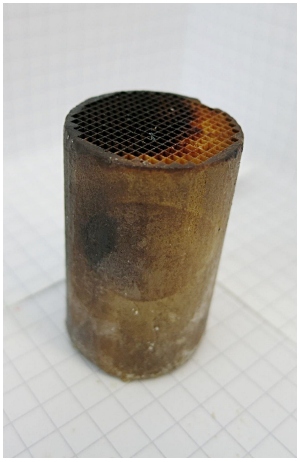

**Figure 1.3:** Picture of a cordierite wick after approximately 7 h of use [32].

for a HT-CPC, a new setup was implemented as presented in chapter 4.4. In addition, to reduce leakage during operation, modifications of the HT-CPCs were made as presented in chapter 4.1.

# CHAPTER 2

# Basics

## 2.1 Particulate emission

Since road traffic – especially in urban areas [43, p. 423] – is one of the main sources of PM[7] and the regulations on emission limits for modern vehicles are extensive – as EU regulations [13] show – this section can only give a short overview on particulate emission related to traffic. To comply EU legislation modern vehicles nowadays are equipped with after-treatment systems like diesel particulate filter. These filters are designed to remove up to 95 % of particles from the exhaust of a vehicle, reducing the emitted particle mass significantly [43, p. 458]. However, most of the remaining particles emitted by vehicles are in the low sub-micrometer range (see figure 2.1) – not only imposing a health risk and being invisible to the unarmed eye and also difficult to detect[8] [6, p. 937].

Particles emitted by modern diesel engines are typically log-normally distributed in size with three clearly distinguishable modes [26, p. 577, 27, pp. 2f. 28, p. 3] as illustrated in figure 2.1. Also for the so called urban aerosol, which is "found in the lowest kilometer of the atmosphere over large cities", [22, p. 307-312] comparable modes were identified:

**Nucleation mode:** The nucleation or nuclei mode contains mainly volatile particles rang-

[7] Beside soot particles from exhaust, also diffuse emission like abrasion from e.g. brakes or tires or dispersed PM by the slipstream of a vehicle has to be taken into account. [43, p. 423]

[8] This is especially critical in case of regular check-ups, since the efficiency of after-treatment systems can degrade over time due to wearout [6, p. 937]. For instance, in case of diesel particle filters regular regeneration is necessary to avoid clogging and flow restriction by the filter, where high PM emission might occur [43, pp. 427,458]. Hence, EU legislation has implemented an additional test to ensure the agreement with emission standards. [43, p. 427]

ing in size from 3 nm to 30 nm and "consist of metallic compounds, elemental carbon and semi-volatile organic and sulfur compounds that form particles during exhaust dilution and cooling" [27, p. 2]. 90 % of all particles but only 0.1 % to 10 % of the total particle mass can be found in this mode [28, p. 3]. Despite the low mass fraction, but due to the high surface area of these particles, harmful substances can bind easily to them [43, p. 424]. However, these particles tend to coagulate rapidly with each other or with particles in the accumulation mode due to their high number [22, p. 311]. Since most of the volatile particles are formed during cooling and diluting from gaseous precursors, this mode is very sensitive to those processes [28, p. 9]. Consequently, "this mode is not always present [in urban aerosol], but is usually found near highways and other sources of combustion" [22, p. 311].

**Accumulation mode:** In this mode particles "composed primarly of carbonaceous agglomerates and adsorbed materials" [27, p. 2] with a size between 30 nm and 500 nm can be found. They make up most of the exhaust total particle mass.

**Coarse mode:** Particles larger than 1000 nm often form from accumulation mode particles that are deposited on exhaust system or cylinder surfaces and formed clusters. They contribute about 5 % to 20 % to the total particle mass. [26, p. 577]

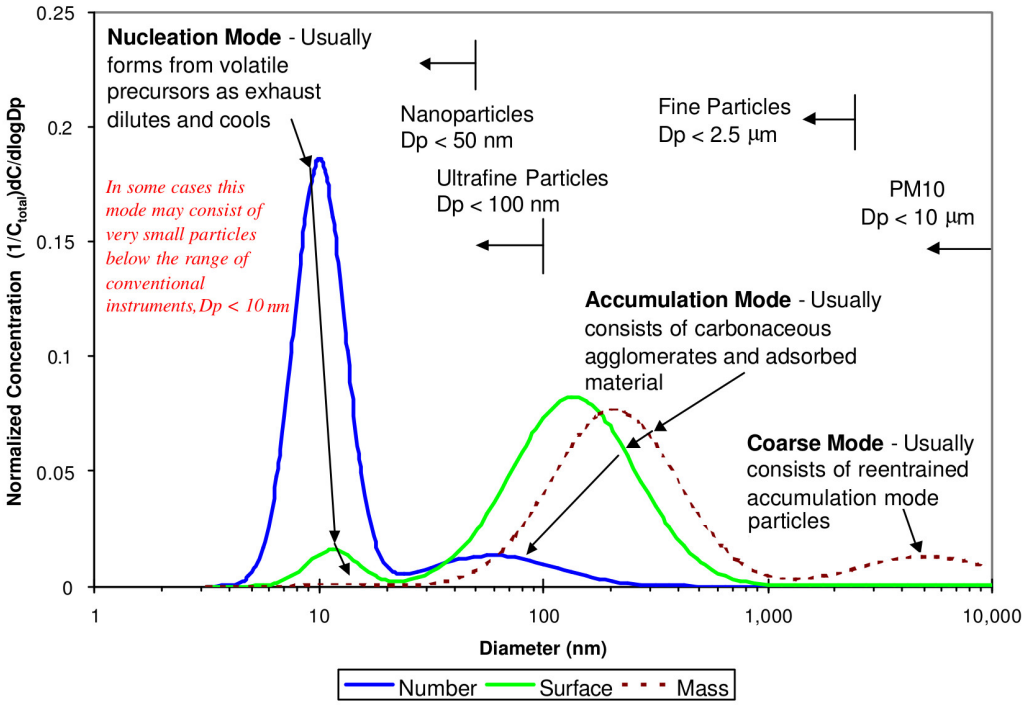


**Figure 2.1:** Typical particle size and mass distribution of diesel engine exhaust; $D_p$...particle diameter, $C_{total}$...total particle concentration (adapted from [28, p. 4]).

In addition, figure 2.1 indicates the commonly used size definition of atmospheric particles[9]. As shown most of the particles emitted by engines are actually significantly smaller than the 2.5 µm that regarded to be a health risk. They are commonly classified as followed [4, 15, 28, 43]:

| | |
|---|---|
| $d_{aero} < 10\,\mu m$ | PM10 – Particles |
| $d_{aero} < 2.5\,\mu m$ | PM2.5 – Fine Particles |
| $d_{aero} < 100\,nm$ | Ultrafine Particles |
| $d_{aero} < 50\,nm$ | Nanoparticles |

Unfortunately, a depiction like in figure 2.1 suggests that the size distribution is more or less static, but naturally it changes over time and strongly depends on environmental settings [15, p. 23]. Several processes – as illustrated in figure 2.2 – lead to a modification of the size distribution in a given volume: On the one hand, particle diffusion and sedimentation involves a particle flux from and to another volume. On the other hand, coagulation, nucleation and growth occur inside the volume itself. Especially, very small particles associated with the nucleation mode are prone to conduct such modifications. Moreover, in particular the gas-to-particle conversion of gaseous precursors in the exhaust is highly sensitive to cooling and dilution conditions at the tailpipe [27, p. 2].

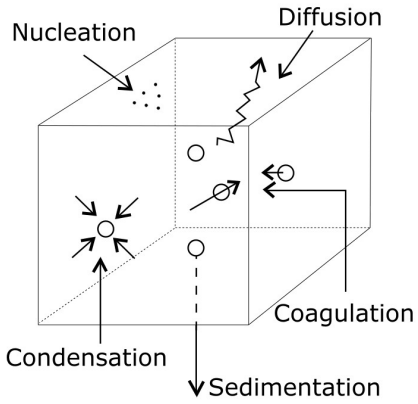


**Figure 2.2:** Processes that modify the particle size distribution within an aerosol volume [15, p. 23].

[9] Note that the size definition is valid for spherical particles only. In case of nonspherical particles it applies to an equivalent diameter, in this case the aerodynamic diameter $d_{aero}$. The aerodynamic diameter of a particle "of any shape, chemical composition and density is equal to the diameter of a sphere with the density of $1\,g\,cm^{-3}$, which has the same settling velocity in air as the particulate being analyzed" [43, p. 421].

## 2.2 Particulate matter measurement

Two parameters are important to evaluate PM. On the one hand its size distribution and on the other hand its concentration. Instruments and methods[10] to measure these two parameters are shown in figure 2.3.

In case of PM concentration, the gravimetric determination of particle mass was the standard technique for a long time [17, p. 50]. However, in modern vehicles – as indicated above – most of the particulate mass is successfully removed by after-treatment systems and the remaining particles emitted by engines are actually significantly smaller than the 2.5 µm, the size that regarded to be a health risk [25, p. 46, 27, p. 1, 45, pp. 2-9 to 2-17]. Consequently, it is very difficult to reliable assess the remaining particle mass – due to its small amount – with conventional gravimetric measurement techniques [17, p. 50, 6, p. 937]. Therefore, PN as an additional metric in emission legislation emerged and is becoming more important ever since [17, p. 50, 27, p. 1, 43, p. 427].

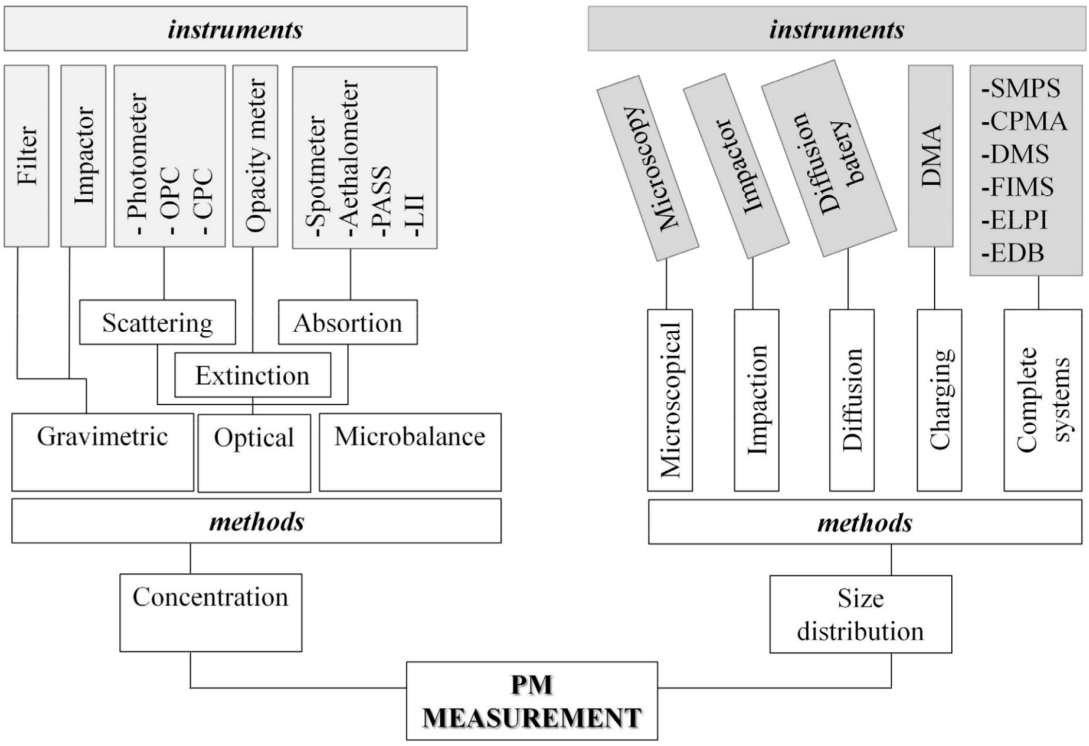


**Figure 2.3:** Instruments and methods for particle measurement [4, p. 1330].

To acquire PN – especially in cases of ultrafine particles – a CPC utilizing light scattering

[10] A quick overview of these instruments can be found in [4] and [17].

is often used[11] [9, p. 381]. This method is discussed in more detail in the following chapters.

## 2.3 Condensation particle counter (CPC)

The basic technique behind a CPC[12] has been around for over a century now[13] and has its origin in the work of P. J. Coulier from 1875 and of J. Aitken from 1880 [41, p. 243]. The latter also reported the first known CPC in 1888 [17, p. 64]. Since small aerosol particles are difficult to detect by optical means, their size is artificially increased by condensational growth and thereby allowing an optical measurement [33, p. 298]. In principle, an aerosol – particles suspended in a carrier gas – is introduced into an atmosphere, which is supersaturated with a working fluid/vapor, which is most often water or an alcohol like *n*-Butanol. In this supersaturated atmosphere, heterogeneous nucleation of the working fluid takes place. Thereby, the particles act as condensation nuclei[14] [2, p. 249, 18, p. 24].

There are several ways to reach the required supersaturated atmosphere. Based on these ways, CPCs are commonly classified in literature [9, p. 384, 33, p. 384] as followed:

**Expansion:** Until 1975, all commercial CPCs used adiabatic expansion [17, p. 64]: An aerosol stream is first saturated with water at room temperature and then cooled by sudden volume expansion in an expansion chamber [9, p. 384]. Due to the cooling the dew point shifts and thus a supersaturated environment is formed. One of the major disadvantages of expansion-type CPCs is its step-wise processing mode, which is not complying well with steady-state flow requirements. Four steps are repeated over and over: First taking the aerosol sample, second expanding, third particle grow and fourth detection. This leads to an unsteady flow and therefore this methods is out of use [2, p. 249].

**Conductive cooling:** Since there are cases where a steady-state flow is required – e.g. in combination with a differential mobility analyzer (DMA) – continuous-flow CPCs

[11] In addition, electrical mobility techniques – for instance a differential mobility analyzer (DMA) – are commonly employed to determine the particle size distribution [9, p. 381].

[12] Instead of CPC also condensation nuclei counter (CNC) is used synonymously in literature [33, p. 298].

[13] An overview over the history of the CPC can be found in [33] as well as in [41].

[14] According to Giechaskiel et al. [18, p. 21] heterogeneous nucleation theory applies, if the particle is insoluble. In addition, the supersaturation has to be low enough to avoid homogeneous nucleation. A short mathematical introduction to heterogeneous condensation can be found in [15, p. 283f.].

were developed. One way to achieve such a CPC is by the principle of conductive cooling. Sinclair and Hoopes in 1975, Bricard et al. in 1976, and Agarwal and Sem in 1980 designed very similar conductive cooling-type CPCs [2, p. 249, 9, p. 386]. Modern CPCs used in automotive industry are still based on their designs [17, p. 64]. As shown in figure 2.4, there are three core elements used in their setups: Saturator, condenser and particle detector.

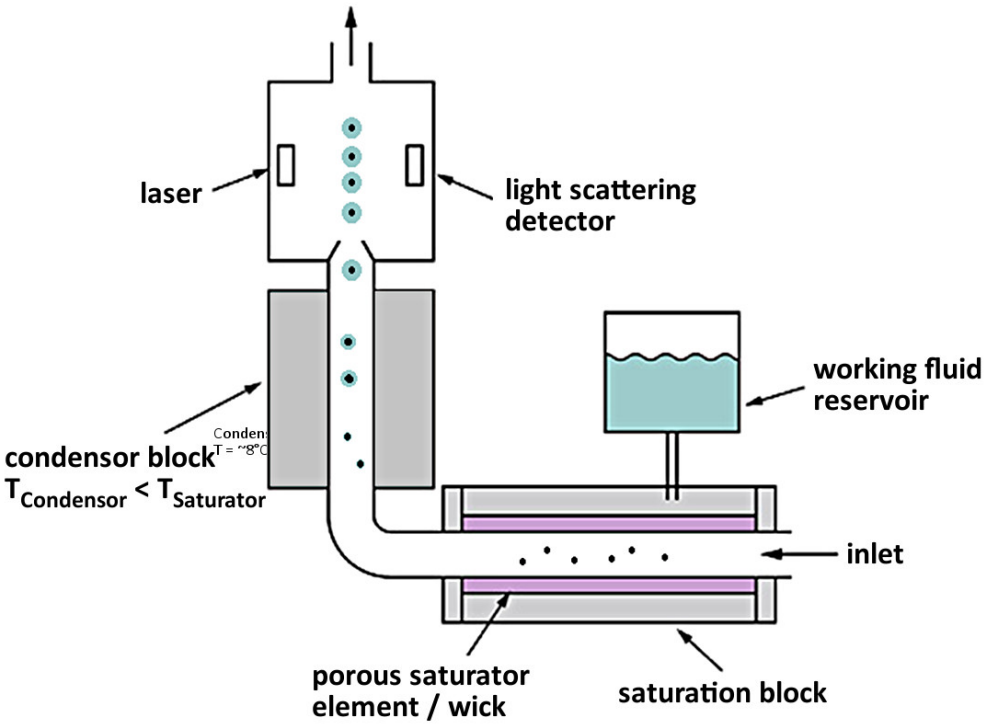


**Figure 2.4:** Schematic of a conductive cooling CPC; adapted from [8].

First the aerosol is introduced into a saturator, where it will be saturated with a working fluid (typically $n$-Butanol) at a given temperature $T_{saturator}$. In many cases a saturator element, also called wick[15] – made of a porous material – is used to guarantee a quick saturation. By passing it to a cooled condenser with a temperature $T_{condensor} < T_{saturator}$, the aerosol is cooled down by thermal conduction and it becomes supersaturated. In this supersaturated region of the CPC, condensational growth of the particle can take place. However, the activation of a particle for condensational growth is not trivial[16], since it depends on various parameters. These include the geometry of the CPC and all settings that influence the supersaturation

[15] In this work *wick* and *saturator element* are used interchangeable.

[16] This is true for all CPC designs. As stated by Ahn and Liu [3, p. 270], the activation efficiency of a CPC and its counting efficiency can be seen as equivalent, due to the fact that if a particle is activated it always grows into detectable size.

like temperature, flow rates/residence time etc. In addition, the spatial distribution of the supersaturation in the condenser tube as well as the chemical composition of the particle itself plays a role. [2, 9, 18] In general, a numerical simulation of the specific growth conditions by solving the heat and mass transfer equation – as done for instance by Ahn & Liu [2] or Giechaskiel et al. [18] – is necessary to get full control over the working conditions of a CPC. The described design of conductive cooling is limited to working fluids with a mass diffusion coefficient smaller than the thermal diffusivity of the aerosol – in case of air as carrier gas smaller than $2.0 \times 10^{-5}\,\mathrm{m\,s^{-1}}$. Otherwise, the working fluid molecules would diffuse faster towards the condensor wall than they would get cooled down. Consequently, the working fluid gets depleted in the middle of the condensor and a supersaturated atmosphere is hardly reached [9, p. 387]. This is the case, if water is used as working fluid in a conductive cooling CPC. Due to its diffusion coefficient of $2.4 \times 10^{-5}\,\mathrm{m\,s^{-1}}$ the $H_2O$ molecules diffuse faster than the heat is dissipating.

**Differential diffusion:** The differential diffusion CPC – developed by Hering and Stolzenburg in 2005 – employs the higher mass diffusion coefficient of water by inverting the operation principle of the conductive cooling CPC: A cold – with water vapor saturated aerosol – is passing through a tube with warm wet walls. Due to the above mentioned difference of diffusion coefficients, $H_2O$ molecules diffuse quickly into the aerosol stream, while the heat transfer is slower. Consequently, a region of high supersaturation evolves in the middle of the tube. [9, p. 387]

**Mixing-type:** As the name indicates this type combines two saturated gas streams to reach a supersaturated state for particle growth. Therefore, there are less constraints regarding working fluids and higher flow rates, up to $14\,\mathrm{L\,min^{-1}}$ are possible [33, p. 314]. Hence, it allows high response rates [9, p. 388]. Despite these advantages, mixing-type CPCs are still quite uncommon in automotive industry [18, p. 64]. However, as McMurry [33, p. 312-314] describes, there are several approaches that differ in concrete realization in terms of temperature settings, working fluid etc.

### 2.3.1 Performance of condensation particle counters (CPCs)

Currently, the measurable particle size[17] of commercial CPCs range from 1 nm to a few micrometers depending on the type [11, p. 29, 44, p. 2]. Regardless which CPC design is used one of the main challenges is to grow the particle droplets just to the right size, i.e. an optically detectable size, because larger droplets tend to get lost by impaction and sedimentation [33, pp. 308f.]. However, at the outlet of the condenser tube – commonly a focusing nozzle in some kind – the droplets have to be big enough to be detected by light scattering. Therefore, particle droplets are grown to a range of 2 µm to 15 µm. The final droplet size in a conductive cooling CPC is influenced by the thermal diffusivity of the used carrier gas[18] and the traveling distance in the condenser [2, pp. 256f.]. In addition, also the flow rate affects the particle size, since it controls the time a particle remains in the condenser [2, p. 260]. Due to the condensational growth process the droplet size at the outlet nozzle tends to be near-uniformly distributed [9, p. 383].

To ensure comparability between measurements with different devices, a calibration process is performed by using a defined number of monodisperse particles from a particle generator. The measured particle concentration $N$ – typically expressed as [particles/cm$^{-3}$] – is calibrated with the readout of an aerosol electrometer in combination with a DMA [9, pp. 389f, 33, pp. 316f.]. Thereby, also the counting efficiency $\eta_{count}$ of the CPC for different particle sizes $d$ is determined [18, p. 27]:

$$\eta_{count}(d) = \frac{N_{detected}(d)}{N_{in}(d)} \cdot 100\,\% \tag{2.1}$$

The so called cut-off diameter $d_{50}$ [9, p. 390] refers to the particle diameter for which a CPC shows a counting efficiency of

$$\eta_{count}(d_{50}) = 50\,\% \tag{2.2}$$

According to EU legislation this cut-off diameter should be $d_{50} = 23\,\text{nm}$ for automotive aerosol measurement setups [17, p. 64].

[17] As Cheng concludes, the minimal size is strongly determined by "the particle solubility in condensing vapor, the wettability of the particle surface, and the charge state of the particle surface" [9, p. 390].

[18] As shown by Ahn and Liu [2, p. 257], in case of helium as a carrier gas the supersaturation in the condenser tube is reached quite fast due to its high thermal diffusivity coefficient. Therefore, the droplets grow significantly faster and bigger compared to air or argon as a carrier gas.

### 2.3.2 Characteristics of conductive cooling condensation particle counter in literature

This chapter is focused on conductive cooling CPCs and their features found in literature, since all devices used in this work belong to that group.

As already mentioned above, due to the temperature difference between saturator and condenser a supersaturated region within the condenser emerges. As Liu & Ahn [2, p. 254] as well as McMurry [33, p. 311] indicate, the setting of the condenser temperature $T_{condensor}$ has a clear influence on the detectability of small particles: If $T_{condensor}$ decreases, smaller particles can be activated, since a higher peak saturation in the condenser – that is also closer to the condensor inlet – is reached. The same is true for an increasing saturator temperature $T_{saturator}$: If $T_{saturator}$ increases also the activation efficiency for small particle increases [2, p. 254]. These findings also coincide with simulations done for one of the used HT-CPC geometry as shown in figure 2.5.

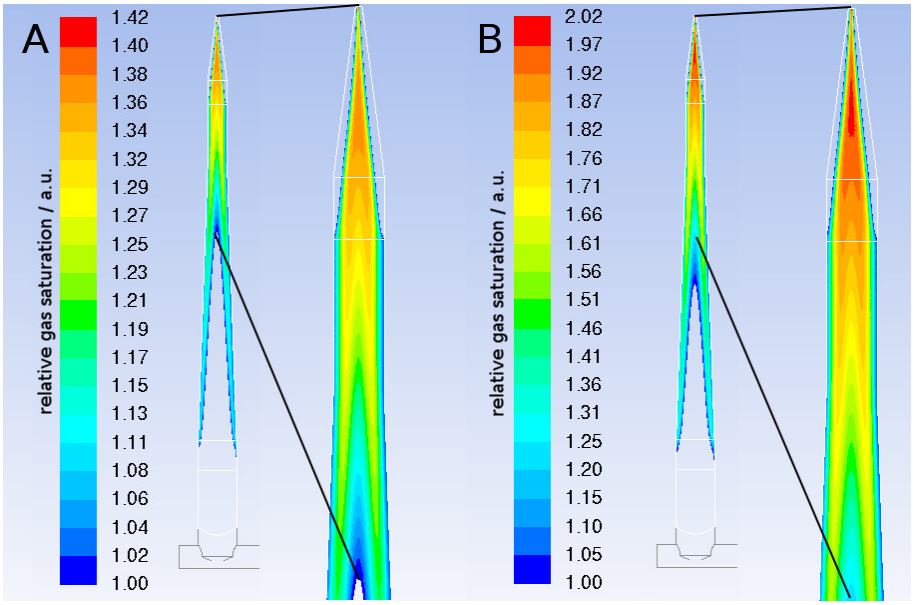


**Figure 2.5:** Relative saturation in the condenser tube of the L-Type HT-CPC according to simulations (rotationally symmetrical). A) $T_{condensor} = 171\,°C$, B) $T_{condensor} = 181\,°C$ [31].

Due to its design, conductive cooling CPCs are prone to the loss of particles: Diffusional deposition, sedimentation, impaction as well as incomplete activation of particles – due to variations in the saturation profile[19] within the condensor – influences the counting

[19] As shown in figure 2.5 the saturation is maximal at the center of the condenser tube and decreases radially to the wall. Due to this inhomogeneous distribution, the activation – especially in case of small particles – is not complete. [9, p. 386].

efficiency [9, pp. 386 & 390, 33, p. 318, 46, p. 856]. In general, the diffusion losses increase with decreasing particle size [9, p. 390]. However, as Wang, Flagan and Seinfeld [46, p. 856] illustrate, the geometry of the device is very important: Additional bends in a device's tubing, for instance, significantly increase diffusional loss. Furthermore, diffusional loss at the sampling inlet has been reported [33, p. 318]. Giechaskiel et al. [18, p. 27] estimate that these effects in summary lead – independently of the measured particle size – to a decrease of the maximal counting efficiency of 1 %.

## 2.4 Optical particle detection

In aerosol measurement optical methods are well established, because they allow an easy and non-intrusive characterization of the particles in an aerosol regarding their "size, morphology, [...] concentration [...] and the dynamics of their motion, aggregation, or dissipation" [40, p. 270]. To gather this information, aerosol particles are illuminated by electromagnetic radiation – in many cases a visible light beam. Light interacts with matter in several ways: It might get absorbed, scattered or just change the direction of its polarization [37, p. 4].

As shown in Giechaskiel et al. [17, p. 4] aerosol measurement instruments utilize both absorption and scattering of light in different ways. Commercial CPCs use light scattering to detect particle, hence the emphasis of this chapter is on this topic. A basic distinction for light scattering in general is based on the energy conservation during the scattering process: If the scattered photons have the same energy as the ones of the incident light beam, they are scattered elastically; otherwise – in case their energy is different – inelastic scattering takes place [37, p. 4]. In case of CPCs only elastically scattered light is detected by static light scattering technique [17, p. 64]. Thereby, the average intensity[20] of the scattered light at certain scattering angles is used to derive information about "molecular weight, particle size, particle shape and particle interactions" [37, p. 7]. A simple measurement setup is depicted in figure 2.6 [37, p. 13]. As shown a light source illuminates a sample e.g. an aerosol stream. Light is scattered in all directions and will be detected in the scattering plane [21] under a certain scattering angle $\theta$ with

[20] Beside of static light scattering so called dynamic light scattering technique is used: Based on temporal fluctuations of the intensity of the scattered light it is possible to derive information about e.g. diffusion coefficient [37, p. 7].

[21] The light will be scattered in all directions, but most experimental setups are confined to the scattering plane and therefore the second scattering angle is typically set to $\phi = 90°$ [40, p. 272].

a photomultiplier tube (PMT) or a photodiode as detector. In most cases apertures or slits define the detector's area of vision. Hence, it can only observe a cylindrical volume of diameter $d_2$. This volume intersects with the light beam that can also be assumed to be cylindrical with diameter $d_1$. This intersection is the origin of detected scattered light and is commonly referred to as the scattering volume $V_S$.

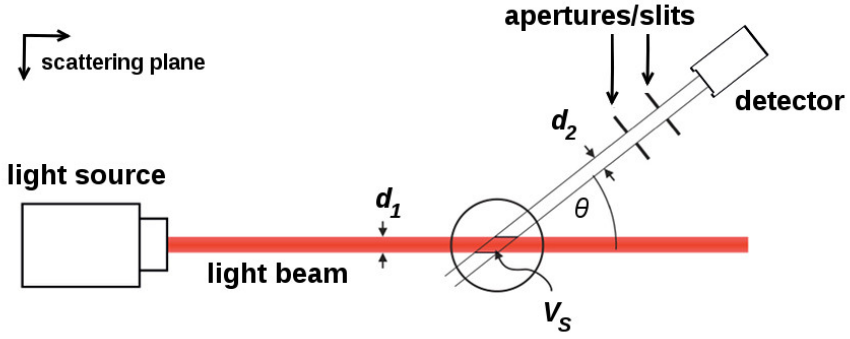


**Figure 2.6:** Basic light scattering setup. The detector observes scattered light that origins in the scattering volume $V_S$ (adapted from [37, p. 6].

For quantitative light scattering – especially for particle size determination – there are some demands on the light source [37, pp. 10f.]: The incident light beam should be highly collimated – to reduce stray light and reflections – as well as monochromatic, since scattering is dependent on the wavelength [6, p. 939]. Lasers can meet these demands and provide such radiation – even with a distinct direction of polarization – with high intensities [37, p. 11]. Usually, the incident light is set to be vertically polarized along the z-direction –perpendicular to the scattering plane – and the vertical polarization of the scattered light is detected[22] [40, p. 272]. Furthermore, in case of spherical particles, the polarization of the light is preserved [19, p. 4].

When an incident light beam with intensity $I_0$ hits a particle, the scattered intensity is given by:

$$I = I_0 \underbrace{\frac{dC_{sca}}{d\omega}}_{\substack{\text{differential} \\ \text{cross section}}} \frac{1}{r^2} \tag{2.3}$$

As shown in the equation 2.3, the scattered intensity depends directly on the differential cross section $\frac{dC_{sca}}{d\omega}$. In general, it includes dependencies on the scattering angle $\theta$, the

[22] This is sometimes indicated by indices: For instance in case of the intensity $I_{vv}$, the first subscript refers to the incident polarization and the second one to the measured polarization [40, p. 272]. Note that in this work, all equations – especially the differential cross sections – will be stated for the scenario $I_{vv}$. For other measurement setups the equations may vary.

wavelength $\lambda$ as well as the particle size $d$. The particular expressions are provided by solutions to Maxwell's equations as presented for instance by Rayleigh or Mie theory [40, p. 276].

### 2.4.1 Rayleigh theory[23]

To solve Maxwell's equations Rayleigh theory incorporates certain approximations, mainly based on the fact that only spherical particles of radius $a$ are taking into account that are small compared to the wavelength $\lambda$ of the incident light. To be more precise, for Rayleigh theory to apply, the size parameter $\alpha$ defined as

$$\alpha = 2\pi a/\lambda \tag{2.4}$$

and the quotient of the refractive indices $m$ defined as

$$m = \frac{n_{particle}}{n_{medium}} \tag{2.5}$$

have to fulfill the following conditions:

$$\begin{aligned} \alpha &<< 1 \\ m\alpha &<< 1 \end{aligned} \tag{2.6}$$

In this case Rayleigh scattering takes place and the differential scattering cross section is expressed by:

$$\frac{dC_{sca}}{d\omega} = k^4 a^6 |\frac{m^2 - 1}{m^2 + 2}|^2 \tag{2.7}$$

Thereby the wave number $k$ is given by:

$$k = 2\pi/\lambda \tag{2.8}$$

As indicated the differential scattering cross section is independent of the scattering angle $\theta$ and therefore the scattered intensity $I_{vv}$ in the Rayleigh regime is isotropic. Furthermore, with $a^6$ and $\lambda^{-4}$ there is a strong dependence on the particle size and on the wavelength. $I_{vv}$ increases as the particles become coarser and as the wavelength of the incident light decreases. Since Rayleigh theory applies only for a very small particle, all scattered light travels the same distance to the detector, hence no phase difference is observed.

[23] If not otherwise stated, this section follows the explanations of Sorensen et al. [40, pp. 272-274].

### 2.4.2 Mie theory[24]

When the particle size and the refractive index are arbitrary the approximations that led to Rayleigh theory do not apply anymore and the exact solution of Maxwell's equation is relevant. Gustav Mie provides such a solution for spherical particles in 1908 [6, p. 937].

To illustrate the results of Mie theory and to plot the differential scattering cross section, it appears practical to introduce the scattering wave vector $\boldsymbol{q}$ as depicted in figure 2.7B. In case of elastic scattering, the scattered light changes only its direction as indicated by the scattering vector $\boldsymbol{q} = \boldsymbol{k_{in}} - \boldsymbol{k_{out}}$ (figure 2.7B). Since the wavelength remains the same, the following applies:

$$|\boldsymbol{k_{in}}| = |\boldsymbol{k_{out}}| = k = \frac{2\pi}{\lambda} \tag{2.9}$$

Therefore, as illustrated by figure 2.7C, the length of the scattering vector is given by:

$$q = \frac{4\pi}{\lambda} sin(\theta/2) \tag{2.10}$$

With this variable it is possible to plot the normalized intensity $\frac{I(\theta)}{I_0}$ - and with it the Mie scattering cross section – as function of the product $qa$ as shown in figure 2.8A for different particle sizes – i.e. $ka$-values. In comparison to figure 2.8B, the advantage is clear: In this diagram the normalized intensity plotted as function of the scattering angle $\theta$ shows no clear pattern, whereas the left plot as function of $qa$ does. In general, the scattering intensity decreases with increasing $qa$. At small $qa$ most of the incident light is forward scattered leading to a quasi-flat region of high intensity until around $qa \approx 1$. There the intensity starts to decrease to a first local minimum. This descent can be described by the Guinier approximation and it provides information about the size of the involved particle as explained later on in chapter 2.4.4. The remaining curve shows the typical Mie ripples structure that is clearly visible if the particles are monodisperse: Due to phase differences in case of highly symmetrical particles – e.g. as here depicted spherical particles – the scattered light shows local intensity minima and maxima [37, p. 46]. At large $qa$ distinct spikes near $2ka$ indicate backscattered light – i.e. the scattering glory. Overall, Mie

[24] If not otherwise stated, this section follows the explanations of Sorensen et al. [40, pp. 274-278.].

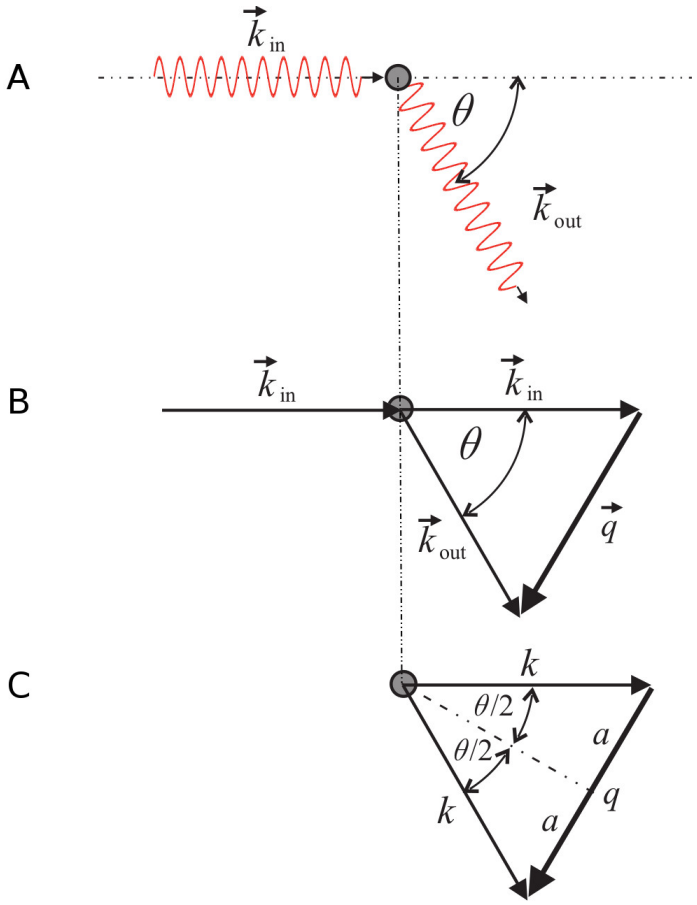


**Figure 2.7:** A) In case of elastic scattering the wave vector of the incoming light $\boldsymbol{k_in}$ changes only its direction but not its wavelength, hence $|\boldsymbol{k_{in}}| = |\mathbf{k_{out}}| \equiv k = \frac{2\pi}{\lambda}$. B) The scattering vector is defined as $\boldsymbol{q} = \boldsymbol{k_{in}} - \boldsymbol{k_{out}}$. C) The length of the scattering vector can be expressed as $q = \frac{4\pi}{\lambda} sin(\theta/2$ (adapted from [37, p. 26]).

scattering follows approximately power laws in three distinguishable intervals:

$$I \propto (qa)^0 \qquad \text{for} \quad qa < 1 \tag{2.11}$$

$$I \propto (qa)^{-2} \qquad \text{for} \quad 1 < qa < 2\alpha|m-1| = \rho \tag{2.12}$$

$$I \propto (qa)^{-4} \qquad \text{for} \quad qa > \rho \tag{2.13}$$

Thereby, the so called phase shift parameter $\rho$ represents the phase difference between a light wave that travels across a particle and one that travels solely through the medium.

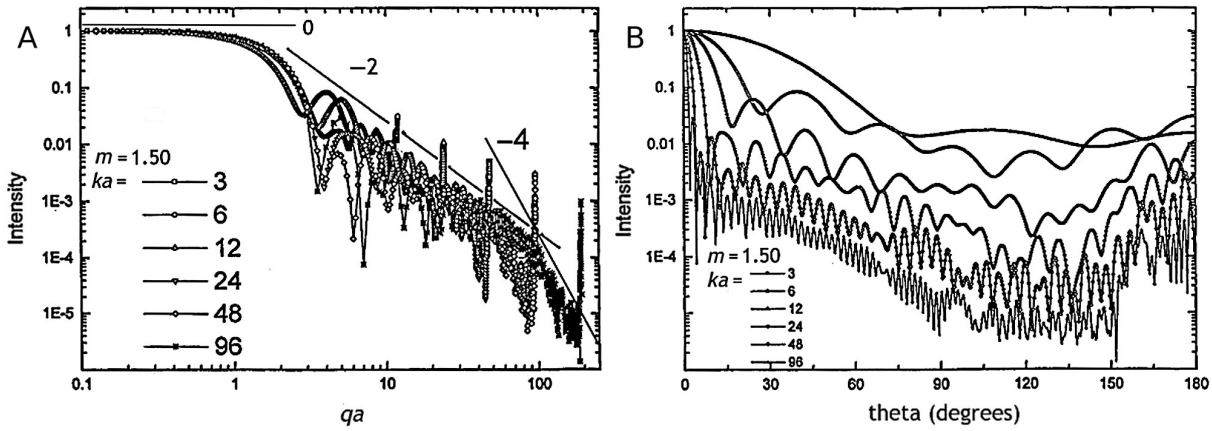


**Figure 2.8:** Normalized Mie scattering intensity for spherical particles of the size $ka$ and with a relative refractive index of $m = 1.5$ plotted against (A) $qa$ and (B) scattering angle $\theta$. Only the plot A shows an overall pattern and the power laws are indicated with 0, -2 and -4. (adapted from [40, p. 276].

### 2.4.3 Determination of particle size – minimum method[25]

It is possible to determine the size of the particles within an aerosol – if they are identical in size and shape – by measuring the scattering intensity at different scattering angles $\theta$ and hence for different $qa$. The relation between scattering intensity and particle size can be established by the so called form factor $P(q)$. On the one hand, it is defined as the normalized scattering intensity:

$$P(q) = \frac{I_s(q)}{I_s(0)} \tag{2.14}$$

The scattering intensity $I_s(q = 0)$ – i.e. for $\theta = 0°$ – is not directly measurable, since the high intensity of the primary laser beam interferes. Hence, $I_s(0)$ has to be extrapolated in general.

[25] If not otherwise stated, this section follows the explanations of Øgendal [37, pp. 43-68].

On the other hand, the form factor for an arbitrary molecule with $n$ identical point-like subunits can be also expressed by:

$$P(q) = \frac{1}{n^2} \sum_{j=1}^{1} \sum_{k=1}^{1} \frac{sin(qr_{jk})}{qr_{jk}} \tag{2.15}$$

Here, $r_{jk}$ is the distance between subunit $j$ and subunit $k$. For simple geometrical forms, an analytical calculation is possible. For instance, for massive spheres with radius $R$ the form factor is given by:

$$P(q)_{sphere} = \left( \frac{3 \cdot (sin(qR) - qRcos(qR))}{q^3} \right)^2 \tag{2.16}$$

This equation connects the form factor to the particle's radius in case of spheres. If the spheres' size distribution is monodisperse, the scattering vectors $q_{min1}$ and $q_{min2}$ at the equation's first two minima can give a quick estimation of the radius $R$ [12, p. 50]:

$$R \approx \frac{4.493}{q_{min1}} \qquad R \approx \frac{7.725}{q_{min2}} \tag{2.17}$$

### 2.4.4 Determination of particle size – Guinier approximation[26]

Another way to process equation 2.15 is to expand the sine function into its Taylor series:

$$\frac{sin(x)}{x} \approx \frac{x - \frac{1}{3!}x^3 + \frac{1}{5!}x^5 - \cdots}{x} = 1 - \frac{1}{3!}x^2 + \frac{1}{5!}x^4 - \cdots \tag{2.18}$$

With the first two terms of the Taylor expansion, the form factor can be approximated by:

$$P(q) \approx \frac{1}{n^2} \sum_{j=1}^{1} \sum_{k=1}^{1} (1 - \frac{1}{6}(qr_{jk})^2) \tag{2.19}$$

This can be also written as:

$$P(q) \approx \frac{1}{n^2} \sum_{j=1}^{1} \sum_{k=1}^{1} (1) + \frac{1}{6}q^2 \cdot \frac{1}{n^2} \sum_{j=1}^{1} sum_{k=1}^{1} r_{jk}^2) \tag{2.20}$$

Finally, the form factor is given by:

$$P(q) \approx 1 - \frac{1}{3}q^2 R_g^2 \tag{2.21}$$

[26] If not otherwise stated, this section follows the explanations of Øgendal [37, pp. 50-68].

Here the radius of gyration $R_g$ provides the link between the form factor and the particles spatial extension for arbitrary shaped particles, since $R_g$ is defined as the average of squared distances from its center of mass to all of its n subunits

$$R_g^2 = \frac{1}{n}\sum_{i=1}^{n} r_{i,c.m.}^2 \tag{2.22}$$

with $r_{i,c.m}$ as the distance of the i$^{\text{th}}$ subunit to the center of mass.

Again, for simple geometrical forms the radius of gyration is easily calculated and in case of massive spheres with radius r it is given by:

$$R_g = \sqrt{\frac{3}{5}}r \tag{2.23}$$

Since the approximation of the form factor in eq. 2.21 drops fast to 0 and even becomes negative, the so called Guinier approximation is used instead:

$$P(q) \approx \exp -\frac{1}{3}q^2 R_g^2 \tag{2.24}$$

The exponential function is used, because the first two terms of its Taylor series expansion[27] matches eq. 2.21. The Guinier approximation is often used to determine the particle size as mentioned above: By combining eq. 2.14 with eq. 2.24 and taking the logarithm, the scattering intensity $I_s$ in the Guinier regime can be expressed as:

$$ln(I_s(q)) = ln(I_s(0)) - \frac{1}{3}q^2 R_g^2 \tag{2.25}$$

Therefore, it is sufficient to plot $ln(I_s(q))$ against $q^2$ for size estimations. This so called Guinier plot shows a linear relationship between the two variables that can be fitted easily. The slope $a$ of this linear fit is directly proportional to the radius of gyration:

$$a = -\frac{1}{3}R_g^2 \tag{2.26}$$

In general, the Guinier approximation is only valid if $qR_g < 1$ and size determination is only possible if $q$ but also the particles are sufficiently small. Therefore, it is enough to measure the descent of the scattering intensity $I_s(q)$ to the first local minimum $q_{min1}$ in most cases. Besides, there is a practical lower limit for the particle's size: If the particles are very small, according to eq. 2.26 also the slope is small and it becomes difficult

[27] The Taylor series expansion of eq. 2.24 is $\exp -\frac{1}{3}q^2R_g^2 = 1 - \frac{1}{1!}(\frac{1}{3}q^2R_g^2) + \frac{1}{2!}(\frac{1}{3}q^2R_g^2)^2 + \frac{1}{3!}(\frac{1}{3}q^2R_g^2)^3 + \cdots$

to determine, especially as there is always background noise in scattering experiments. Literature states that this lower limit of particle size is $\lambda/20$ for isotropic scattering [37, p. 54].

# CHAPTER 3

# Material and Methods

The experimental setup is based on the HT-CPC setup used by Kupper et al. [32]: Both HT-CPC designs are described below in chapter 3.1)[28]. A static light scattering detection unit was implemented and is outlined in chapter 3.5. Furthermore, a low-temperature CNM was used for adjustment of this unit (see chapter 3.2). The aerosol source as well as the flow control is described in chapter 3.3. A comprehensive listing of used materials and devices can be found in the appendix (table A.1 to A.4). Moreover, all saturator elements that were used for the degradation test are listed in chapter 3.4.

## 3.1 High temperature condensation particle counter designs

As mentioned above two different HT-CPCs were constructed by Kupper et al. [32], one L-shaped (L-Type) and one T-shaped (T-Type) as shown in figure 3.2 and 3.3. Both consist of several milled aluminum components that can be thermo-regulated by heating cartridges. Since different temperatures for the saturator and condensor are necessary, thermal isolators[29] separate them from each other. Both devices were operated with 99 % pure[30] *n*-Eicosan $C_{20}H_{42}$ (figure 3.1) as working fluid. This non-toxic and at room temperature white crystalline solid, has a melting point of $T_{melt} = 36.7\,°C$ and a boiling point of $T_{boil} = 342.7\,°C$ [36]. Therefore, operation up to at least 300 °C should be possible.

[28] All modifications conducted as part of this thesis are stated in chapter 4.1 and 4.2.

[29] In case of the L-Type polyetheretherketone (PEEK) and in case of the T-Type Vespel SP-1 was used.

[30] Due to the production process of higher alkanes, small traces of neighboring alkanes – e.g. $C_{19}H_{40}$ – are expected.

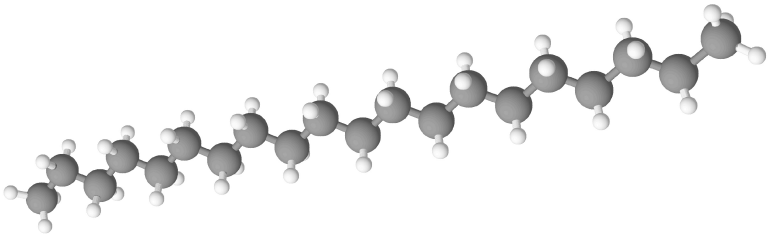

**Figure 3.1:** The structure of *n*-Eicosan $C_{20}H_{42}$ [36]. It was used as working fluid for the HT-CPCs.

### 3.1.1 L-Type HT-CPC

Since the L-Type HT-CPC is designed as a demonstrator, it is quite modular to maintain the possibility for adaption (see figure 3.2). Like all conductive cooling CPCs, its parts can be assigned to three major blocks (compare chapter 2.3):

The horizontal **saturation block** is formed by four elements:

1. The **carrier gas inlet** made out of polyetheretherketone (PEEK) to thermally isolate the gas tube from the heated saturator.
2. A **funnel** to gradually increase the gas path to meet the diameter of the wick element.
3. The **saturation chamber** that contains a removable wick element. This element supports the evaporation of the working fluid and the saturation of the carrier gas flow.
4. An **aerosol inlet** to introduce the sample gas into the carrier gas flow.

The vertical **condensor block** consists of two elements:

1. An **isolator** made out of PEEK that thermally isolates the condensor block from the hotter saturator block.
2. The **condensor** itself that cools the gas flow to initiate heterogeneous condensation.

The following three components are part of the **particle detector block** of the L-Type HT-CPC.

1. An outlet **nozzle** with a diameter of 0.5 mm to focus the sample gas flow.
2. A solid aluminum **hood** that is heated to $T_{hood} > T_{condensor}$ and covers the nozzle to prevent condensation.
3. The **static scattering setup** as described in chapter 3.5, to detect the particles.

In addition, a heated **reservoir block** containing $n$-Eicosan is connected via a valve to the saturation chamber to allow the refilling the working fluid. Since it is sufficient to heat the working fluid over its melting temperature, the reservoir is only heated to $T_{reservoir} = 50\,°\mathrm{C}$. Consequently, it is necessary to thermally isolated it from the saturator block. This is done by another PEEK element.

A LabView-based control program was implemented to handle the temperature control. The flow chart is provided in the appendix. Heating cartridges are strategically distributed to all four blocks and are monitored by class A PT100 that are mounted on the side of the aluminum parts. Additionally, glass wool is used as insulation. This setup allows to set the temperature as stable as $\pm 0.1\,\mathrm{K}$. For light scattering measurements the temperatures are set to:

$$\begin{aligned} T_{hood} &= 230\,°\mathrm{C} \\ T_{condensor} &= 170\,°\mathrm{C} \\ T_{reservoir} &= 50\,°\mathrm{C} \\ T_{saturator} &= 210\,°\mathrm{C} \end{aligned}$$

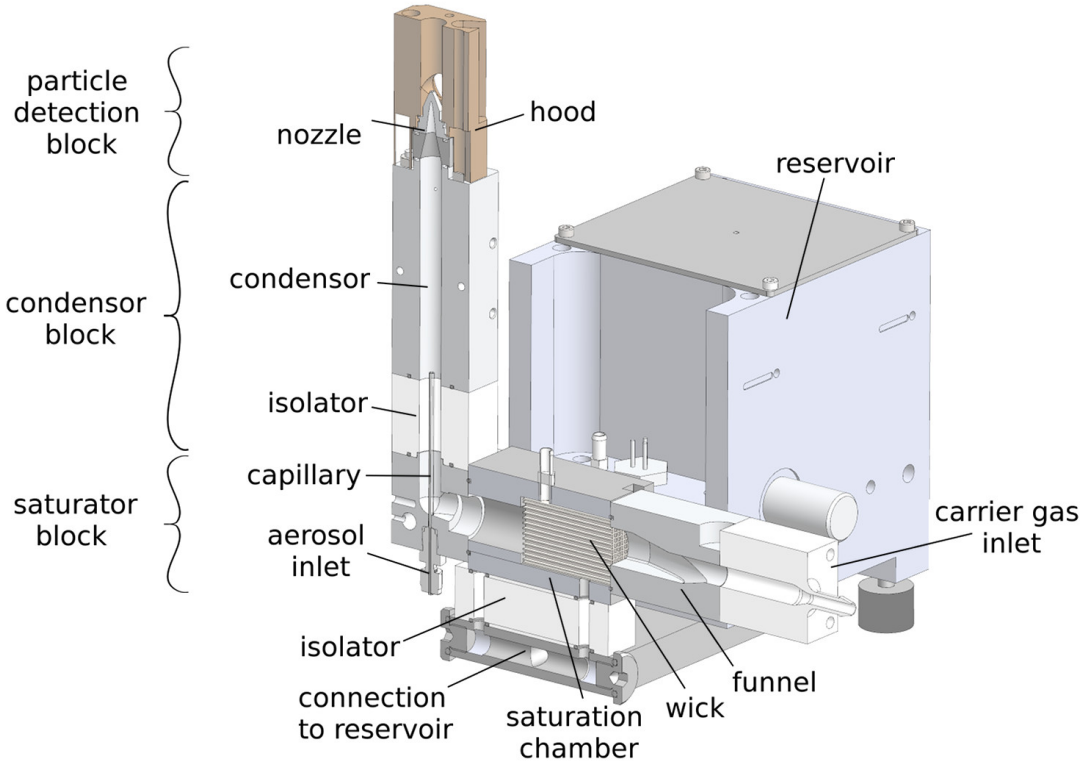


**Figure 3.2:** Schematics of the L-type HT-CPC.

### 3.1.2 T-Type HT-CPC

In contrast to the L-shaped HT-CPC, the T-Type has a mirrored saturation block that allows to introduce the aerosol from both sides simultaneously. It has two saturation chambers, each with a permanently mounted porous aluminum wick and an open connection to the working fluid reservoir. Hence, the reservoir and the saturation chambers are communicating vessels with the same working fluid level. The level is monitored by a sensor in the reservoir and refills are done manually. Since the connections between the reservoir and the saturators are made of Vespel-SP1, the two blocks are thermally separated. Vespel-SP1 parts also thermally separate the vertical condensor from the saturator on the one side and from the outlet nozzle on the other side. The saturator and condensor block are thermo-regulated by heating cartridges, while in case of the reservoir heating mats are used. The outlet nozzle, however, is not heated. All temperatures are

monitored with PT100 temperature sensors and temperature controller keep the parts at:

$$T_{condensor} = 190\,^{\circ}\mathrm{C}$$
$$T_{reservoir} = 60\,^{\circ}\mathrm{C}$$
$$T_{saturator} = 220\,^{\circ}\mathrm{C}$$

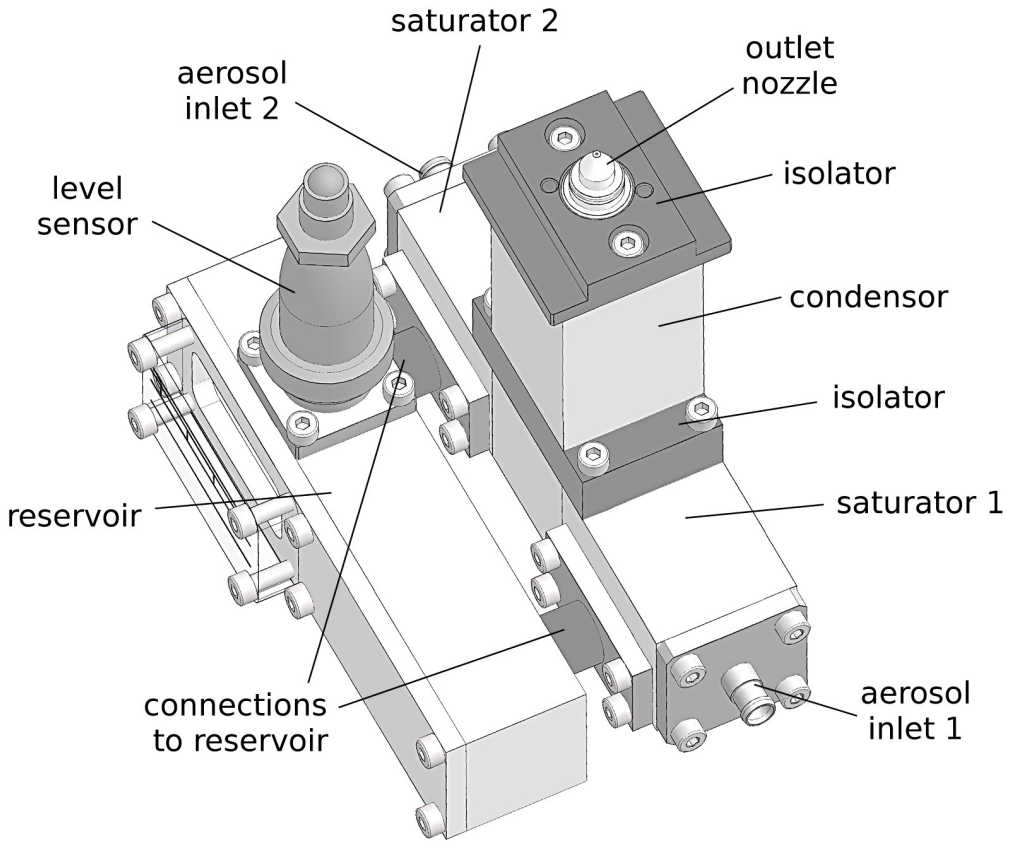


**Figure 3.3:** Schematics of the T-type HT-CPC.

## 3.2 Condensation nucleus magnifier design

To establish and align the static light scattering measurement setup, the CNM device from Cresnoverh [12] as shown in figure 3.4 is used. In principle, a CNM is a conductive cooling CPC without the particle detection unit: It grows particles to a certain size based on the temperature difference $\Delta T$[31] between saturator and condensor. Both temperature circuits consist of one PT100 temperature sensor and two Peltier elements, which heat in case of the saturator or cool in case of the condensor their aluminum components.

[31] $\Delta T = T_{saturator} - T_{condensor}$.

To ensure a steady $\Delta T$ the temperature control was adapted: Two PID[32] temperature controllers switch the Peltier elements of the CNM via solid state relays. Thus, the temperatures fluctuations are less than $\pm 0.1\,\mathrm{K}$. In general, the temperatures are set to:

$$T_{saturator} = 34\,^{\circ}\mathrm{C}$$
$$T_{condensor} = 26\,^{\circ}\mathrm{C}$$

As working fluid *n*-Decan ($C_{10}H_{22}$) is used. This working fluid has several advantages over *n*-Butanol, especially in case of exhaust measurements with a CPC [29] On the one hand, it hardly reacts chemically with exhaust components and does not mix with water. On the other hand, the flash point of *n*-Decan is higher than the one of butanol and due to the fact that it is less toxic it is easier to handle[33]. Moreover, as *n*-Eicosan – the working fluid used in case of the HT-CPC – also *n*-Decan is an alkane.

The working fluid level in the reservoir is kept constant by a capacitive sensor that controls a valve to a tank.

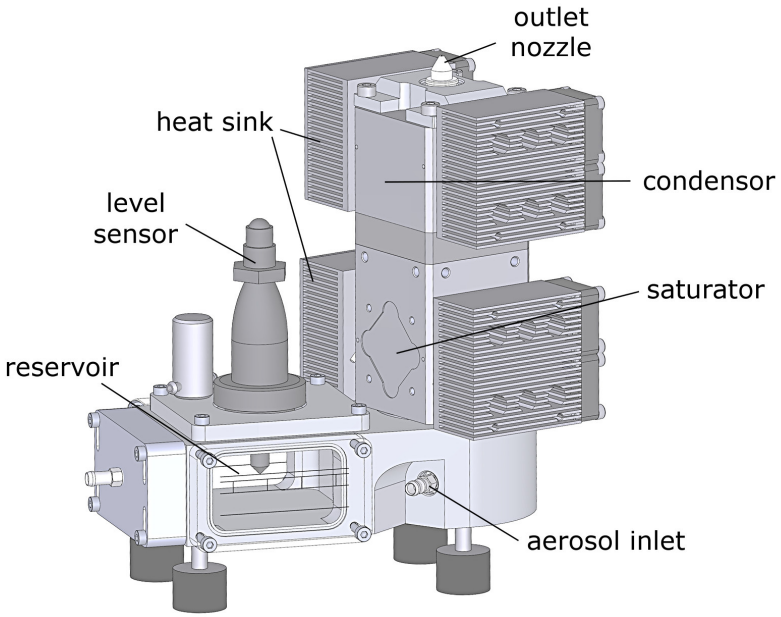


**Figure 3.4:** Schematics of the used CNM.

[32] PID stands for *proportional-integral-derivative* and refers to the feedback mechanism that is used to control the temperature.

[33] While the flash point of *n*-Decan is 46 °C (closed cup), the flash point of *n*-Butanol around 29 °C to 37 °C (closed cup) is very close to the typical operating temperatures of CPCs [35, 34].

## 3.3 Aerosol source and flow control

To test the HT-CPCs and the CNM an aerosol source is necessary. Since the aim of the experiments were to establish proof of concept a defined particle number or particle size was not required. Hence, ambient air as particle source was sufficient. According to measurements with a TSI 3938 SMPS system, ambient air in the laboratory contains 8000 particles/cm$^3$ to 10 000 particles/cm$^3$. As figure 3.5 shows, their size is ranging between 20 nm to 110 nm with an average size of approximately 65 nm.

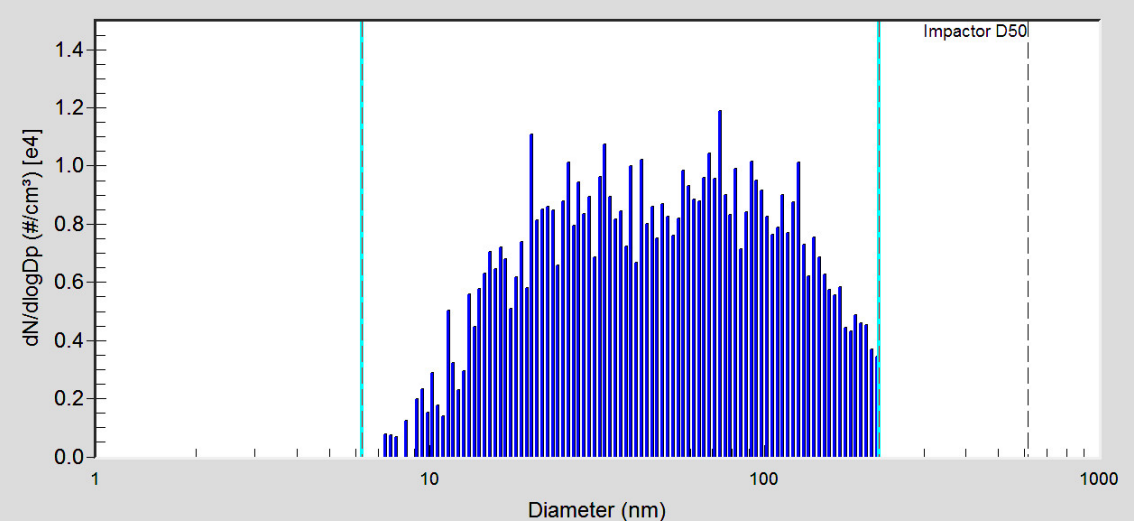


**Figure 3.5:** Particle number and size distribution of ambient air in the laboratory measured with a SMPS system.

A Venturi pump driven by compressed air with a pressure of 2 bar to 3 bar is utilized to sample ambient air. A needle valve and a bypass regulates the sample flow towards the CNM/HT-CPC. In addition, a thermal mass flow controller (MFC) allows the fine adjustment of the gas flow to the device as shown in figure 3.6. In general it was set to 0.6 l min$^{-1}$.

Due to the operating principle of a Venturi pump a dilution of the aerosol is inevitable. Together with the particle loss due to the tubing, the particle concentration drops before it enters the devices normally to less than 2000 particles/cm$^3$.

To strip almost all particles from the aerosol a high efficiency particulate air (HEPA) filter with a efficiency of 99.99 % [20] is attached to the aerosol inlet of the Venturi pump. In this way, carrier gas without any particles is obtained.

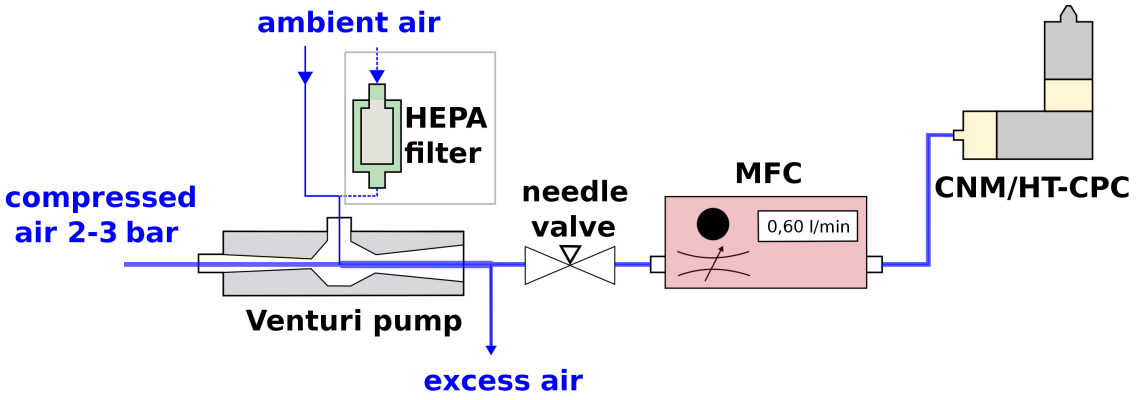


**Figure 3.6:** Flow control schematics: A Venturi pump samples aerosol from ambient air. A needle valve and a MFC controls the gas flow towards the CNM/HT-CPC. To strip the ambient air from all particles a HEPA filter is used at the aerosol inlet of the Venturi pump.

## 3.4 Degradation experiments with different wick elements

First tests with the HT-CPC using a NGK cordierite wick by Kupper et al. [31] showed that the working fluid degrades over time with unknown influence on the device's performance. Therefore, wick materials that minimize degradation are preferable. In general, as stated in chapter 2.3, a wick element is porous to enhance its wettability, has a large surface area and thus ensure a quick saturation of the carrier gas in the saturation chamber. In addition, in case of a HT-CPC it has to withstand temperatures up to 300 °C without decomposition. The following wick materials meet these requirements:

- IBIDEN FRAUENTHAL HT ceramic
- IBIDEN FRAUENTHAL MK20 cordierite ceramic
- NGK cordierite ceramic
- SiC diesel particle filter
- IBIDEN FRAUENTHAL NT ceramic
- Porous aluminum wick

As shown in figure 3.7, all materials have a honeycomb-like structure that acts as flow conditioner and were cut to fit the saturator chamber of the L-Type HT-CPC[34]. The typical chemical composition of the IBIDEN FRAUENTHAL ceramics is provided in the appendix in table A.5.

[34] The degradation tests are done with the L-Type HT-CPC only, since the T-Type has issues with leakage.

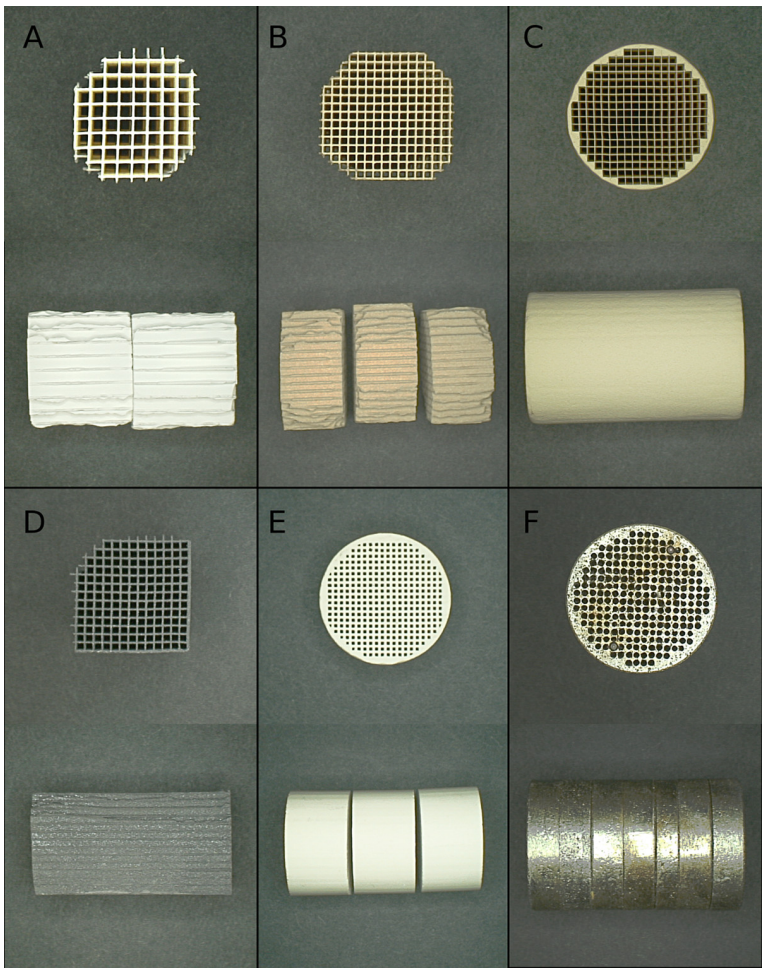


**Figure 3.7:** Different potential wick materials for a HT-CPC: A) IBIDEN FRAUENTHAL HT ceramic, B) IBIDEN FRAUENTHAL cordierite ceramic, C) NGK cordierite ceramic, D) SiC diesel particle filter, E) IBIDEN FRAUENTHAL NT ceramic and F) porous aluminum wick.

The first four of the listed wick materials were tested qualitatively[35] with the L-Type HT-CPC for their long-term performance over 18.25 h. The following two settings were realized for all wick materials:

**Setting 1:** Ambient air containing all particle is introduced at the carrier gas inlet.

**Setting 2:** $N_2$ stripped off all particles is introduced at the carrier gas inlet.

In addition, a third setup was used to evaluate the performance of the FRAUENTHAL HT ceramic, while using the aerosol gas inlet of the HT-CPC as intended by its design:

**Setting 3:** $N_2$ stripped of all particles is introduced at the carrier gas inlet. In addition

[35] Quantitative measurements utilizing the static light scattering setup used by Kupper et al. [32] were not feasible, since the results of similar measurements were not comparable. Since only one porous aluminum wick is available and the FRAUENTHAL NT ceramic is not porous, both materials were excluded from testing.

ambient air containing particles is introduced at the sample gas inlet through a capillary.

In all cases the input gas flow at the carrier gas inlet is kept at $0.4(1)\,\mathrm{l\,min^{-1}}$ with a MFC[36]. In case of setting 3, the flow at the sample gas inlet is set to $0.3\,\mathrm{l\,min^{-1}}$ with a second MFC[37]. For all wick material tests the temperatures of L-Type HT-CPC are set to:

$$T_{hood} = 230\,^{\circ}\mathrm{C}$$
$$T_{condensor} = 180\,^{\circ}\mathrm{C}$$
$$T_{reservoir} = 50\,^{\circ}\mathrm{C}$$
$$T_{saturator} = 205\,^{\circ}\mathrm{C}$$

## 3.5 Static light scattering setup

To determine the particle size at the aerosol outlet of the CNM and in further consequence of the HT-CPC a static light scattering detector setup was realized.

As depicted in figure 3.8 the optics are mounted on a motor driven rotary table that is installed on an aluminum rack. The used stepper motor allows changes of the detector position and hence the scattering angle $\theta$ in steps of 0.02°. In addition, three linear translation stages allow the fine adjustment of the detector position in XY- and the laser position in XYZ-direction.

Since the Z-position of the laser is adjustable, it is possible to align its optical axis with the one of the detector's optical system as depicted in figure 3.9.

The 532 nm laser is focused 2 mm above the outlet nozzle of the CNM/HT-CPC on the scattering volume with a plano-convex lens that has a focal length of $f = 200\,\mathrm{mm}$. Thereby, the outlet nozzle of the CNM/HT-CPC has to be in the center of rotation[38]. Furthermore, apertures constrain the laser beam and the laser's intensity is reduced by an absorptive neutral density filter with an optical density of 0.3.

[36] Since the liquid level in the saturation chamber of the L-Type varies over time, also the gas flow shows variations of $\pm 0.1\,\mathrm{l\,min^{-1}}$.

[37] During operation the flow was not stable, but dropped to almost zero repeatedly.

[38] If the outlet nozzle is not in the center of rotation, the detector's area of vision is continuously moved out of the scattering volume while rotating. Hence, the signal is decreasing.

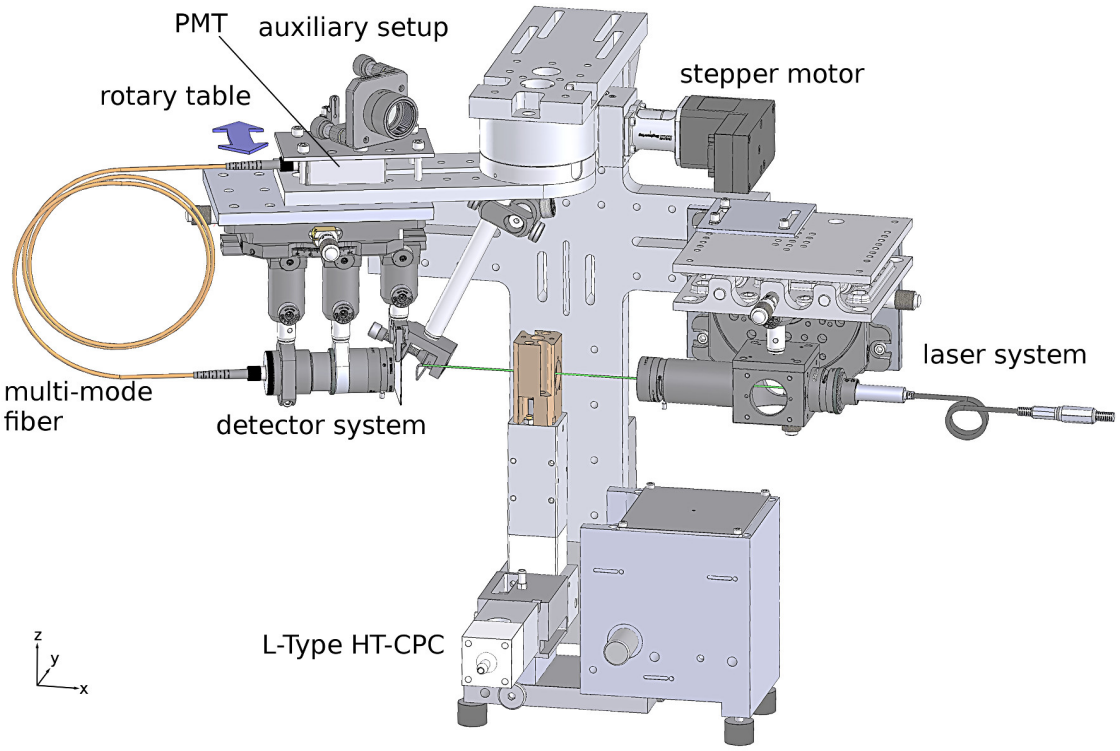


**Figure 3.8:** Schematics of the static light scattering setup: A motor driven rotary table allows the detection of scattered light at different angles. The position of the optical systems can be fine adjusted by linear translation stages.

The primary laser beam is caught by a beam dump right in front of the polarizing filter. Since the beam dump intersects the detector's line of sight, measurements below $\theta < 3°$ are not feasible.

As detector a fiber coupled photomultiplier tube (PMT) is used. The scattering volume is mapped onto a multi-mode fiber by a biconvex lens with a focal length of $f = 35\,\mathrm{mm}$ that is arranged in a $2f$-setup. Thereby, the diameter of the fiber core restricts the detector's area of vision and an iris aperture restricts the opening angle.

To adjust the $2f$-setup, the optical setup is used the other way around: Instead of the PMT, the laser is coupled to the optical fiber. In this way, the end of the fiber is mapped onto the scattering volume. By adjusting the focal point – by moving the XY-stage – the $2f$-setup can be adjusted easily.

To achieve a sufficient coupling, an auxiliary setup was implemented: A plano-convex lens with a focal length of $f = 50\,\mathrm{mm}$ focuses the laser beam onto the fiber's end. A kinematic mount provides the possibility to fine adjust the laser focus, thus optimizing the coupling

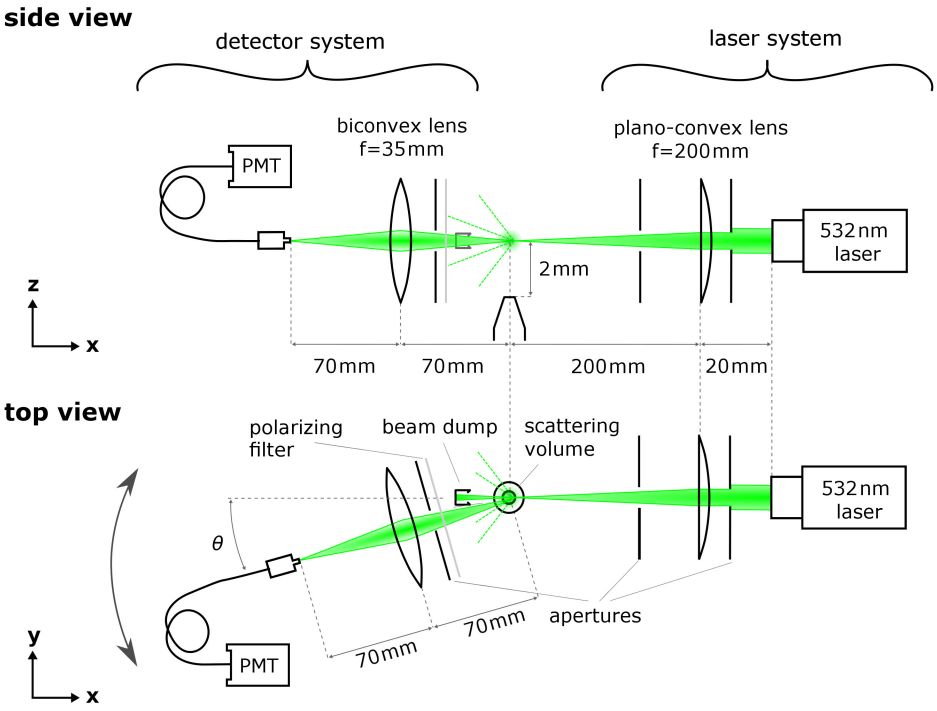


**Figure 3.9:** Optical system of the static light scattering setup.

efficiency.

Since the PMT has a current output, the voltage drop to ground across a resistor of resistance $R = 200\,\mathrm{k\Omega}$ is tapped with an oscilloscope. The measured voltage is proportional to the output current and hence to the scattered intensity. To ensure that the PMT's output is in its linear range, the control voltage of the PMT has to be adjusted. Depending on the oscilloscope reading during the alignment procedure, 0.6 V to 0.7 V were applied. To sample the signal over time and at different scattering angles, a LabView program is used. It controls the stepper motor and collects data from the oscilloscope. Thus, the signal can be measured at different detector positions for a given amount of sampling steps. At each sampling step the oscilloscope collects $5 \times 10^6$ data points[39] over 4 s. At each detector position the mean as well as the cumulative sum of the detected signal is calculated automatically.

Light scattering measurements were done with the CNM as well as with the L-Type HT-CPC. Table 3.1 provides an overview of the used configurations.

[39] The oscilloscope is set to 1.0 V/division and 400 ms/division and the high resolution sampling mode is enabled.

**Table 3.1:** Configuration for light scattering measurements with the CNM and the L-Type HT-CPC

| **setting** | **CNM** | **L-Type** |
|---|---|---|
| detection range | $\theta = 2°$ to $20°$ | |
| flow rate | $0.6\,\mathrm{l\,min^{-1}}$ | |
| step size | $\Delta\theta = 0.5°$ | |
| sampling steps | 5 | |
| sample gas config. 1 | ambient lab air | |
| sample gas config. 2 | HEPA filtered air | |
| | | |
| $T_{Condensor}$ | 34 °C | 170 °C |
| $T_{Saturator}$ | 26 °C | 210 °C |
| $T_{Hood}$ | – | 230 °C |
| $T_{Reservoir}$ | – | 50 °C |
| $V_{PMT\ control}$ | 0.65 V | 0.6 V |

# CHAPTER 4

# Results and Discussion

## 4.1 Modification of the L-Type HT-CPC

Due to its modular design, the L-Type HT-CPC is prone to leakage. The working fluid diffuses through gaps that open up due to uneven tightening of bolts or due to insufficient clamping pressure as shown in figure 4.1. Consequently, the working fluid evaporates on the outer hot surfaces and uncontrollable condensation on surrounding particles occurs. This leakage influences all measurements conducted with the HT-CPCs and leads to unreliable working conditions. Therefore, it has to be reduced to a minimum, before any measurements can take place.

The following weak spots were identified and the device was modified to improve the performance:

1. The M4 steel studdings that should hold the saturator block together, showed no grip in the screw holes of the aluminum saturation chamber in heated conditions: The internal threads were torn off by the harder steel studding due to extensive tightening torque and different thermal expansion coefficients. Therefore, the screw holes were enlarged and M6 tapped to ensure a better hold due to larger thread depth. A threaded insert was made out of brass[40] to allow the use of a M4 brass stubbing to hold the saturation block together as shown in figure 4.2A.

2. A very similar issue occurred in case of the condensor block: The M4 steel studding

[40] Brass was used to better match the thermal expansion coefficient of aluminum.

was supposed to hold in screw holes in the PEEK isolation element. Since the PEEK could not withstand the tightening torque in heated conditions, an adaption was necessary: As shown in figure 4.2B holes were drilled to insert additional bolt nuts to secure a sufficient clamping pressure.

3. Furthermore, the PEEK isolation showed also deficiencies between the saturation chamber and the connection to the reservoir: Due to numerous heating and cooling cycles the PEEK block slightly deformed. As shown in figure 4.1C, the surfaces were no longer plane parallel and a tight connection was not longer possible resulting in leakage in case of refilling. Therefore, it was sanded and polished to regain its original shape.

4. Although all components are screwed together using sealing rings, it appeared to be necessary to use additional polytetrafluoroethylene (PTFE) sealing tape between all components to improve the leakproofness. An attempt to seal the L-Type with LOCTITE SI 5920 – a gasketing paste for high temperature applications – was not practicable, since the cleaning effort in case of dismantling was too laborious as shown in figure 4.2D.

Furthermore, due to temperature changes of ≈180 K during a typical heating cycle, the aluminum parts expand and contract accordingly. As consequence, bolts are prone to come loose. Therefore, it is necessary to tighten all screws before every test run of the L-Type HT-CPC. With all these measures it was possible to reduce the leakage to an amount that should not influence light scattering measurements by any means.

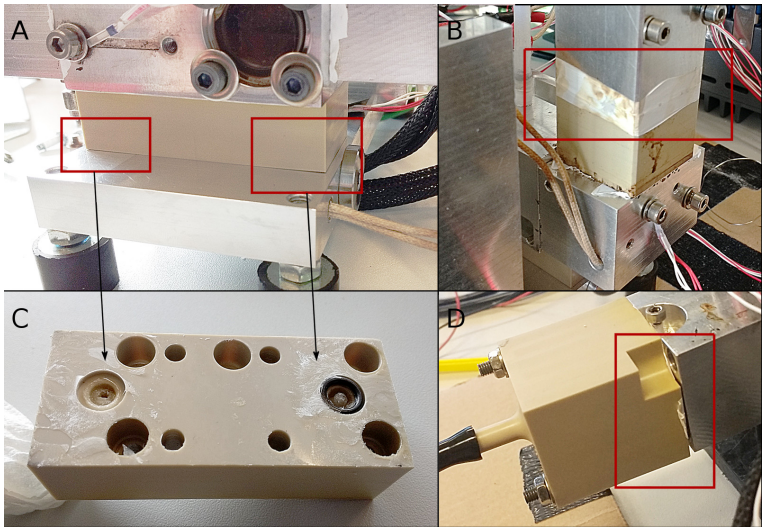


**Figure 4.1:** Gaps between the individual components of the L-Type HT-CPC lead to leakage: They open up due to deformation (A, C) or due to uneven tightening of bolts and insufficient clamping pressure (B, D).

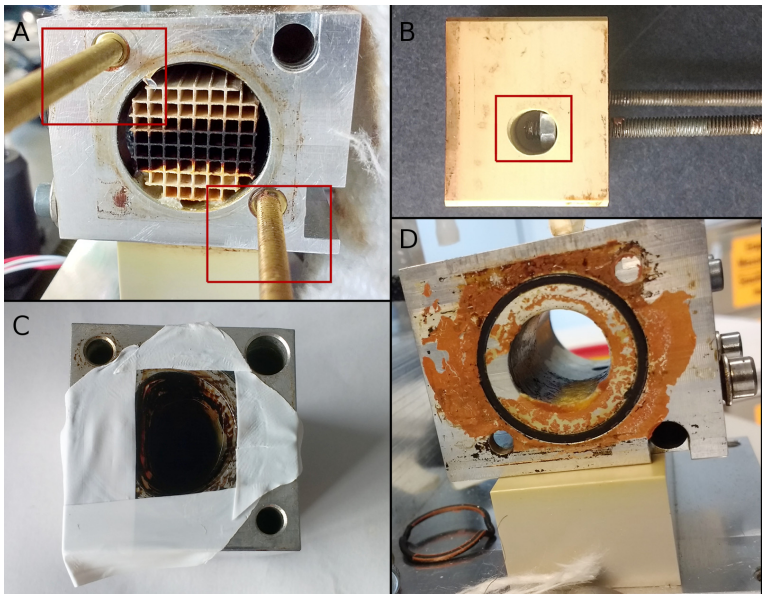


**Figure 4.2:** Modification of the L-Type HT-CPC to improve its leakproofness: A) To prevent the gap in the saturator block, the M4 screw holes were enlarged and M6 tapped to ensure a better hold of the brass studdings due to the larger thread depth. B) In case of the condensor block, additional bolt nuts were used to secure a sufficient clamping pressure. C) PTFE sealing tape was used between all components. D) An attempt to seal the L-Type with a gasketing paste was not practicable.

## 4.2 Modification of the T-Type HT-CPC

The T-Type HT-CPC shows similar issues as the L-Type. Again, working fluid diffuses through gaps that open due to insufficient sealing. In case of the T-Type two issues were identified:

1. The main weak spot of the T-Type is the connection between saturator and reservoir as show in figure 4.3A-C: The Vespel-SP1 connection parts are screwed into the reservoir on the one side and into adapter plates on the other side. Both sides are prone to leakage, therefore it was necessary to apply additional sealing tape. As a consequence, the spacing of the two connections became uneven, because the two Vespel parts were screwed unequally far into the reservoir or the adapter plate. Due to the different distances, a certain strain on the connectors was inevitable. In addition, the internal threads of the M4 screw holes were again torn off due to extensive tightening torque in some cases. In summary, it was not possible to evenly tighten these bolts to reduce the leakage between the saturator and reservoir.

2. Besides, due to the fact that the outlet nozzle is not heated, heavy condensation occurs. The liquid working fluid clogs the nozzle sporadically and interrupts the laminar flow. To prevent condensation, a heated hood as used for the L-Type would have been necessary.

Since the heavy leakage in the connection region is not manageable without an extensive adaption of the construction, the T-Type HT-CPC was not investigated any further.

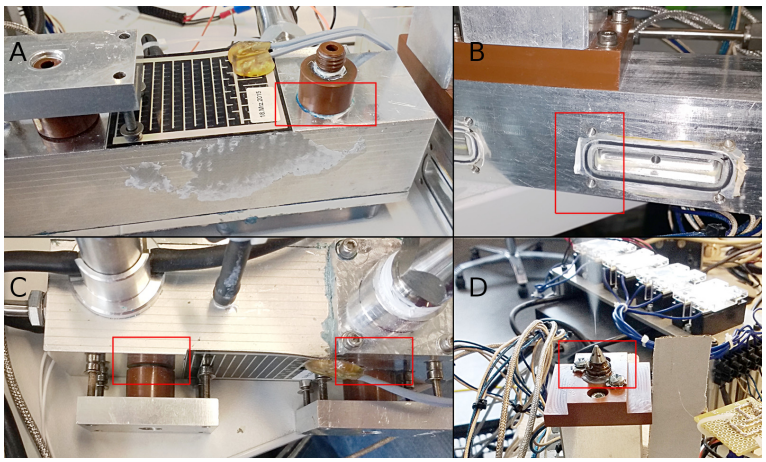


**Figure 4.3:** Issues with leakage in case of the T-Type HT-CPC: A) The Vespel-SP1 connection part between reservoir and saturator of the T-Type HT-CPC is the main weak spot. B) In some cases the internal threads of the M4 screw holes are torn off due to extensive tightening torque. C) The spacing of the two connections is different, due to different screw-in depths of the Vespel-SP1 components. D) Working fluid condensates on the unheated outlet nozzle.

## 4.3 Degradation experiments with different wick elements

To clarify the suitability of different wick materials for a HT-CPC and their impact on the degradation of the working fluid (shown in figure 4.4), the following four wick materials were investigated:

- IBIDEN FRAUENTHAL MK20 cordierite ceramic
- IBIDEN FRAUENTHAL HT ceramic
- NGK cordierite ceramic
- SiC diesel particle filter

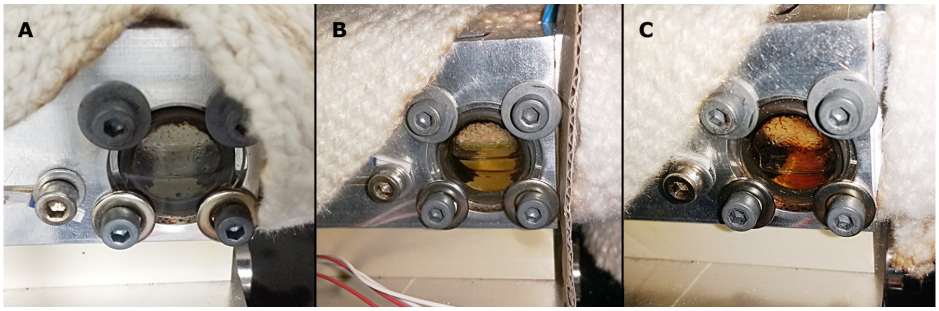


**Figure 4.4:** Degradation of the working fluid: As clearly visible, it turns yellowish due to chemical decomposition over time.

### 4.3.1 X-ray fluorescence analysis

Since the chemical composition of the wick materials was partly unknown, it was determined using X-ray fluorescence (XRF) spectroscopy. The results are listed in table 4.1. The XRF analysis of the SiC diesel particle filter shows mostly Si and small amounts of Sr and Al, because carbon is not detectable with the used equipment. The analysis of the IBIDEN FRAUENTHAL ceramics indicate a slightly higher proportion of Si as reported by the manufacturer[41] (compare table A.5). In addition, it was revealed that the analyzed MK20 ceramics does not contain Mg in the expected amount of about 9 %. Instead it contains about twice as much K, Ti and Fe as the HT ceramic samples. In even higher amounts the latter two elements are also present in the cordierite ceramic of NGK. Fe is a catalytically active element and Ti a known carrier element that supports the catalytic component by increasing the surface area [14]. Thus, they might accelerate the degradation process in case of the cordierite ceramics.

**Table 4.1:** XRF analysis of available wick materials: Material composition of IBIDEN FRAUENTHAL HT ceramic (HT1, HT2), of IBIDEN FRAUENTHAL MK20 cordierite ceramic, of NGK cordierite ceramic and of a SiC diesel particle filter.

| Element | HT1 | HT2 | MK20 | ngk cordierite | Particle Filter |
|---|---|---|---|---|---|
| **Al** | 62.1 % | 62.8 % | 35.5 % | 36.1 % | 1.4 % |
| **Si** | 34.2 % | 32.9 % | 57.2 % | 54.6 % | 94.4 % |
| **K** | 1.4 % | 1.6 % | 2.8 % | 0.4 % | 0.1 % |
| **Fe** | 1.1 % | 1.3 % | 2.6 % | 5.4 % | 0.4 % |
| **Cl** | 0.4 % | 0.5 % | 0.4 % | 0.4 % | 0.2 % |
| **Ca** | 0.4 % | 0.4 % | 0.5 % | 0.3 % | 0.2 % |
| **Ti** | 0.3 % | 0.3 % | 0.6 % | 2 % | 0.0 % |
| **Sr** | 0.0 % | 0.0 % | 0.0 % | 0.0 % | 3.2 % |
| **Ga** | 0.0 % | 0.0 % | 0.2 % | 0.0 % | n.d. |
| **Ni** | n.d. | n.d. | 0.0 % | 0.3 % | 0.0 % |
| **Cr** | 0.0 % | n.d. | 0.0 % | 0.1 % | 0.0 % |

n.d. = not detected

### 4.3.2 Long term tests

To evaluate the performance of the four wick materials, long-term tests with the L-Type have been conducted as described in chapter 3.4. Since light scattering measurements with the L-Type were not reliable over a long time period, no quantitative evaluation was

[41] The analysis of two HT ceramic samples of different patches indicates that the composition of the ceramics varies slightly. Hence, the here presented values should be taken as approximate reference only.

possible. Instead, the impact of a test run on a wick was documented qualitatively.

**Frauenthal HT ceramics**

As shown in figure 4.5 the FRAUENTHAL HT ceramic is a white ceramic with a thin-wall honeycomb structure that has a grid size of 2.05(5) mm and a wall thickness of 0.37(1) mm. For all test runs two elements with a height of 19.38(6) mm each were used.

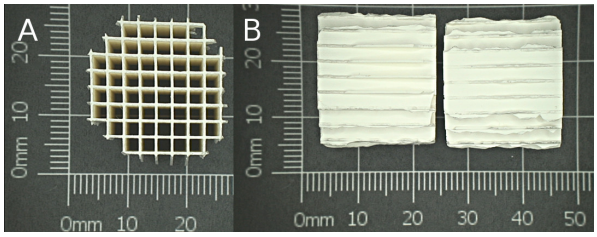


**Figure 4.5:** New FRAUENTHAL HT ceramic saturator element. A) Front and B) side view.

In test setting 1 ambient lab air was used as carrier/sample gas. As expected, the constant introduction of oxygen during the 18.25 h of operation leads to advanced degradation of the working fluid. As shown in figure 4.6, it appears yellowish due to decomposition products. In addition, these products are deposited onto the wick element as the dark decolorations. As shown in the picture, only the top half of the wick element is affected, since the L-Type's construction channels the gas flow to the upper part of the wick.

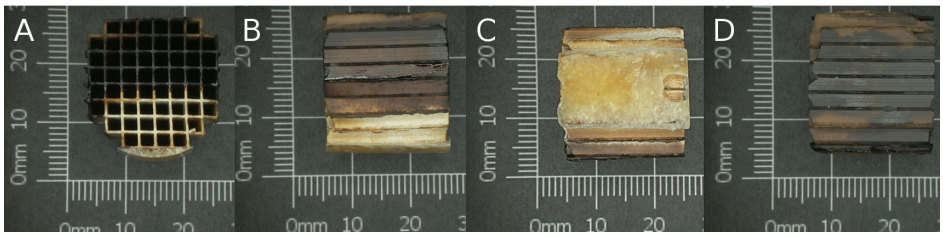


**Figure 4.6:** FRAUENTHAL HT ceramic after 18.25 h of use in setting 1: Unfiltered ambient lab air introduced at the carrier gas inlet. A) Front, B) side, C) bottom and D) top view.

The depositions have an clear impact on the the wick's appearance as shown in figure 4.9: After the test run in setting 1, the once slightly structured surface of the wick is covered with a brown to black layer of degradation products that appears like an enamel. Whether this layer seals the surface, reduces the wick's porosity or effects the saturation is unclear and should be subject to further analysis. On top a transparent layer of *n*-Eicosan is solidified, as clearly visible at the edge in figure 4.9E.

After 18.25 h of operation in test setting 2 with $N_2$ as carrier/sample gas, only minor

depositions of degradation products at the top of the wick element become visible as seen in figure 4.7. It is very likely that they are a result of the degradation due to residual oxygen in the saturation chamber at the start of the test run, since the chamber was not purged with $N_2$ beforehand. At a certain point this oxygen is depleted and is not available for chemical reactions any longer. Hence, at the end of the test run, the working fluid shows no sign of degradation at all.

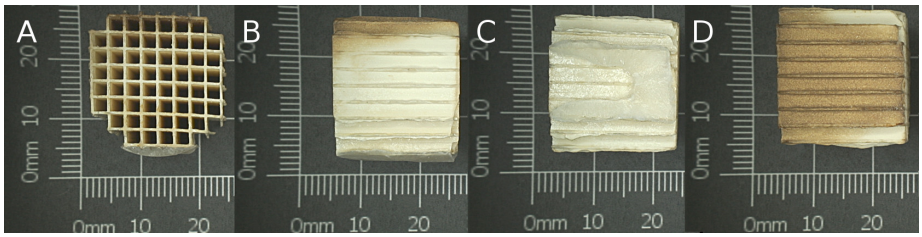


**Figure 4.7:** FRAUENTHAL HT ceramic after 18.25 h of use in setting 2: $N_2$ introduced at the carrier gas inlet. A) Front, B) side, C) bottom and D) top view.

Furthermore, also the impact of the degradation on the wick is minimal. As shown in figure 4.9G, only minor depositions are visible after the test run. In contrast to the findings with ambient air, only a clear layer of *n*-Eicosan covers the surface quite uniformly as shown in figure 4.9H. A very similar result is obtained in test setting 3 as shown in figure 4.8. Here as well, $N_2$ is used as carrier gas, but the sample gas is directly injected into the condensor through a capillary as intended by the design of the L-Type. Hence, no additional oxygen was introduced into the saturation chamber and the degradation remains negligible. However, this operation mode was not stable with the in chapter 3.3 described flow control setup. The flow rate through the capillary repeatedly drops from 0.3 L min$^{-1}$ to almost zero for a short time. Probably the capillary becomes partly clogged by condensed working fluid over time. Due to this circumstance and due to the fact that the visible degradation in setting 2 and setting 3 is comparable low, further wick tests in setting 3 were omitted.

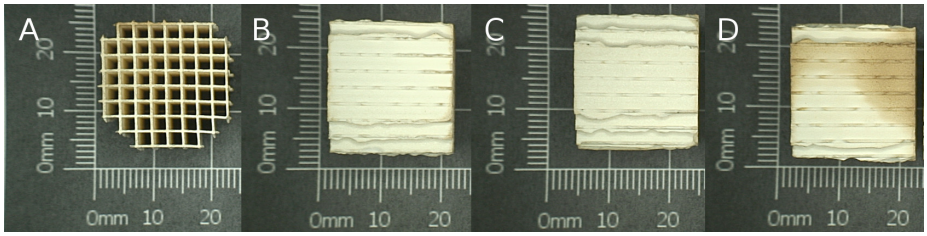


**Figure 4.8:** FRAUENTHAL HT ceramic after 18.25 h of use in setting 3: $N_2$ introduced at the carrier gas inlet and unfiltered ambient lab air at the sampling gas inlet. A) Front, B) side, C) bottom and D) top view.

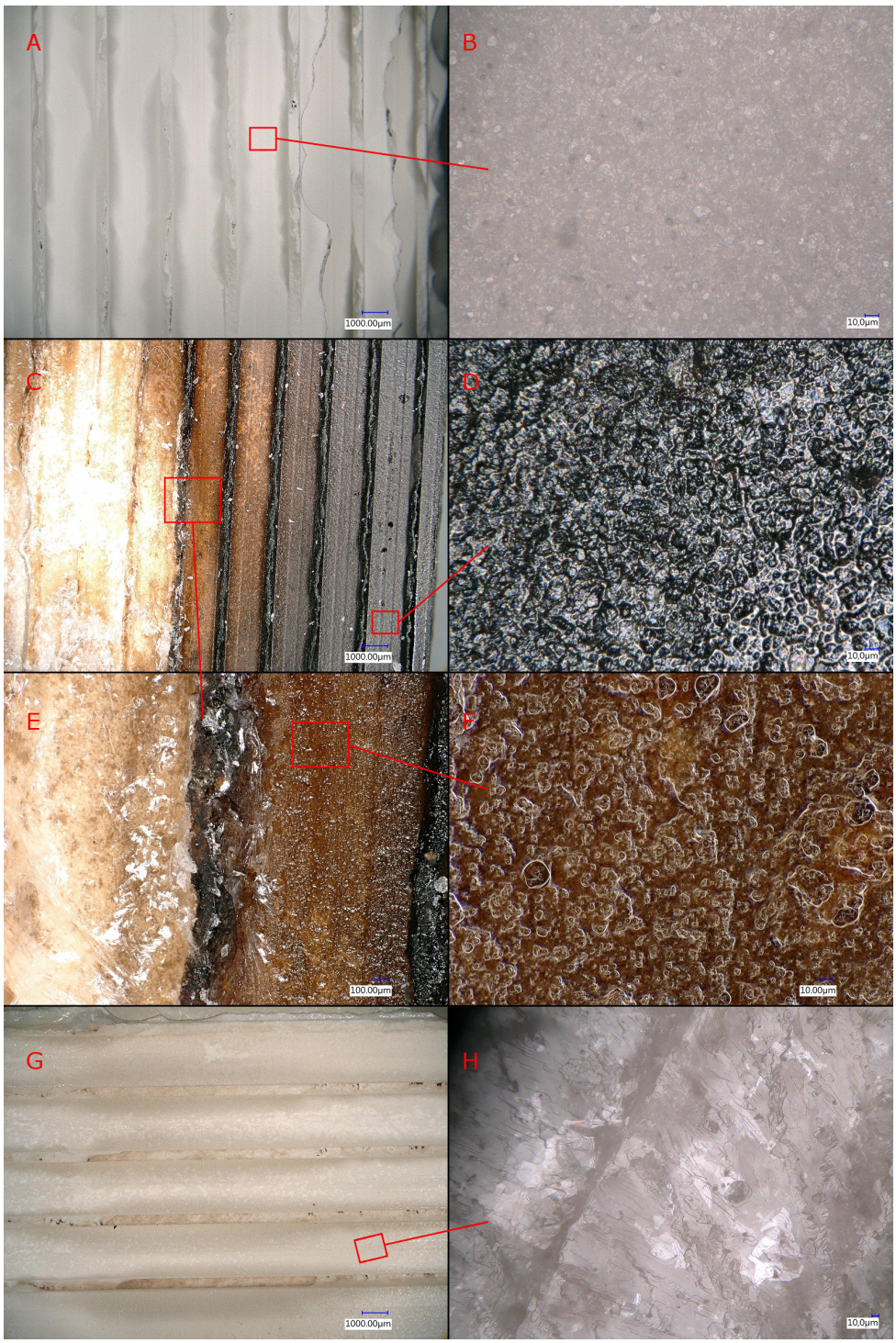


**Figure 4.9:** Change of a FRAUENTHAL HT ceramic wick due to deposition of degradation products on the surface: A) Microscope pictures of a surface of an unused wick. The dark spots on the edges are due to the cutting. B) The surface appears slightly structured. C) Side few of a wick after the test run in setting 1. D) Black depositions cover the surface of the wick completely. E) Solidified *n*-Eicosan still appears transparent and covers an edge – that shows signs of depositions – in a flaky manner. F) Less exposed areas are covered with brownish degradation products. G) Side view of a wick after the test run in setting 2: Only minor degradation signs on the edges are visible. H) The surface is covered with a transparent layer of *n*-Eicosan.

**Frauenthal MK20 ceramics**

The FRAUENTHAL MK20 ceramic is a cream-colored cordierite ceramic with a thin-wall honeycomb structure that has a grid size of 1.00(5) mm and a wall thickness of 0.27(1) mm as shown in figure 4.10. For all tests three elements with a height of 11.41(3) mm were used.

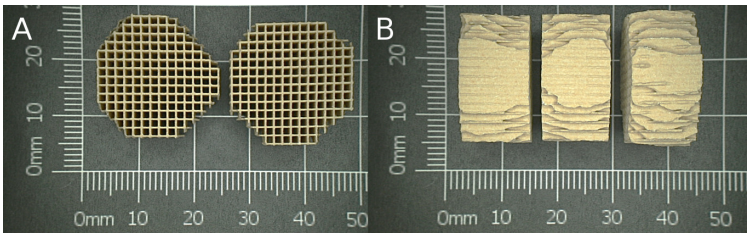


**Figure 4.10:** New FRAUENTHAL MK20 cordierite ceramic saturator element. A) Front and B) side view.

After 18.25 h of operation in test setting 1 the working fluid appears dark yellow with brown inclusions indicating heavy decomposition in figure 4.6. Again, the surface is stained black and in comparison to FRAUENTHAL HT ceramics, the surface appears to be more evenly covered. Furthermore, the grid seems partly clogged and it is not clear, whether this clogging is permanent or if it has an impact on the flow inside the chamber.

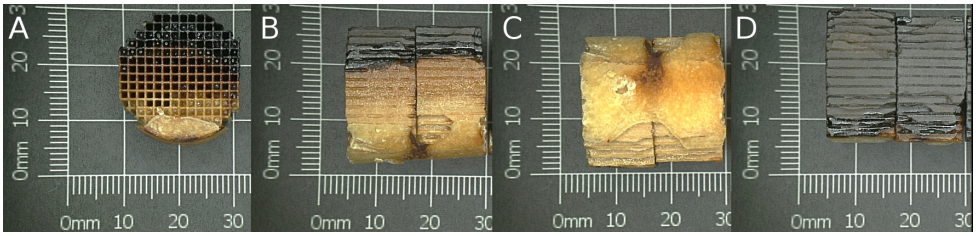


**Figure 4.11:** FRAUENTHAL MK20 cordierite ceramic after 18.25 h of use in setting 1: Unfiltered ambient lab air introduced at the carrier gas inlet. A) Front, B) side, C) bottom and D) top view.

The opposite is true, after the test run in test setting 2, since there are almost no visible depositions. Only minimal discoloration at the top of the wick – as shown in figure 4.7 – indicates degradation at the beginning of the test run due to residual oxygen. After 18.25 h the working fluid appears white with no signs of decomposition at all.

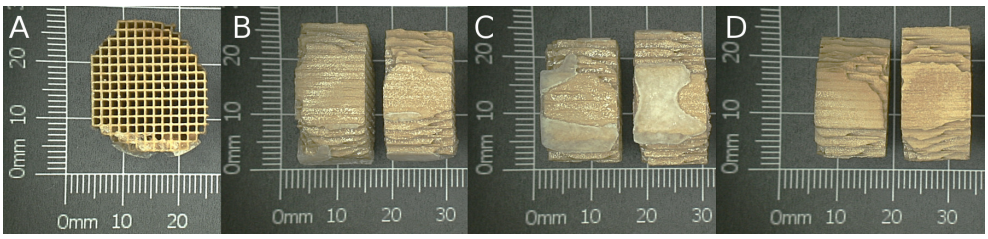


**Figure 4.12:** FRAUENTHAL MK20 cordierite ceramic after 18.25 h of use in setting 2: $N_2$ introduced at the carrier gas inlet. A) Front, B) side, C) bottom and D) top view.

### NGK cordierite ceramics

As shown in figure 4.13 the NGK ceramic is a cream-colored cordierite ceramic with a thin-wall honeycomb structure that has a grid size of 1.00(5) mm and a wall thickness of 0.11(1) mm. In this case, only one element with a height of 40.1(1) mm and a smooth outer cladding was used.

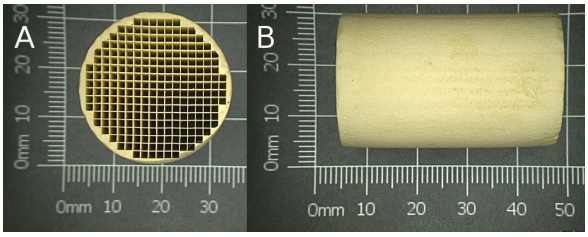


**Figure 4.13:** New NGK cordierite ceramic saturator element. A) Front and B) side view).

After the test run in setting 1, the increased decomposition is again obvious: As shown in the side and bottom view of the NGK wick in figure 4.14, the cladding is more uniformly stained than the FRAUENTHAL wicks before: In comparison, the bottom half of both FRAUENTHAL ceramics in figure 4.6 and figure 4.11 seem less affected after the test run in this setting. As the grid of the FRAUENTHAL MK20 ceramic, the grid of the NGK ceramic is partly clogged. The small grid size in both cases might favor this phenomenon. Since the beneficial influence of the small grid size on the saturation and the impact of the clogging on the flow inside the saturation chamber is unknown, more comparison tests are necessary to clarify the impact of the grid size on the saturation behavior.

In comparison to both wicks described before, this wick shows clearly more signs of usage in test setting 2 as shown in figure 4.15. Since the amount of residual oxygen in the saturation chamber should be more or less the same in all three cases, the increased degradation compared to the other wicks is probably caused by oxygen that is stored in the crystal lattice or by components that catalyze the oxidation reaction. Both explanations

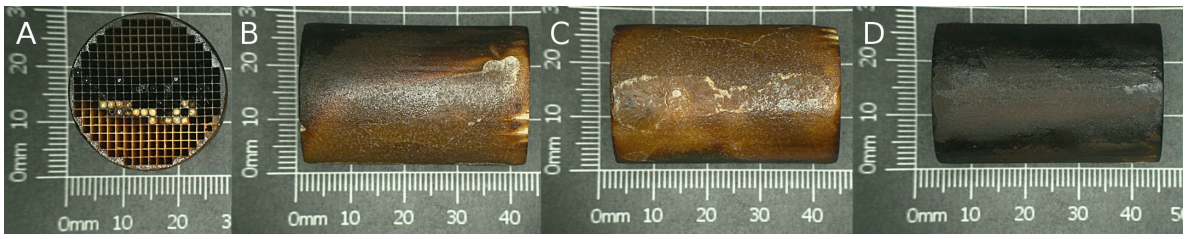


**Figure 4.14:** NGK cordierite ceramic after 18.25 h of use in setting 1: Unfiltered ambient lab air introduced at the carrier gas inlet. A) Front, B) side, C) bottom and D) top view.

might be true in this case, since the oxygen amount is unknown and the NGK ceramic contains higher amounts of Fe as well as Ti than the other two ceramics as indicated in table 4.1.

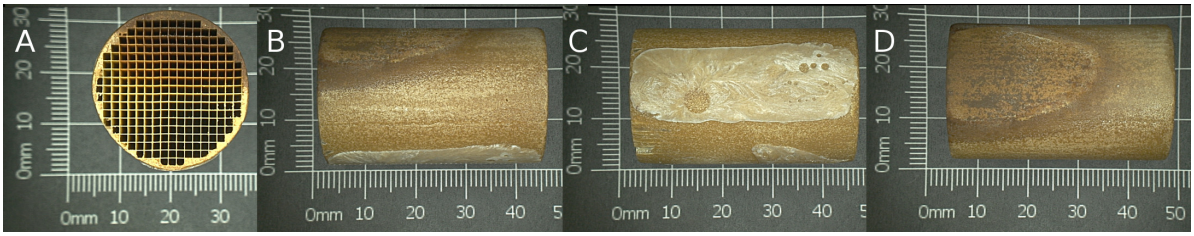


**Figure 4.15:** NGK cordierite ceramic after 18.25 h of use in setting 2: $N_2$ introduced at the carrier gas inlet. A) Front, B) side, C) bottom and D) top view.

### SiC particle filter

As shown in figure 4.16 the diesel particle filter is metallic grey with a thin-wall honeycomb structure that has a grid size of 0.95(5) mm and a wall thickness of 0.31(1) mm. Only one element with a height of 33.8(4) mm was used for the test runs.

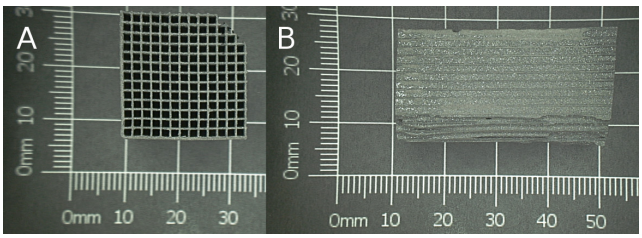


**Figure 4.16:** New SiC diesel particle filter saturator element. A) Front and B) side view.

As shown in figure 4.17 the top of the wick is still subject to heavy depositions after the test run in test setting 1. In comparison to the other wicks, the working fluid shows most signs of degradation if a SiC wick is used: The decomposition of *n*-Eicosan leads to a dark yellow to orange-brown appearance of the working fluid. Again, the honey comb

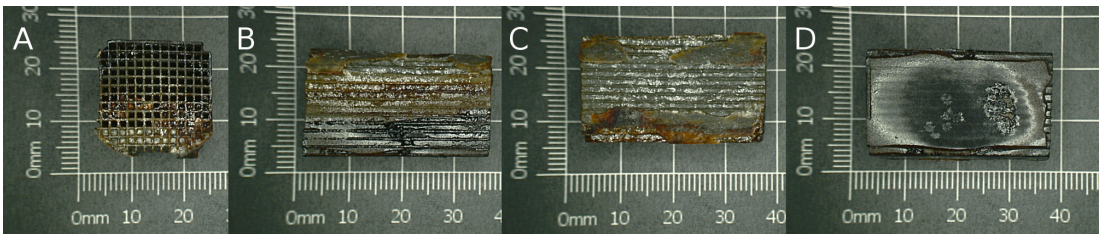


**Figure 4.17:** SiC diesel particle filter after 18.25 h of use in setting 1: Unfiltered ambient lab air introduced at the carrier gas inlet. A) Front, B) side, C) bottom and D) top view.

structure is partly clogged after the test run.

Compared to the other samples, the SiC diesel particle in figure 4.18 shows almost no signs of decomposition after the test run in setting 2. In the side and bottom view the reflecting layer of *n*-Eicosan is well visible, due to the dark material. The top view does not show the working fluid explicitly, since the reflection of the light is more evenly due to its smooth surface.

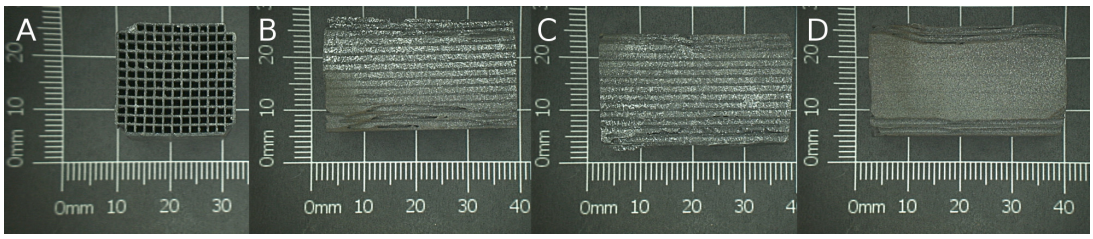


**Figure 4.18:** SiC diesel particle filter after 18.25 h of use in setting 2: $N_2$ introduced at the carrier gas inlet. A) Front, B) side, C) bottom and D) top view.

### 4.3.3 Summary of the wick tests

In summary, the test runs indicate that the degradation of the working fluid can be minimized when $N_2$ as carrier gas is used. Except of the NGK cordierite ceramic, all other wicks show only minor signs of degradation on there surfaces in test setting 2. These signs are probably linked to residual oxygen in the wick chamber. The residual oxygen alone, however, cannot explain the increased signs of degradation on the surface of the NGK wick. In this case, oxygen stored in the wick material or catalytically active components might support the degradation process.

When ambient lab air is used as carrier gas – as in test setting 1 – the constant introduction of oxygen enforces the decomposition of *n*-Eicosan. This results in brown and black depositions on the surface of all tested wick elements. Furthermore, the working fluid

appears yellow to brown. The influence of the wick material on the degradation is only qualitatively assessable by the discoloration of the *n*-Eicosan and by the depositions on the wick's surface. Thereby, FRAUENTHAL HT ceramic show the least signs of degradation, whereas the SiC particle filter shows the most in test setting 1. In case of the two cordierite ceramics, the discoloration of *n*-Eicosan is comparable, but the surface of the NGK wick shows increased depositions. According to these findings, the FRAUENTHAL HT ceramic performs best and should be considered for further use.

Overall, an operation with $N_2$ and the FRAUENTHAL HT ceramic should allow to operate the HT-CPC with minimal degradation issues.

Furthermore, the test runs revealed a high consumption of *n*-Eicosan during operation in all cases. A considerable amount of the emitted working fluid is found after each test run as condensate in the exhaust tubes as figure 4.19 shows.

**Figure 4.19:** *n*-Eicosan is emitted by the L-Type HT-CPC during operation in large amounts. The working fluid partly condenses in the exhaust tube.

In a next step, the consumed amount of working fluid has to be determined quantitatively to improve the simulation results. In addition, the changing *n*-Eicosan level inside of the saturation chamber influences the flow rate at the carrier gas inlet. Further investigations should clarify the impact of these fluctuations on the saturation conditions within the HT-CPC.

## 4.4 Static light scattering setup

The static light scattering setup used before was based on the work of Buchberger [7], but with a different detector unit[42]. As shown in figure 4.20, this previous setup utilizes a 635 nm diode laser to illuminate the scattering volume. The scattered light is detected by an photodiode detector that is mounted on a rotary table. The signal processing was done with an ADC board of an AVL particle counter: A peak count algorithm – implemented in a field-programmable gate array (FPGA) – detects the height and the amount of scattering peaks. Thereby, it automatically subtracts the background signal in an unknown way. A Matlab script was used to control the motor and to collect the data from the analog to digital converter (ADC) board. Thereby, it correlates the detector's position and the summed up height of the counted peaks as a value for the intensity.

However, the fact that the algorithm is optimized for a different setup – particle counting in a closed environment[43] – make the adaptability of the algorithm in this case questionable. Although scattering curves obtained with the CNM seemed plausible in certain settings[44], the influence of ambient as well as unintended stray light[45] and the unknown influence of the peak count algorithm made the setup highly unreliable.

### 4.4.1 Stepwise adaption of the light scattering setup

As a consequence of the findings above, the light scattering setup was modified based on the recommendations of Chu [10] and his descriptions of different laser light scattering setups. Several steps led to an adequate light scattering setup. These include the following points and all of them are described in more detail below.

1. Blackening of all surfaces to prevent stray light
2. Implementation of the laser system
3. Implementation of the detection system

[42] Buchberger used an avalanche photodiode and a Red Pitaya as detection system [7].

[43] The laser-detector as well as the optical setup is configured once and enclosed in a way that no ambient light can influence the measurement.

[44] It was necessary to tilt the detector in a certain way and mount it exactly 36 mm away from the outlet nozzle of the CNM. In addition, the laser has to be focused as precise as possible on the scattering volume above. With this setting, continuous scattering curves commonly up to 12°, in rare occasions up to 16° were obtained.

[45] Due to the open detector setup, stray light from surrounding surfaces influenced the measurement significantly. Especially, in case of the HT-CPC, stray light from the heating cap made a meaningful measurement impossible.

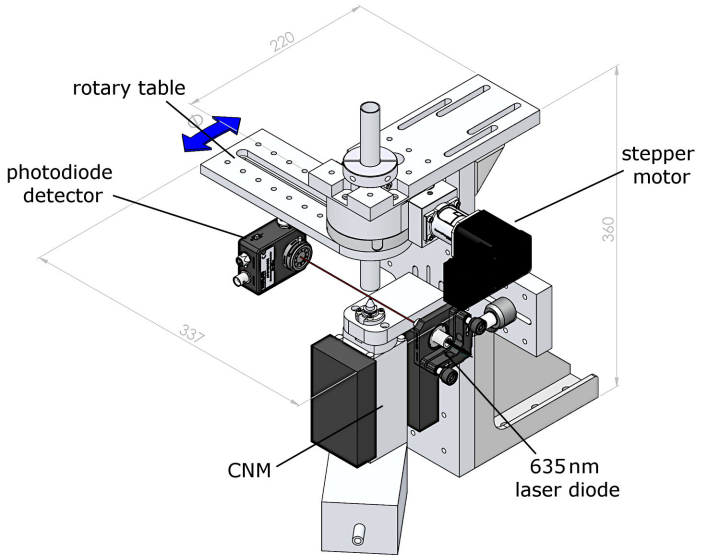


**Figure 4.20:** Previous static light scattering setup: A photodiode detector mounted on a motor driven rotary table detects scattered light at different angles.

4. Detector change from photodiode to PMT
5. Implementation of beam dump
6. Implementation of auxiliary alignment setup
7. Adaption of the laser system to PMT detector
8. Final adjustment of the light scattering setup

**Step 1: Blackening of all surfaces to prevent stray light**

Since the circuit board of the photodiode as well as the outlet nozzle acted as reflection faces for the primary laser beam, unwanted stray light reached the detector. Therefore, the surfaces were blackened and an iris aperture was implemented in front of the photodiode. Despite these alterations, stray light still reached the detector. The primary beam was reflected back by the aperture and stray light from the nozzle is captured by the photodiode. Due to the fact that the distance between outlet nozzle and photodiode could not be altered as mentioned above[46], it was not feasible to install an adequate beam dump[47].

[46] See footnote 44.

[47] Since the primary beam and the detector share an optical axis, a beam dump that blocks the primary beam also restrains the detector's view at the same time. Thus, the closer it is situated to the outlet nozzle in the center of rotation, the more it limits the detectable scattering angle.

**Step 2: Implementation of the laser system**

To obtain a scattering curve at all, it was necessary to focus the laser beam on the scattering volume right above the outlet nozzle of the CNM. Several steps were necessary to achieve this alignment: First, the focus of the 635 nm laser had to be adjusted to match the distance to the nozzle. Since the adjustment of the focus is done by a knurled nut that locks the focusing lens in place, it has to be done before the laser is mounted. Next, the laser module was mounted in the preset distance and the focus position was set by tilting the laser using a kinematic mount. Since the accuracy of the focus setting was insufficient, the laser system was adapted: Instead of a laser with adjustable focus, a collimated 532 nm laser beam was focused by a simple optical system – a plano-convex lens with a focal length of $f = 100\,\text{mm}$ – as shown in figure 4.21 onto the scattering volume. Two mounted iris apertures, one in front of the laser and one in front of the lens reduce unwanted stray light. A XY-stage was used to fine adjust the distance between the lens and the scattering volume. The focus position at this stage was still set with the kinematic mount.

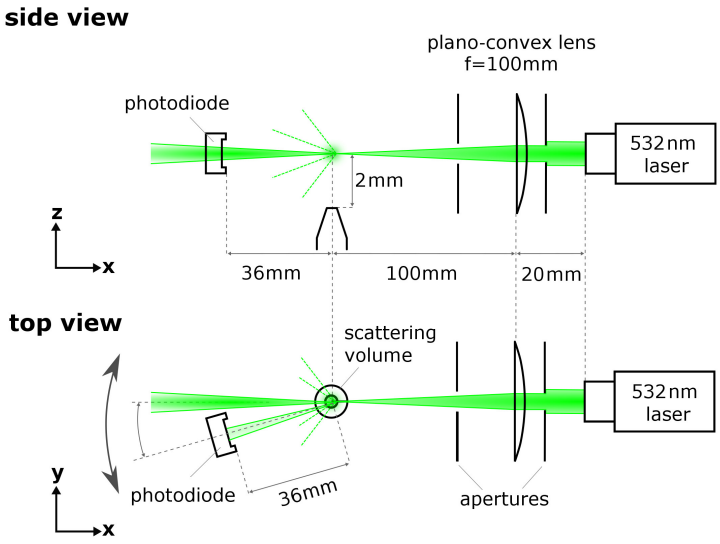


**Figure 4.21:** First implementation of an optical setup to focus the 532 nm laser beam onto the scattering volume. A photodiode detector was used to measure scattered light.

First tests of the setup with the CNM revealed that the setup was still very sensitive to the position of the laser focus. In case the laser focus is shifted along the optical axis out of its optimal position[48], the intensity clearly changes as indicated in figure 4.22A: If this

[48] In this case, the best laser position is determined by the maximizing the intensity difference $\Delta I_{\text{extrema1}} =$

shift is in the range of ±400 µm the local extrema are found at the same position and only the intensity changes. For instance, shifting the laser focus by 350 µm along the optical axis, decreases the intensity difference $\Delta I_{\text{extrema1}}$ by 44 %. Since the scattered intensity is proportional to the primary intensity, according to eq. 2.3, this decrease in scattered intensity might be a consequence of less primary intensity hitting the particles directly. Moreover, when the laser focus is shifted further, even the positions of the extrema change and the signal is lost occasionally as shown in plot.

Furthermore, also the movements of the stepper motor and the vibrations transferred to the base plate influence the measurement significantly as indicated in figure 4.22B: If the base plate is kept tight on the table, the measured intensity clearly increases and the intensity difference $\Delta I_{\text{extrema1}}$ more than doubles. As consequence, the used acrylic glass base plate was changed to a heavier solid aluminum breadboard.

The influence of the opening diameter of both iris apertures is surprisingly small. It has almost no influence on the detected intensity in this setup as shown in figure 4.23.

**Step 3: Implementation of the detection system**

In a next step a detection optic as proposed by Chu [10, pp. 165ff.] was implemented in front of the photodiode to restrict the detector's area of vision to the scattering volume only: A biconvex lens was mounted in between the outlet nozzle and the detector. In this way, the magnification ratio of the scattering volume and its image on the detector can be adjusted by the focal length of the used lens. In the focal plane of the lens an iris aperture was placed for restricting the effective scattering volume. A second aperture is placed right in front of the detector to restrict the beam divergence and to reduce the influence of unwanted stray light. In this case a biconvex lens with a focal length of $f = 25.4\,\text{mm}$ was used. It was mounted $l_1 = 40\,\text{mm}$ from the outlet nozzle and $l_3 = 65.4\,\text{mm}$ away from the detector. Thus, the scattering volume is mapped onto the detector with a magnification $M$ of:

$$M = \frac{l_3}{l_1} = 1.6 \tag{4.1}$$

The setup did not work well with the L-Type: The ADC board provided only occasionally – and on random detector positions – intensity values, although the scattering event was

$I_{max} - I_{min}$ between the first local minimum $I_{min1}$ and the first local maximum $I_{max}$.

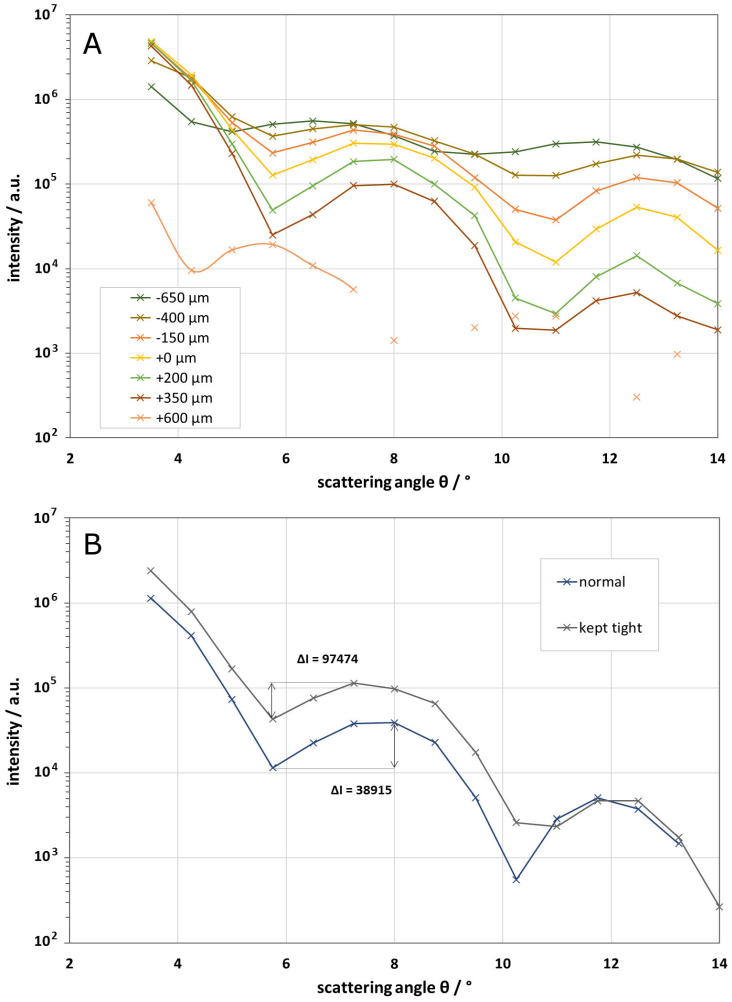


**Figure 4.22:** The influence of the position of the laser focus and of movement vibrations on the scattering intensity: A) If the focus is shifted, also the intensity decreases. If it is shifted further than ±400 µm, also the positions of the extrema change. B) The movement vibrations and the mechanical stability of the measurement setup influences the intensity reading. If the base plate is kept tight, the intensity clearly increases and the intensity difference $\Delta I_{\text{extrema1}}$ between the first minima and maxima more than doubles.

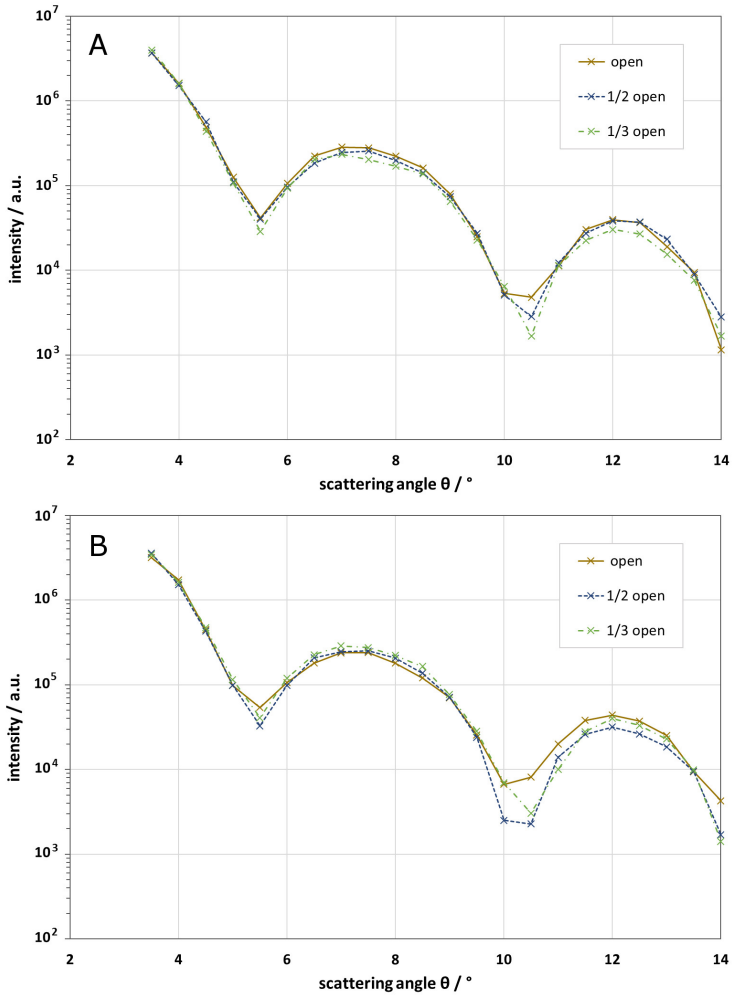


**Figure 4.23:** The influence of the opening diameter of both used iris apertures on the scattering intensity. The intensity does not change significantly A) due to the iris aperture in front of the laser nor B) due to the one in front of the focusing lens.

clearly visible with unarmed eye. Since the restriction of the detector's view also implicates that the setup becomes more sensible to its alignment, it was likely, that the alignment possibilities of the detection optic in this stage were not sufficient.

As first attempt to improve the adjustability of the detector optics, the XY-stage from the laser setup was utilized. However, due to this alteration the accuracy of the laser focus suffered and the measured data quality did not improve overall. Therefore, the usage of another XY-stage was considered and a one-axis linear translation stage was 3D-printed to allow the adjustments of the Z-position of the laser as well.

Furthermore, in cases were measurement data could be obtained, the data showed low intensity and no resemblance with a Mie scattering curve overall. It is possible that the detected peak shape was not suitable for the peak count algorithm or that the automatic background correction of the ADC board over performed and too much intensity was classified as background. Since the raw data was not accessible, the influence of the ADC board on the measurement data remained beyond control.

**Step 4: Detector change from photodiode to PMT**

Based on these findings the choice of detector was reevaluated and the ADC board as well as the photodiode was substituted by a HAMAMATSU H13320-04 photomultiplier tube. The spectral response of this PMT model matches the laser wavelength, since it peaks at 530 nm. The PMT provides a current output that is linear up to a current of 10 µA. To obtain a voltage signal a resistor with a resistance of $R = 200\,\mathrm{k\Omega}$ was utilized. The voltage drop across the resistor to ground is proportional to the output current and hence to the scattered intensity.

Due to the fact that the full width half maximum (FWHM) of a PMT response to a scattering event is in the range of 10 µs to 20 µs – as shown in figure 4.25C – a high enough sampling rate is necessary to resolve it completely: Although it is possible to distinguish PMT peaks from the background with sampling rate of 125 kS/s in figure 4.25A, they are not well defined and occasionally forked. In contrast, a higher sampling rate – as 1.25 MS/s in figure 4.25B – clearly shows the rapid rise of the PMT signal and the long decay. An attempt to sample this signal with a myRio signal processing unit and a Labview program failed due to the fact that a sampling rate of >100 kS/s could not be maintained stable over time for unknown reasons. Therefore, an oscilloscope in high resolution sampling

mode was used instead as sampling device.

Based on a typical PMT response, it was set to 1.0 V/division and 400 ms/division. By collecting $5 \times 10^6$ data points over 10 divisions – or 4 s – per sampling step, a sampling rate of 1.25 MS/s was realized. To automatically sample the voltage signal over time and at different scattering angles, a Labview program was implemented together with a coworker, J. Prats Valero. The block diagrams can be found in the appendix and the frontend is depicted in figure 4.24: It controls the stepper motor and collects data from the oscilloscope. Thus, the signal can be measured at different detector positions for a given amount of sampling steps. For each measured detector position the program calculates the integral as well as the arithmetic mean over all related values.

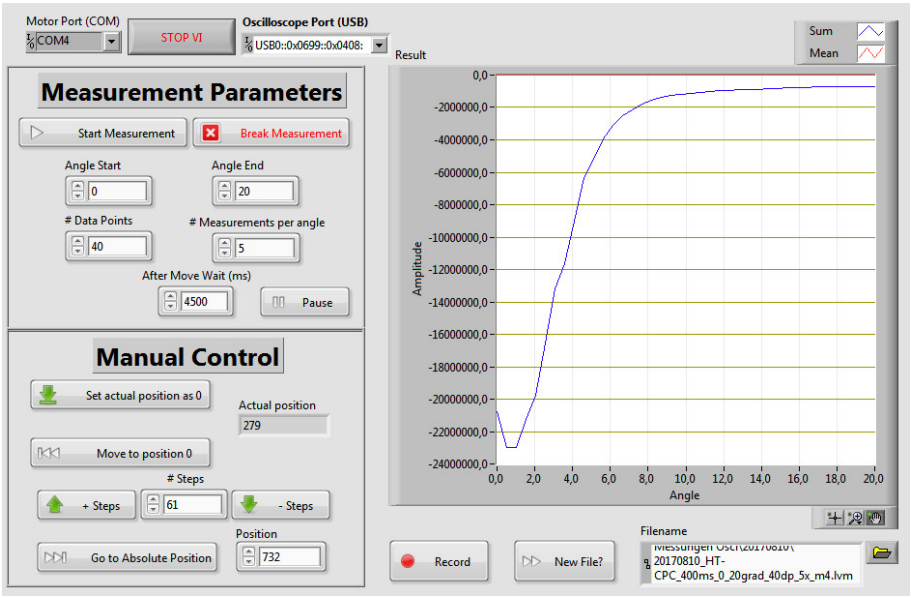


**Figure 4.24:** Front-end of the Labview program that controls the stepper motor and collects the data from the oscilloscope.

To reduce the influence of ambient as well as stray light, the PMT was coupled with an optical fiber. Since the coupling with a single-mode fiber proved to be difficult, a multi-mode fiber was used. As shown in figure 3.9, a lens is necessary to map the scattering volume onto the fiber: A biconvex lens with a focal length of $f = 35$ mm in a $2f$-setup[49] was chosen. In this way, the scattering volume is mapped one-to-one onto the fiber, while the core diameter of 50 µm acts as a delimiter of the detector's area of vision. The opening angle of the detector system is set by an iris aperture. The axis of this optical setup lies within the scattering plane.

[49] The distance between lens and fiber core as well as between lens and outlet nozzle is $l = 2f = 70$ mm.

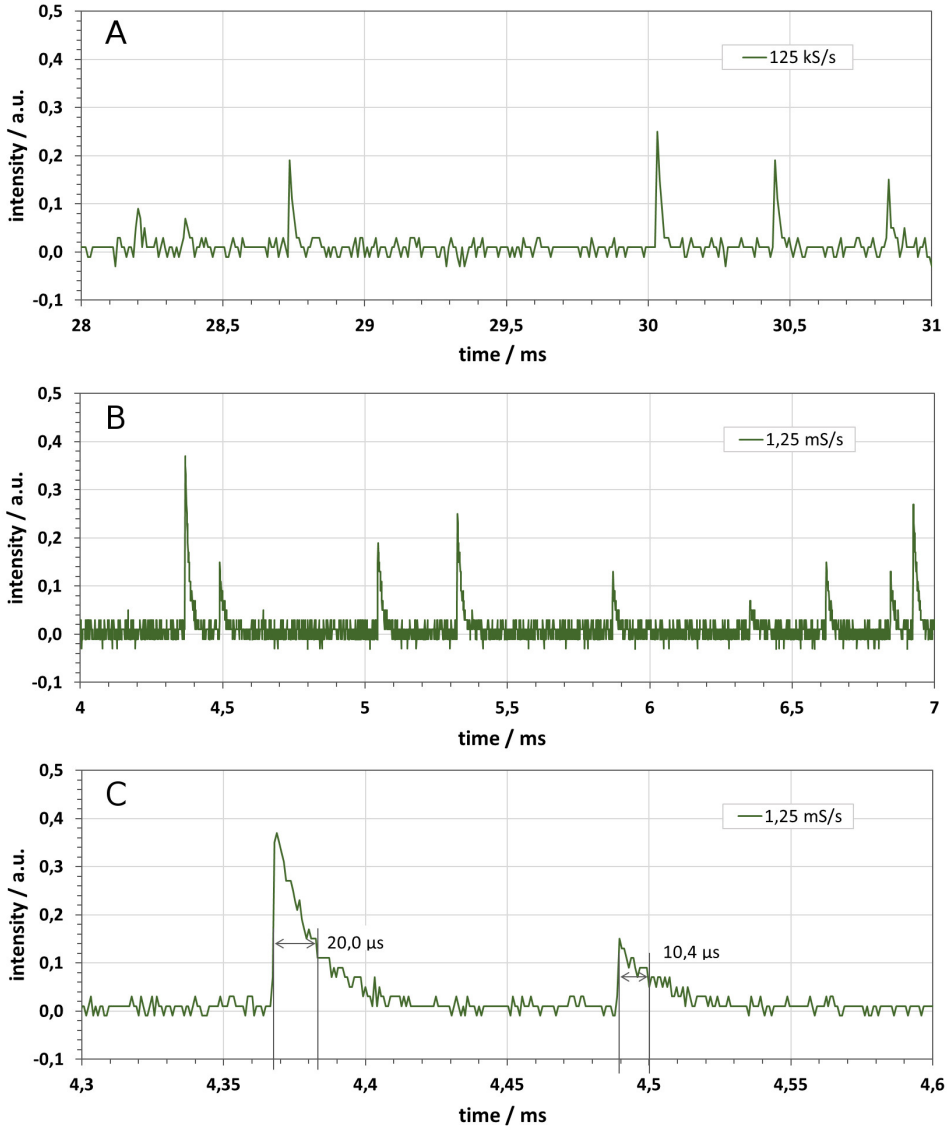


**Figure 4.25:** The PMT signal sampled with different sample rates: A) With 125 kS/s the PMT response to a scattering event is distinguishable from the background, but the peaks are not well defined and occasionally forked. B) With 1.25 MS/s these peaks are well defined and show the characteristic rapid rise and long decay clearly. C) The FWHM of a typical PMT response to a light scattering event sampled with 1.25 MS/s is in the range of 10 µs to 20 µs.

Since the alignment with the scattering event is critical, the optical setup was mounted on a XY-stage. In addition, a dovetail rail allows a rough adjustment of the distance between lens and outlet nozzle.

**Step 5: Implementation of beam dump**

Furthermore, due to the extended distance between lens and outlet nozzle, it was possible to install a beam dump. As first attempt, a rather large beam dump was mounted slightly below the scattering plane. To ensure that the laser hits the beam dump it was tilted by 4°. Although this setup worked very well with the CNM – since the beam was absorbed efficiently and the detector's line of sight was not interrupted at all – the setup was not feasible in case of the HT-CPC. Therefore, a smaller beam dump was designed and installed along the optical axis of the detector at $\theta = 0°$. It was mounted as far away from the center of rotation as possible. Nonetheless, it not only blocks the primary laser beam, but also the detector's line of sight at scattering angles below 3.5°.

**Step 6: Implementation of auxiliary alignment setup**

To align the setup, the CNM was operated with standard settings as stated in chapter 3.2. Despite the above mentioned alignment aids, it was difficult to find the optimal detector position. Therefore, the optical setup was used the other way around and the PMT was substituted by the laser. In this way, the end of the fiber can be mapped onto the scattering volume. Since a biconvex lens was used, the focal point should be very similar for both directions. To increase the coupling efficiency, an auxiliary setup including a plano-convex lens with a focal length of $f = 50\,\mathrm{mm}$ mounted on a kinematic mount was used to focus the laser beam onto the fiber's end. In this way, the intensity at the scattering volume is sufficient to observe the scattering event with an unarmed eye. By minimizing the beam diameter there, the $2f$-setup can be optimized easily. Furthermore, it is possible to check if the scattering volume is in the center of rotation, by rotating the detector optics to several scattering angles. At all angles, the scattering event should be visible.

**Step 7: Adaption of the laser system to PMT detector**

Once the detector optic is aligned with the scattering volume, the particles within have to be hit by the 532 nm laser beam. Therefore, the beam was focused by a plano-convex lens with a focal length of $f = 200\,\text{mm}$ onto the scattering volume. Thereby, two apertures constrain the laser beam. A spatial filter as described by Chu [10, p. 198f.] had not been implemented until this point, since no suitable lenses were available. However, to improve quality of the primary intensity beam, a spatial filter is highly recommended for small angle light scattering measurements and should be implemented as part of future modifications.

Furthermore, it was necessary to decrease the laser's intensity, since the PMT is quite sensitive. An absorptive neutral density filter with an optical density of OD = 0.3 was used to reduce the primary intensity. To ensure that the PMT's output is in its linear range[50], the control voltage of the PMT has to be adjusted. Depending on the oscilloscope reading during the alignment procedure, 0.6 V to 0.7 V were applied. Since the setup is very sensible to the focus position, two linear translation stages were used. They allow the adjustment of the position of the focus along all three axes. Thus, by moving the laser setup in Z-direction it is possible to align the optical axis of the laser system with the one of the detector. In this setting, the primary beam will also hit the beam block.

**Step 8: Final adjustment of the light scattering setup**

To fine tune the alignment, the readout of the oscilloscope was used: At two different scattering angles, 3° and 8°, the PMT signal level was locally maximized by adjusting the laser as well as the detector position systematically. If the outlet nozzle is not in the center of rotation, it is not possible to maximize the levels at both positions at the same time.

To ensure that the maximum PMT output is in the linear regime – below 2 V – the control voltage was adjusted accordingly. In most cases, it was set to 0.60 V to 0.65 V.

The final implemented scattering light setup is shown in figure 4.26. It is placed inside an optical enclosure that blocks all ambient light and acts simultaneously as fume hood.

[50] The linear range of the used PMT is up to 2 V.

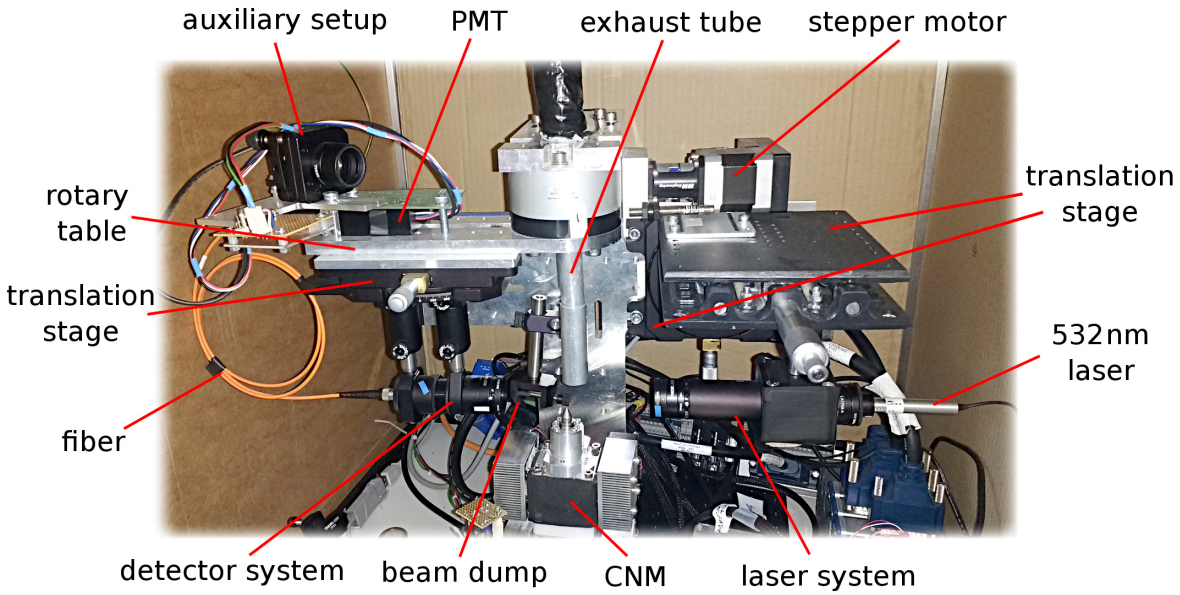


**Figure 4.26:** The final implemented scattering light setup. It is placed inside an enclosure that blocks ambient light and acts as fume hood, since the hood is directly connected to the local exhaust ventilation.

### 4.4.2 Laser stability issues

Occasionally, disproportional jumps in the intensity reading disturb the measurements. To evaluate the impact of the laser in this regard, four long term measurements with a power meter in a darkened room were conducted. Most of them show that – after the start-up phase of about 250 s to 350 s[51] – the laser's intensity becomes stable. However, in one case the laser's intensity does not become stable at all as shown in figure 4.27A. Instead it increases slowly after the startup phase by approximately 8 %. This rise is interrupted once by a 2 % intensity drop. This behavior indicates that the used laser diode module might be mode hopping due to changes in the laser's temperature [21]. A monitoring of the laser's intensity in combination of the temperature of the laser's housing under the enclosure of the light scattering setup supports this finding. Moreover, figure 4.27B shows that the local exhaust ventilation influences the temperature of the laser housing and hence has an impact on the laser stability: Again, the intensity of the laser becomes stable after approximately 330 s. During this start-up phase the temperature of the laser's housing slowly increases. If the local exhaust ventilation is turned on, the ambient temperature

[51] According to the product data sheet of the laser module, it should only take half as long, since it should be less than 2 min [42].

in the enclosure as well as the laser's housing temperature decline and begin to oscillate slightly. The big thermal mass of the inactive CPC remains unaffected. With the decrease in temperature also the laser's intensity slowly decreases by approximately 4 %. While the temperature of the laser housing becomes quite stable, the intensity starts to increase until it suddenly drops again by about 1 % when the laser's wavelength shifts. As shown in the plot, this is a recurrent behavior. Although the test was done without a running CPC, it is very likely that the proximity of a heated device like the HT-CPC will influence the temperature of the laser's housing as well.

A possible solution would be to insulate the laser. Thereby, its sensitivity to temperature changes caused by the ventilation should be reduced. However, the sudden intensity drop that occurs from time to time seems to be a inherent property of the used laser module. Hence, it is necessary to log the primary intensity in future or change to a temperature controlled laser for accurate light scattering measurements.

### 4.4.3 Light scattering measurements with the CNM

After the alignment of the setup, light scattering measurements were successfully conducted with the CNM. The measurement parameters are listed in table 3.1. As stated, two main configurations were used: Configuration 1 with ambient lab air as sample gas to determine the scattering of particles in the lab air and configuration 2 with HEPA fitered air as sample gas to determine the background signal. In both cases, the measured intensity was cumulated over five samplings steps at each detector position. To show the stability, the average of three measurements in configuration 1 and of two measurements in configuration 2 were calculated and plotted in figure 4.28A. In configuration 1, the first and second intensity maxima/minima are clearly visible. In case of configuration 2, there are no distinct minima and maxima and the overall intensity is significantly reduced due to the lack of particles as nucleation seeds. Hence, the intensity extrema visible before are a consequent of light scattered from particles within the scattering volume.

The error bars representing the standard deviation indicate good reproducibility of the measurements[52]. Based on the background corrected scattering curve shown in fig-

[52] Measurements with random intensity fluctuations as described in chapter 4.4.2 have not been taken into account here.

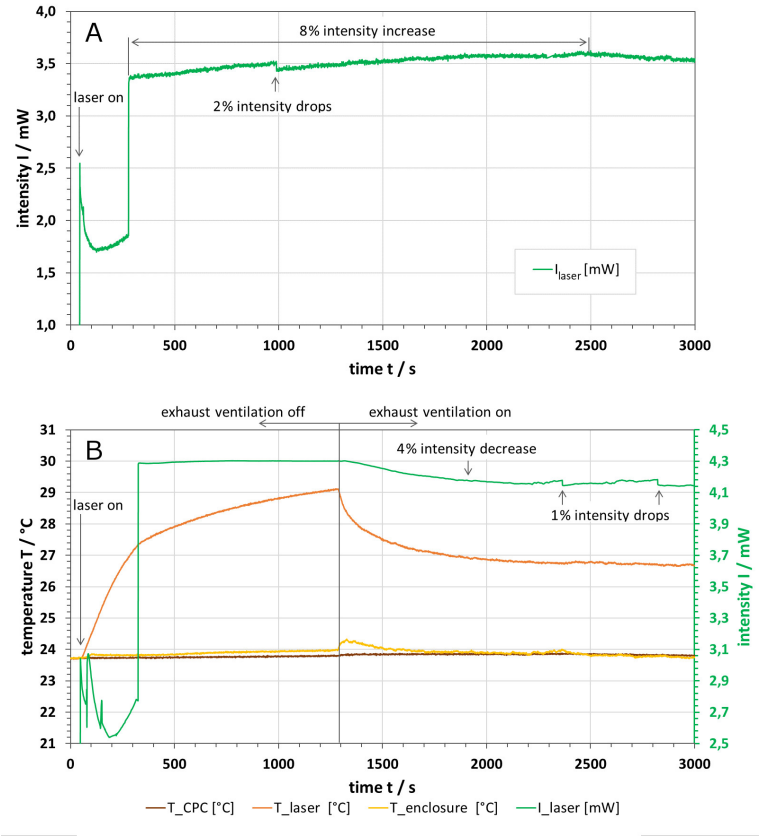


**Figure 4.27:** Long term stability tests with the used 532 nm laser module in a dark room: After power on, it normally takes the laser up to 350 s to stabilize its output intensity. A) In one out of 4 cases, no stable output was reached. Instead the laser's intensity continuously increases for approximately 2200 s and suffers one sudden drop due to mode hopping. B) Similar drops occur if the local exhaust ventilation influence the temperature of the laser housing. After the exhaust ventilation is turned on, the housing temperature and with it the output intensity decreases. At a certain point the temperature becomes stable, but intensity fluctuations due to mode hopping begin to occur.

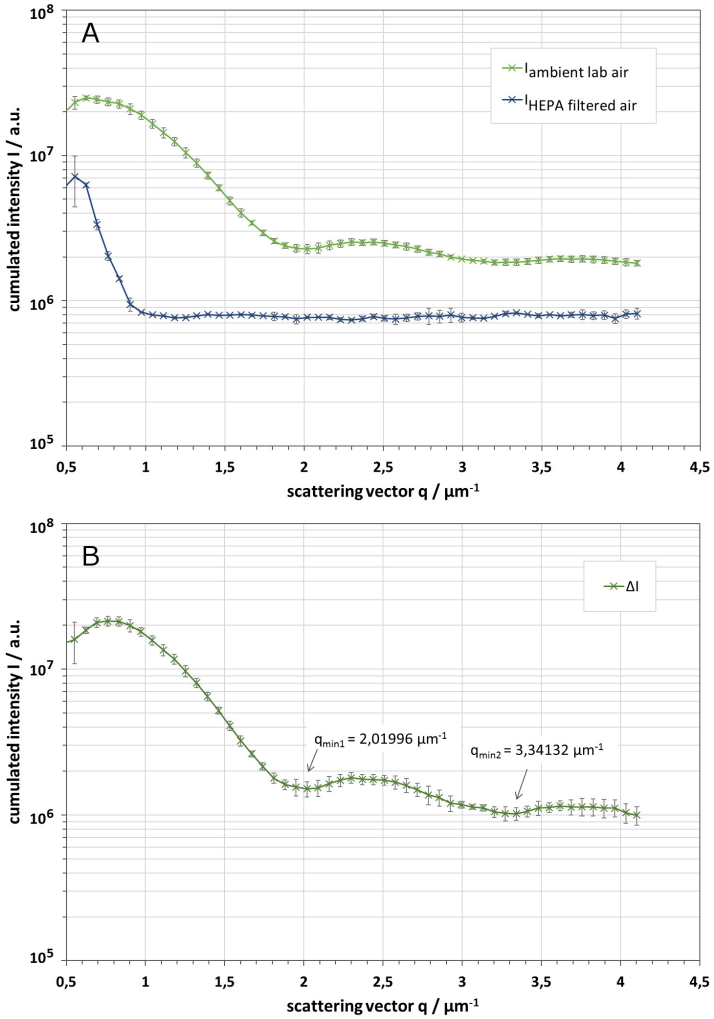


**Figure 4.28:** Light scattering measurement with the CNM: A) The average scattered intensity $I_{\text{ambient lab air}}$ from particles in ambient lab air based on the cumulated intensity values of three independent measurements. As background signal, the average scattered intensity $I_{\text{HEPA filtered air}}$ with HEPA filtered air as sample gas based on two independent measurements is shown. B) The background corrected scattering intensity $\Delta I = I_{\text{ambient lab air}} - I_{\text{HEPA filtered air}}$ based on the cumulated intensity values in plot A. The scattering vectors of the two minima are labeled.

ure 4.28B, the positions of the first two minimum are determined to:

$$q_{min1} = 2.02\,\mu m^{-1} \qquad q_{min2} = 3.34\,\mu m^{-1}$$

Based on theses positions and according to eq. 2.17 the radius can be estimated to:

$$R_{min1} \approx 2.22\,\mu m \qquad R_{min2} \approx 2.32\,\mu m$$

In addition, also the Guinier approximation as described in chapter 2.4.4 yields an estimation of the radius. By plotting the background corrected intensity values of figure 4.28B in a Guinier plot, the linear relation in the Guinier regime was revealed as shown in figure 4.29. As depicted, the linear regime can be fitted quite nicely with a narrow 95 % confident range. The slope of a linear fit is used to determine the radius of the spheres according to eq. 2.23 and eq. 2.26 to:

$$R_{guinier} = 2.35\,\mu m$$

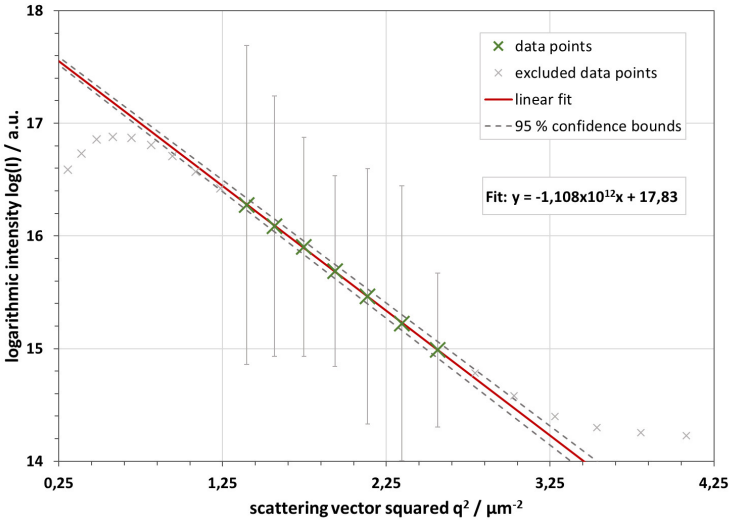


**Figure 4.29:** Guinier plot of the background corrected intensity data of figure 4.28A.

Both size estimations deliver comparable results, indicating that the light scattering setup works as intended. Unfortunately, the determined particle size does not coincide well with similar measurements: According to scattering measurements conducted by Cresnoverh [12] the radius of the emitted particles by the same CNM should be in the range of 3.7 µm to 4.8 µm if the devices temperatures are set to $T_{condensor} = 29\,°C$ and $T_{saturator} = 38\,°C$ – hence for a temperature difference of $\Delta T = 9\,K$. However, the results presented above, are valid for a temperature difference of only $\Delta T = 8\,K$. In general, a smaller tempera-

ture difference leads to a decreased condensational growth and in further consequence to smaller particles at the aerosol outlet. Further measurements with different $\Delta T$ between condensor and saturator should be conducted, to determine the temperature dependency of the CNM on the particle size. Whether the different operation settings alone can explain the particle size difference is an open question. Due to the limitations of the setup used by Cresnoverh[53] the here presented results seem more plausible. However, also the here presented setup has a mechanical disadvantage that might result in a systematic measurement deviation: As figure 3.8 shows, the laser system is attached to the translation stage by a single pole only. There is a risk that the axis of the laser got rotated unintentionally in the x-y-plane during the alignment procedure. In this case the axis of the laser and of the detector does not coincide anymore and it would have been necessary to correct the scattering angle by the angle of rotation. An unintended rotation of the laser of approximately 4° would shift the extrema in a way that the size estimations – based on the minima positions – coincides well with the results found by Cresnoverh. By realizing a similar attachment to the translation stage as on the detector side – three poles mounted on a linear rail – the orientation of laser's axis would be secured.

### 4.4.4 Light scattering measurements with the HT-CPC

Analog to the described measurements with the CNM, light scattering measurements with the L-Type HT-CPC – configured as stated in table 3.1 – were conducted. The sample was introduced at the carrier gas inlet, since the operation of the L-Type in setting 3[54] is unstable as described later in chapter 4.3. Due to the heated hood of the L-Type and the elevated operating temperature the alignment procedure is challenging: On the one hand, the hood conceals the scattering event in a way that the alignment of the laser and detector axis becomes complicated. Therefore, the alignment procedure was done with the CNM instead and it was later substituted by the L-Type. On the other hand, the centering of the outlet nozzle of the L-Type is difficult: It is not possible to align the device in cool condition, since all components expand slightly during the heating. This expansion results in a noticeable shift of the nozzle position, since the L-shaped geometry – the nozzle sits literally at the end of a lever – amplifies the deflection. In hot condition, precise movement of the device becomes more difficult, since the device

[53] As Cresnoverh [12, p. 59] states his measurements might be influenced by ambient light and by the fact that the nozzle was not perfectly centered.

[54] $N_2$ is introduced at the carrier gas inlet while lab air is introduced at the sample inlet.

is hot and quite heavy. Therefore, it was centered by slightly tapping the base of the device to the approximate position. The fact that a slight pressure to the side of the device increases the PMT output signal significantly, indicates that this is not sufficient. A translational platform would improve the accuracy of the positioning effectively and is strongly recommended for further measurements.

Still, it was possible to conduct first scattering measurements. The curves are not as defined and reproducible as with the CNM and local extrema are hardly recognizable as shown in figure 4.30. However, the influence of particles as nucleation seeds is still clear. While using a HEPA filter, the intensity drops significantly and every indication to the intensity extrema is lost. Hence, the light scattering setup also works in case of the HT-CPC. However, measurements with the L-Type are not reliable yet. As shown in figure 4.30A the resulting scattering curves change clearly over operating time: The first measurement after the alignment procedure after a total run time of the CPC of $t_r = t_a$ min[55] shows two plateau-like features in $I_{\text{ambient lab air}}$ that might be blurry scattering extrema. The background measurement after $t_r = t_a + 50\,\text{min}$ shows a surprisingly low intensity for small scattering vectors $q$. Otherwise, it is comparable to the background measurements with the CNM. The slightly lower intensity values for high $q$ is a result of the lower PMT control voltage that is applied in this case. The measurements after $t_r = t_a + 90\,\text{min}$ and also the one after $t_r = t_a + 120\,\text{min}$ do not resemble the first curve anymore. After a total run time of $t_r = t_a + 150\,\text{min}$ and also after $t_r = t_a + 180\,\text{min}$ scattering curves became quite linear as shown in figure 4.30B. This and the increase in intensity might be due to a change of the working fluid level inside the saturation chamber, since $n$-Eicosan was refilled before these measurements. A low working fluid level might be also the reason for the low background intensity readings at small $q$.

After $t_r = t_a + 260\,\text{min}$ the scattering curve change completely as shown in figure 4.30C: There are local extrema and the intensity is increased by an order of magnitude for high $q$. It might be that a high amount of scatterers were emitted from the device during this measurement. The subsequent measurement after $t_r = t_a + 2900\,\text{min}$ still shows local extrema, but the intensity has dropped significantly and decreases completely differently with increasing $q$. After $t_r = t_a + 320\,\text{min}$ the intensity is close to the range of the background intensity.

[55] Since the run time until the end of the alignment procedure is unknown, it is expressed as variable $t_a$. All measurements were done with the same settings and the same wick.

In all these curves the influence of the degradation of the working fluid might become visible. As documented in chapter 4.3, the working fluid degrades over time, when the L-Type is used in the current operational setting. In addition, the working fluid level in the saturation chamber is continuously decreasing during operation. Both effects can influence the condensation process inside the HT-CPC and might explain the change of measured intensity over time in case of ambient air as sample gas. These effects show less impact, when HEPA filtered air is sampled, since no nucleation seeds are introduced. This is also reflected in the plotted background intensity curves shown in figure 4.30A-C. All background measurements yield very similar intensity values for $q > 1.3\,\mu m^{-1}$, which are comparable to those found with the CNM. For small $q$ the intensity values increase over time. However, compared to measurements with the CNM the intensity values in this region are expected to be higher and therefore they should be re-evaluated.

Furthermore, the possible impact of the HT-CPC on the laser's stability has to be kept in mind. As mentioned in chapter 4.4.2 above, the close proximity of the heated device to the laser, might additionally disturb the laser's stability and hence influence the primary intensity. This could be the reason for the kinks in figure 4.30A and B.

Due to these reasons, the here presented measurement results of the HT-CPC can only be preliminary. For more reliable results further modifications are necessary that ensure a stable operation of the HT-CPC during the measurement.

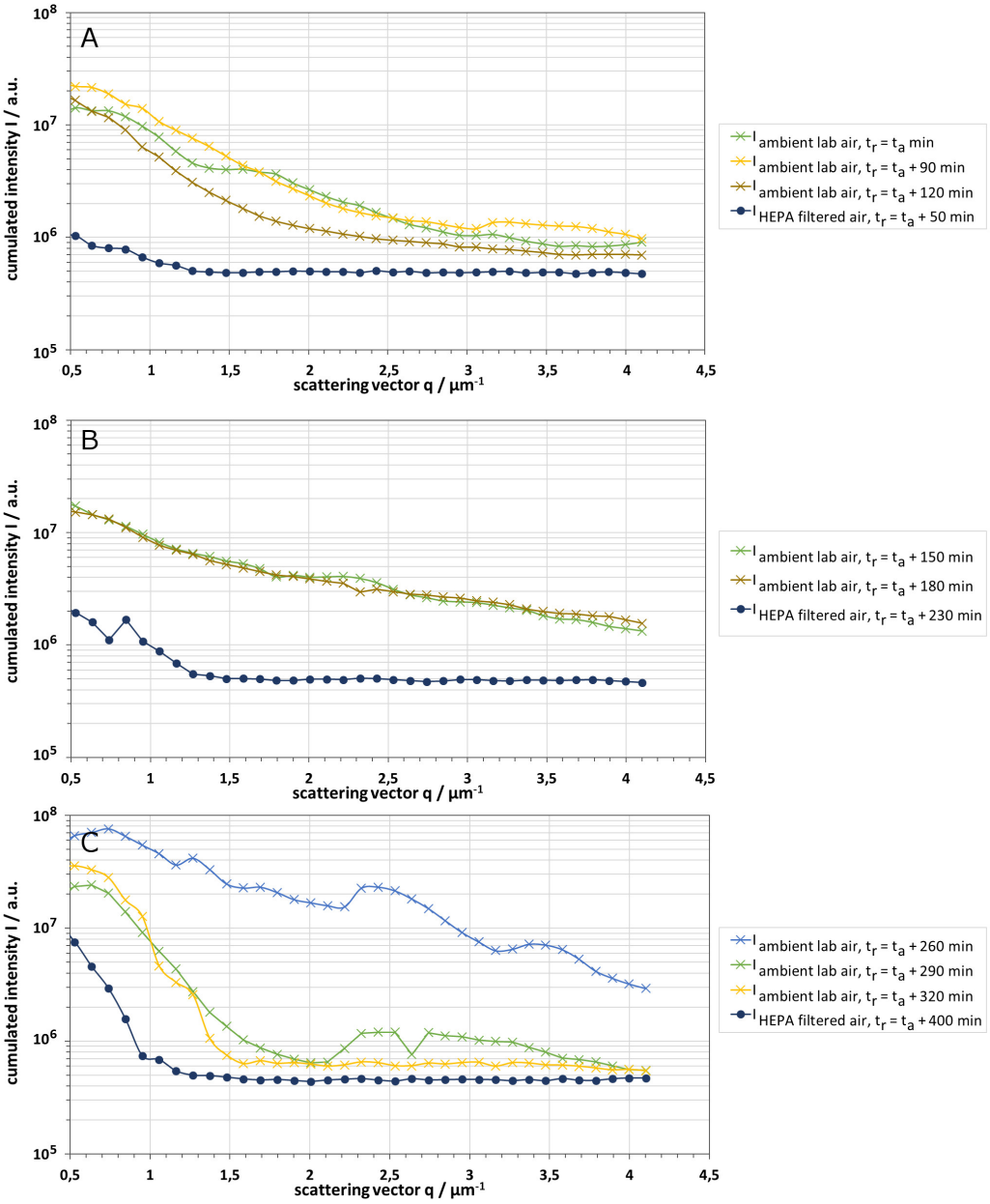


**Figure 4.30:** Light scattering measurements with the L-Type HT-CPC over time. The total run time $t_r$ of the HT-CPC is stated for each measurement (Since the duration of the alignment procedure is unknown, it is added as variable $t_a$). As shown, the measured intensity $I_{\text{ambient lab air}}$ is influenced by the changing condensation conditions inside the HT-CPC, when ambient air is sampled. The intensity $I_{\text{HEPA filtered air}}$ do not show this influence, since no nucleation seeds are introduced in case of background measurements.
A) The first measurement of $I_{\text{ambient lab air}}$ after the alignment after $t_r = t_a$ shows two plateau-like features that might be scattering extrema. B) After $t_r = t_a + 150\,\text{min}$ the decline of $I_{\text{ambient lab air}}$ is quite linear. C) The scattering curve of $I_{\text{ambient lab air}}$ after $t_r = t_a + 260\,\text{min}$ shows no resemblance with all other curves: There are local extrema visible and the intensity is increased significantly. $I_{\text{ambient lab air}}$ of the following measurements is decreasing differently with increasing $q$ than seen before.
A-C) All background measurements yield very similar intensity values $I_{\text{HEPA filtered air}}$ for $q > 1.3\,\mu\text{m}^{-1}$. For small $q$ the intensity values seem to increase over time.

# CHAPTER 5

# Conclusion and Outlook

Two obstacles of current research on HT-CPCs were addressed in this thesis. First, the degradation of working fluid during operation and second the implementation of a static light scattering setup that is adequate for scattering measurements with a HT-CPC. Before these two points could be addressed, modifications of the used L-shaped and T-shaped HT-CPCs – two designs developed by Kupper et al. [32] – were necessary, since they were prone to leakage due to the modular design as figures 4.1 to 4.3 show. In case of the L-Type, mechanical modifications, using seal tape between all components and the preventive tightening of all screws before every test run could reduce the leakage to a minimum that should not influence light scattering measurements by any means. In case of the T-Type, the heavy leakage in the connection region was not manageable. Consequently, the T-Type HT-CPC was not used any further and all tests were done with the L-Type. To evaluate the degradation of saturator elements during operations as observed by Kupper et al. [32], long term tests of four potential wick materials were conducted:

- IBIDEN FRAUENTHAL HT ceramic
- IBIDEN FRAUENTHAL MK20 cordierite ceramic
- NGK cordierite ceramic
- SiC diesel particle filter

A XRF analysis of these ceramics revealed that both cordierite ceramics contain Fe – a

catalytically active element – and Ti – a known carrier element that supports the catalytic component – in higher amounts than the FRAUENTHAL HT ceramic. These elements might accelerate the degradation process in case of the cordierite ceramics.

All wick materials were long term tested for 18.25 h in two settings, once with ambient lab air and once with $N_2$ as carrier/sample gas. The performance was evaluated qualitatively based on the figures 4.6 to 4.18. On the one hand, test runs with ambient lab air showed clearly that working fluid is degrading in the saturation chamber due to increased oxidation by the introduced oxygen over time. Thereby, the working fluid changes its appearance from white to yellow-brown. In addition, degradation products are deposited on the used wicks and form a brown to black layer that appears like an enamel and might seal the surface of the wick. In further consequence, this layer might influence the saturation inside the saturation chamber.

The majority of the test runs with $N_2$, on the other hand, showed no discoloration of the working fluid and only minor depositions of degradation products at the top of the used wick elements. These degradations might be the result of residual oxygen in the saturation chamber at the beginning of the test runs, since it was not purged with $N_2$ beforehand. An exception to these findings was the NGK cordierite ceramic, since the wick material also showed increased depositions when operated with $N_2$. These depositions in this test setting might be due to oxygen that is stored in the crystal lattice or due to material components that catalyze the oxidation reaction. In summary, all tested materials except the NGK cordierite ceramic seem equally suitable as wick material, when $N_2$ is used as carrier gas. In case of ambient lab air as carrier gas, the FRAUENTHAL HT ceramic showed clearly the least signs of degradation after 18.25 h, while the SiC particle filter showed the most. In this regard, ceramic wicks might be not the optimal choice, since their metal compounds can influence the degradation of the working fluid catalytically. An alternative might be porous non-metallic materials, for instance glass wool or porous glass.

Furthermore, the wick tests revealed several issues with the L-Type HT-CPC in its current state. On the one hand, a high consumption of *n*-Eicosan is observed during the test runs. The quickly changing *n*-Eicosan level inside of the saturation chamber influences the flow rate at the carrier gas inlet. Further investigations should clarify the impact of these fluctuations on the saturation conditions within the HT-CPC and determine the consumed amount per hour quantitatively to improve the simulation accuracy. On the other hand, the tests revealed that the operation of the L-Type HT-CPC is not always

stable with the currently implemented flow control. The L-Type is designed to introduce $N_2$ as carrier gas at the carrier gas inlet, while the sample gas is directly injected into the condensor through a capillary. In this way, no oxygen is introduced into the saturation chamber and hence only minor degradation of the working fluid can be expected. A test with FRAUENTHAL HT ceramic in the described operating setting supports this claim as indicated in figure 4.8. At the same time this test showed issues at keeping the flow rate at the aerosol inlet stable. It repeatedly drops from $0.3\,\mathrm{L\,min^{-1}}$ to almost zero for a short time during operation. These fluctuations might be a result of a capillary that gets clogged from time to time due to condensation. If this reasoning is applicable or if there are other reasons for the fluctuations must be clarified before this operating mode can be used further.

In summary, the long term tests of several wick material showed that degradation of the working fluid is inevitable with air as carrier gas, since the introduced oxygen as well as the boosts the oxidation process. Instead, the degradation can be minimized by using $N_2$ as carrier gas. When the aerosol is introduced at the aerosol inlet – as intended by the design of the L-Type – this would be possible, but the test runs revealed issues with maintaining a stable flow rate through a capillary with the current flow control. For a stable operation of the HT-CPC it is necessary to resolve this issues.

To determine the size of the emitted particles and to evaluate the performance of the HT-CPC, a static light scattering setup is necessary. Scattering measurements with the L-Type HT-CPC and a rudimentary setup containing only a diode laser and a detection unit – consisting of a signal processing board that reads out a photodiode detector and processes the data in an unknown way – were not successful. Stray light from the heating cap of the L-Type and an unknown background correction algorithm made reproducible measurements impossible. Therefore, an new light scattering setup was established that allows direct access to the scattering signal.

A CNM was used to align and test the new setup and first scattering measurements were conducted successfully. Scattering curves with clear distinctive local extrema were recorded while sampling ambient lab air as shown in figure 4.28. Based on the Guinier regime and the location of the first two local minima the size of the emitted particles was estimated to be around 2.22 µm to 2.35 µm as shown in chapter 4.4.3. These estimations, however, seem to be rather low compared to similar measurements described in literature that states a range of 3.7 µm to 4.8 µm [12]. One reason for this disagreement might be

that the experiments were conducted with different temperature differences $\Delta T$ between condensor and saturator. Therefore, further measurements with different $\Delta T$ should be conducted, to determine the temperature dependency of the CNM on the particle size. Whether the different operation settings alone can explain the particle size difference is an open question. Another reason, might be a systematic measurement deviation, for instance due to a not perfectly aligned laser-detector axis. This could be the case, since the laser system is prone to unintentional tilting in the current implementation. To avoid this tilting in future setups, the laser's axis can be secured by altering the mounting construction of the laser system. In addition, the implementation of a spatial filter in the laser system is highly recommended, to improve the quality of the primary intensity beam. Furthermore, occasional measurement deviations with the CNM indicate that the intensity of the used 532 nm diode laser module is drifting over time. As depicted in figure 4.27, the local exhaust ventilation influences the temperature of the laser's housing and with it the emitted intensity. It increases or decrease slowly and occasionally even drops suddenly due to mode hopping. Therefore, it is necessary to log the primary intensity or change to a temperature controlled laser to accomplish accurate light scattering measurements in future.

First light scattering measurements with the L-Type HT-CPC were also conducted successfully. The local extrema of the obtained scattering curves are less distinct than with the CNM, but the measured intensity is clearly tied to particle scattering. If no particles are introduced, the measured intensity is significantly reduced and no distinctive extrema can be identified. These background measurements coincide well with each other as the comparison of three measurements of HEPA filtered air in figure 4.30A-C indicate. However, these plots also show that reproducible particle size estimations are not possible yet, since the measured scattering intensity varies from measurement to measurement if ambient lab air is sampled. These variations might be caused by the following issues: On the one hand, the working fluid level inside the saturation chamber changes over time. This leads also to a varying flow rate at the carrier gas inlet as the wick long term tests have indicated. In both cases, the condensation conditions inside the L-Type HT-CPC change over time. This can be prevented by implementing an automatic refill control that keeps the working fluid at a constant level. Due to the fact that currently air has to be used as carrier gas also the degradation of the working fluid as well as the depositions of these degradation products on the wick's surface, influences the saturation condition in an unknown way. When the aerosol is introduced as intended at the aerosol inlet via a

capillary – and by using $N_2$ as carrier gas in combination with an adequate wick as stated above – most of the decomposition in the saturation chamber can be prevented. Therefore, it is essential to achieve a stable operating mode without the currently occurring fluctuations of the flow rate at the aerosol inlet for future measurements.

On the other hand, due to the heated hood and elevated operating temperatures in case of the HT-CPC, the alignment of the light scattering setup is challenging at the moment. Here, especially the centering of the nozzle is an issue, since the device is too heavy for accurate positioning in hot condition. Therefore, it is very likely that the nozzle is slightly out of the center of rotation in all conducted measurements. The implementation of a translational platform would improve the accuracy effectively and is strongly recommended.

In summary, the following modifications are advisable to improve the accuracy of the light scattering measurements with the HT-CPC:

- Since the current used laser diode showed stability issues, it is necessary to log the primary intensity or change to a temperature controlled laser in future.
- The current mounting of the laser system is prone to unintended tilting. An adaption of the mounting construction would secure the laser's axis.
- To obtain a clean primary laser beam, a spatial filter should be implemented. It is recommended for small angle light scattering measurements.
- A translational platform to accurately align the outlet nozzle of the HT-CPC and the center of rotation of the rotary table is necessary.
- The HT-CPC should be operated with $N_2$ as carrier gas in combination with an adequate wick to minimize degradation. Therefore, it is necessary to achieve a stable introduction of aerosol directly through the capillary into the condensor in future.
- By implementing an automatic flow control, the working fluid level in the saturation chamber of the HT-CPC can remain constant. In this way, fluctuations of the flow rate during measurements can be avoided.

In addition to these modifications, the following adaptions are already in work: The oscilloscope as signal sampling unit will be substituted by a more compact solution in

future. Furthermore, a new improved HT-CPC design as well as new heating hood will be available that allows to draw the sample/carrier gas through the device instead of pushing it through. This operation mode should enhance the leak tightness and a stable operation with $N_2$ as carrier gas should become possible. Hopefully, this will be the basis for reproducible scattering measurements with a HT-CPC.

# APPENDIX

# Appendix

## A.1 Used materials and devices

**Table A.1:** Materials used for the HT-CPC setups.

| material | type |
|---|---|
| L-Type HT-CPC | demonstrator setup |
| T-Type HT-CPC | demonstrator setup |
| temperature controller | NATIONAL INSTRUMENTS cRIO-9035 |
| - heating catriges | |
| - PT100 temperature sensors | |
| working fluid | n-Eicosan |

**Table A.2:** Materials for the CNM setup.

| material | type |
|---|---|
| CNM | demonstrator setup |
| temperature controller | POHL TR-81 A-Senco |
| - peltier element | |
| - PT100 temperature sensor | |
| - solid state relay | |
| working fluid | n-Decan |

**Table A.3:** Materials used for the static light scattering setup.

| aluminum rack | |
|---|---|
| breadboard | THORLABS MB3060/M |
| cage cube | THORLABS C4W |
| cube cover plate | THORLABS B1C/M |
| dichroic film polarizer | THORLABS LPVISE2X2 |
| dovetail optical rail | THORLABS RLA150/M |
| dovetail rail carrier | THORLABS RC1 |
| ferrule clamp | THORLABS FCM/M |
| fiber adapter | THORLABS S120-FC |
| filter mount | THORLABS FH2 |
| iris apertures | THORLABS SM1D12SS |
| | THORLABS SM1D12SZ |
| kinematic mount | THORLABS KM100T |
| laser 532 nm | THORLABS CPS532 |
| laser 635 nm | THORLABS CPS190 |
| laser holder | THORLABS AD8F |
| laser power supply | THORLABS LDS5-EC |
| lens mount | THORLABS SMR1/M |
| lens tubes | THORLABS SM1V10 |
| | THORLABS SM1L05 |
| | THORLABS SM1L10 |
| | THORLABS SM1L20 |
| lens tube slip ring | THORLABS SM1RC/M |
| lenses: | |
| - biconvex f=35 mm | THORLABS LB1811-A |
| - plano-convex f=200 mm | THORLABS LA1708-A |
| - plano-convex f=50 mm | THORLABS LA1131-A |
| linear translation stage (one-axis) | 3D-printed |
| linear translation stage (two-axis) | THORLABS XYR1/M |
| neutral density filters: | |
| - OD = 0.1 | THORLABS NE01A |
| - OD = 0.2 | THORLABS NE02A |
| - OD = 0.3 | THORLABS NE03A |
| optical fiber | BRUGG FG5 |
| optical posts | THORLABS TR30/M |
| | THORLABS TR40/M |
| | THORLABS TR50/M |
| oscilloscope | TEKTRONIX MDO 3024 |
| photo multiplier tube | HAMAMATSU H13320-04 |
| plate holder | THORLABS FP01 |
| post holders | THORLABS PH30/M |
| | THORLABS PH40/M |
| power supply | TTI EL302RT |
| right-angle clamp | THORLABS RA90/M |
| rotary table | MM ENGINEERING MDT36012 |
| stepper motor | GUNDA SM17H1.3OC |

**Table A.4:** Materials used for the flow control.

| material | type |
|---|---|
| HEPA filter | PARKER BALSTON 9933-11-BQ |
| mass flow controller | VÖGTLIN red-y GCR-C3SA-BA25 |
| needle valve | CAMOZZI RFO-344 |
| Venturi pump | VACCONI-JS-40UM-60-303 |

## A.2 Composition of Ibiden Frauenthal ceramics

**Table A.5:** Typical chemical composition and material properties of three IBIDEN FRAUENTHAL ceramics: HT, NT, MK20 according to the manufacturer [23].

| | **chemical composition \ material properties** | **method** | **HT** | **NT** | **MK20** |
|---|---|---|---|---|---|
| **chemical composition** | Al2O3 | XRF | 66 % | 51.7 % | 33.8 % |
| | SiO2 | | 31 % | 42 % | 53.8 % |
| | Fe2O3 | | 1 % | 0.7 % | 1.1 % |
| | TiO2 | | 1 % | 0.5 % | 0.4 % |
| | CaO | | 0 % | 0.2 % | 0.2 % |
| | MgO | | 0 % | 0.4 % | 9.4 % |
| | Na2O | | 0 % | 0.2 % | 0.1 % |
| | K2O | | 1 % | 4.1 % | 1.1 % |
| **material properties** | bulk density [$\mathrm{g\,cm^{-3}}$] | hydrostatic method DIN VDE 0335/2 | 2,4 | 2,7 | 2,0 |
| | start of softening [°C] | PoFa testing | 1540 | 1200 | 1300 |
| | coefficient of thermal expansion @800 °C [$10^{-6}\,\mathrm{K^{-1}}$] | dilatometer | 6,5 | 6,2 | 2,7 |
| | heat capacity @100 °C [$\mathrm{J\,kg^{-1}\,K^{-1}}$] | differential thermo-calorimetry | 930 | 910 | 810 |
| | thermal conductivity [$\mathrm{W\,mK^{-1}}$] | heating wire method | 2,2 | 2,1 | 1,9 |
| | temperature shock resistance [K] | DIN VDE 0335/2 | 190 | 200 | 350 |
| | water absorption [%] | hydrostatic method DIN VDE 0335/2 | 11 | 0 | 9 |

## A.3 LabView block diagram

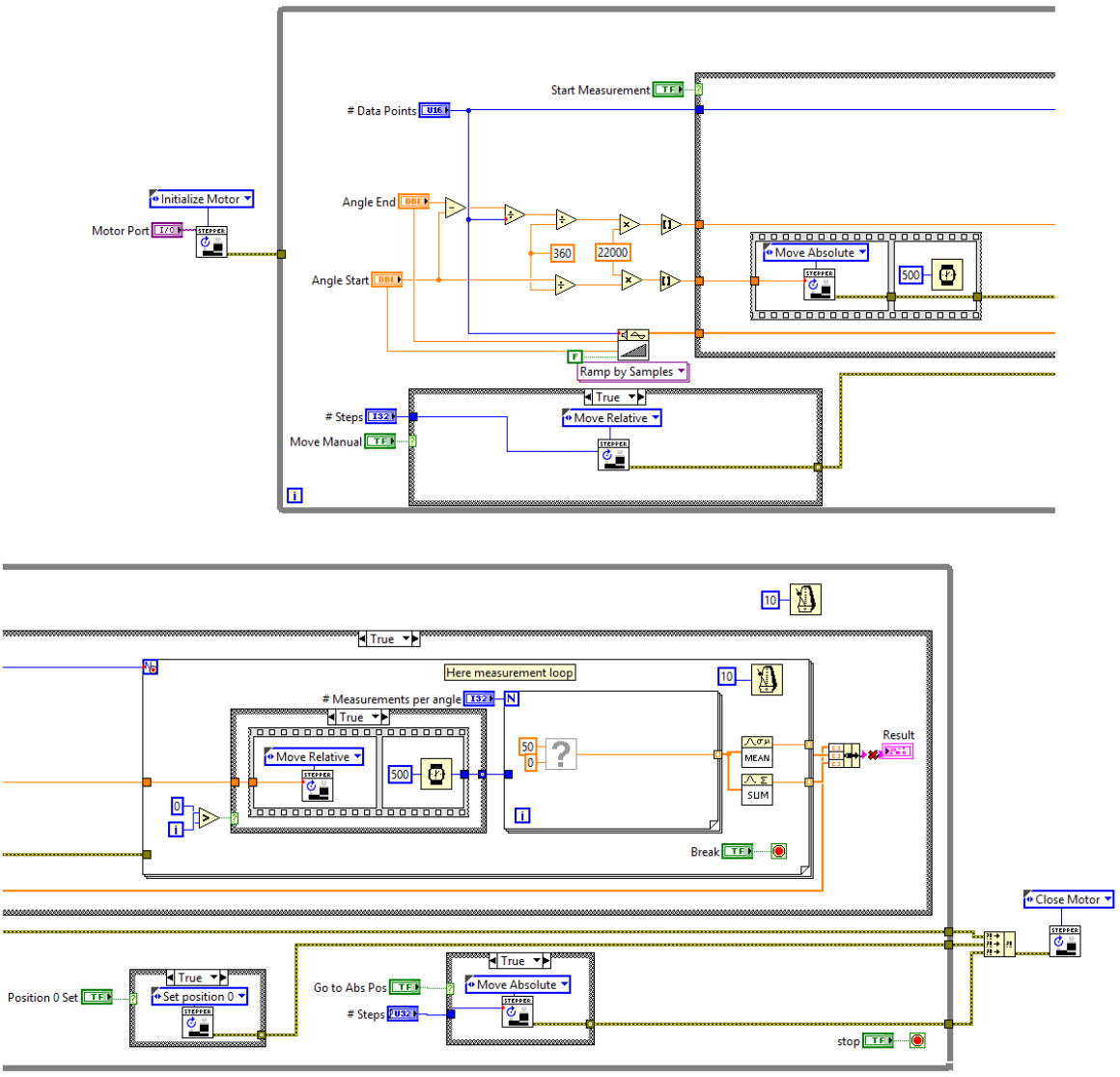


**Figure A.1:** Block diagram of the used Labview program that controls the stepper motor and collects the data from the oscilloscope (implemented together with J. Prats Valero).

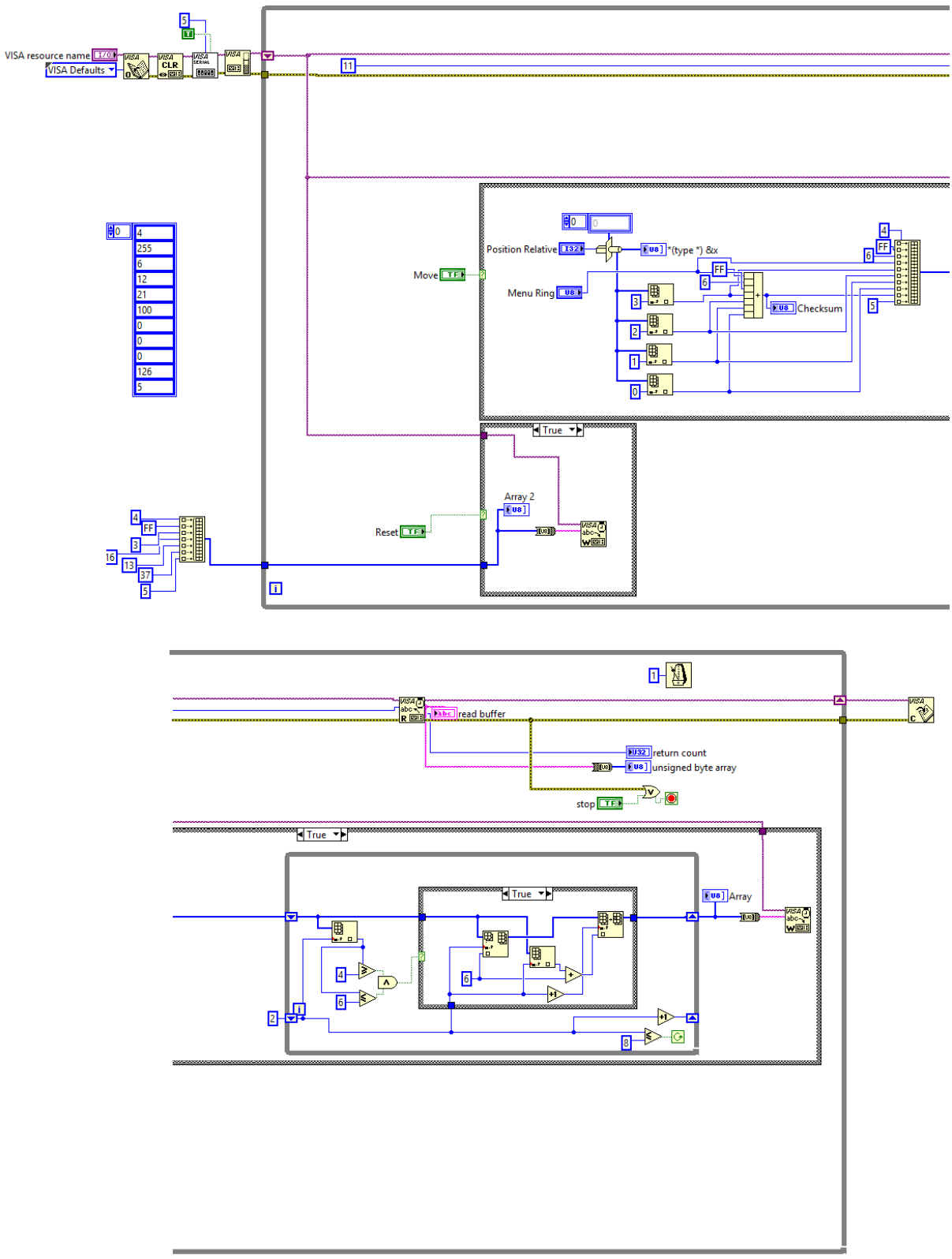


**Figure A.2:** Block diagram of the stepper motor control (implemented together with J. Prats Valero).

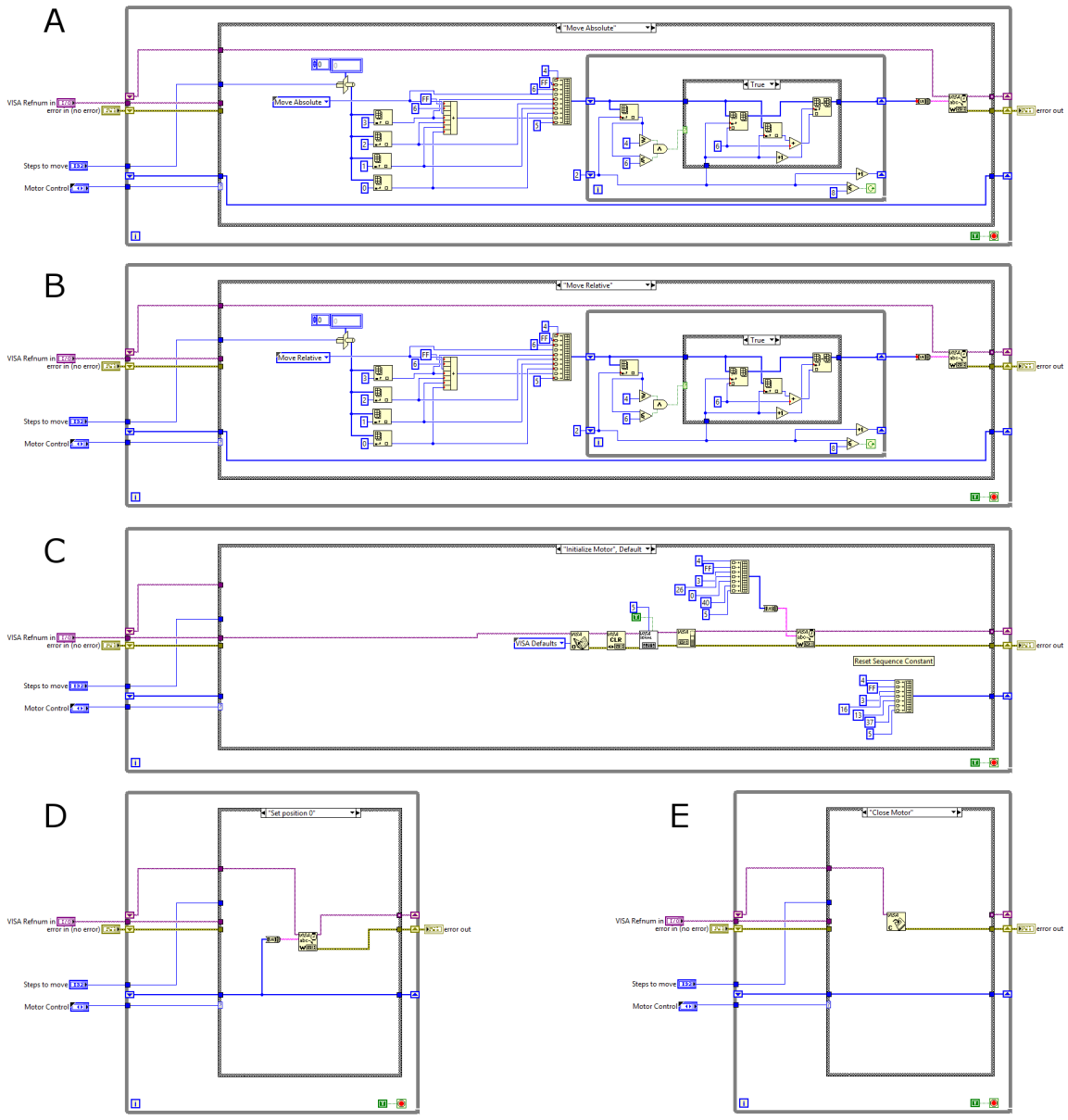


**Figure A.3:** Block diagram of the stepper motor control commands: A) Absolute move, B) relative move, C) initialize motor, D) set position to zero, E) close motor (implemented together with J. Prats Valero).

# Bibliography


[1] Abdul-Khalek, I., Kittelson, D., & Brear, F. (1999). *The influence of dilution conditions on diesel exhaust particle size distribution measurements*. SAE Technical paper. Available online at: http://papers.sae.org/1999-01-1142/ (Accessed on July 21, 2017)

[2] Ahn, K.-H. & Liu, B. Y. (1990a). Particle activation and droplet growth processes in condensation nucleus counter: I. Theoretical background. *Journal of Aerosol Science*, *21*(2), pp. 249–261.

[3] Ahn, K.-H. & Liu, B. Y. (1990b). Particle activation and droplet growth processes in condensation nucleus counter: II. Experimental study. *Journal of Aerosol Science*, *21*(2), pp. 263–275.

[4] Amaral, S. S., de Carvalho, J. A., Costa, M. A. M., & Pinheiro, C. (2015). An overview of particulate matter measurement instruments. *Atmosphere*, *6*(9), pp. 1327–1345.

[5] Andersson, J., Giechaskiel, B., Munoz-Bueno, R., Sandbach, E., & Dilara, P. (2007). Particle measurement programme (PMP): Light-Duty InterLaboratory Correlation Exercise (ILCE LD): Final report (EUR 22775 EN) GRPE-54-08-Rev. 1. Available online at: www.unece.org/trans/main/wp29/wp29wgs/wp29grpe/grpeinf54.html (Accessed on July 20, 2017)

[6] Axmann, H., Bergmann, A., & Eichberger, B. (2013). Measurement of ultrafine exhaust particles using light scattering. In: *Proceedings to the 2013 seventh international conference on sensing technology (ICST)*. IEEE, pp. 937–941.

[7] Buchberger, A. (2015). *Statische Lichtstreuung an Aerosolen* (Bachelor's thesis). Graz: University of technology.

[8] Centre for Atmospheric Science of the University of Manchester. (2016). Condensation particle counters (CPC). Available online at: http://www.cas.manchester.ac.uk/restools/instruments/aerosol/cpc/ (Accessed on July 21, 2017)

[9] Cheng, Y.-S. (2011). Condensation particle counters. In: *Aerosol measurement* (3rd ed.). Hoboken: Wiley, pp. 381–392.

[10] Chu, B. (2007). *Laser light scattering* (reprinted 2nd ed.). New York: Dover.

[11] Collings, N., Rongchai, K., & Symonds, J. P. (2014). A condensation particle counter insensitive to volatile particles. *Journal of Aerosol Science*, *73*, pp. 27–38.

[12] Cresnoverh, M. (2015). *Realisation of a visual based condensation particle counter utilizing bright field technique* (Master's thesis). Graz: University of technology.

[13] European Commission. (2016). C/2016/1393 commission regulation (EU) 2016/427 of 10 march 2016 amending regulation (EC) no 692/2008 as regards emissions from light passenger and commercial vehicles (Euro 6) (text with EEA relevance). Available online at: https://publications.europa.eu/en/publication-detail/-/publication/9a3e0348-f714-11e5-abb1-01aa75ed71a1 (Accessed on July 20, 2017)

[14] Farrauto, R. J., Dorazio, L., & Bartholomew, C. H. (2016). *Introduction to catalysis and industrial catalytic processes*. Hoboken: Wiley.

[15] Friedlander, S. K. (2000). *Smoke, dust, and haze: Fundamentals of aerosol dynamics*. New York: Oxford University Press.

[16] Giechaskiel, B., Cresnoverh, M., Jörgl, H., & Bergmann, A. (2010). Calibration and accuracy of a particle number measurement system. *Measurement Science and Technology*, *21*(4), p. 045102.

[17] Giechaskiel, B., Maricq, M., Ntziachristos, L., Dardiotis, C., Wang, X., Axmann, H., Bergmann, A., & Schindler, W. (2014). Review of motor vehicle particulate emissions sampling and measurement: From smoke and filter mass to particle number. *Journal of Aerosol Science*, *67*, pp. 48–86.

[18] Giechaskiel, B., Wang, X., Gilliland, D., & Drossinos, Y. (2011). The effect of particle chemical composition on the activation probability in n-butanol condensation particle counters. *Journal of Aerosol Science*, *42*(1), pp. 20–37.

[19] Hahn, D. W. (2009). Light scattering theory. Available online at: http://plaza.ufl.edu/dwhahn/Rayleigh%20and%20Mie%20Light%20Scattering.pdf (Accessed on July 21, 2017)

[20] Hannifin, P. (2017). Parker balston filter. Available online at: http://ph.parker.com/us/en/disposable-filter-units (Accessed on August 3, 2017)

[21] Heumier, T. A. & Carlsten, J. L. (2005). Mode hopping in semiconductor lasers: Application note no. 8. Available online at: https://www.newport.com/medias/sys_master/images/images/h4b/h48/8797049585694/AN08-Mode-Hopping-in-Semiconductor-Laser-Diodes.pdf (Accessed on February 18, 2017)

[22] Hinds, W. C. (1999). *Aerosol technology: Properties, behavior, and measurement of airborne particles* (2nd ed.). New York: Wiley.

[23] Ibiden Porzellanfabrik Frauenthal. (n.y.). *Datenblatt für Frauenthaler NT, HT, MK20 Keramiken*. Product sheet.

[24] Jing, L. (2000). Neuer Russgenerator für Verbrennungsrussteilchen zur Kalibrierung von Partikelmessgeräten. *Ofmet Info*, *7*(2), pp. 1–5.

[25] John, W. (2011). Size distribution characteristics of aerosols. In: *Aerosol measurement* (3rd ed.). Hoboken: Wiley, pp. 41–54.

[26] Kittelson, D. B. (1998). Engines and nanoparticles: a review. *Journal of aerosol science*, *29*(5), pp. 575–588.

[27] Kittelson, D. B. (2001). Recent measurements of nanoparticle emissions from engines. *Current Research on Diesel Exhaust Particles*, *9*, pp. 451–457.

[28] Kittelson, D. B., Watts, W., & Johnson, J. (2002). Diesel aerosol sampling methodology-crc e-43: Technical summary and conclusions. Available online at: http://www.me.umn.edu/centers/mel/reports/crce43ts.pdf (Accessed on July 21, 2017)

[29] Kraft, M. & Bergmann, A. (2013). *Betriebsmittel für einen Kondensationskernzähler für Abgase von Verbrennungsmotoren*. AT 514774. Available online at: http://seeip.patentamt.at/NPatentSuche/Details/f708f089-abdc-45c0-aca2-a7fc724d59f9 (Accessed on February 18, 2017)

[30] Kulkarni, P., Baron, P. A., & Willeke, K. (2011). Introduction to aerosol characterization. In: *Aerosol measurement* (3rd ed.). Hoboken: Wiley, pp. 1–13.

[31] Kupper, M. (2016). *iPhoNA Ergebnisse Simulation HT-CPC-Funktionsmuster: Februar 2016*. Internal progress report.

[32] Kupper, M., Kraft, M., Kaczynski, J., & Bergmann, A. (2016). A simulational and experimental attempt for a high temperature condensed nuclei magnifier using organic working fluids. Available online at: https://www.tugraz.at/fileadmin/user_upload/Institute/IES/Pictures/News/EAC2016/eac2016_poster_kupperm.pdf (Accessed on February 18, 2017)

[33] McMurry, P. H. (2000). The history of condensation nucleus counters. *Aerosol Science and Technology*, *33*(4), pp. 297–322.

[34] National Center for Biotechnology Information. (2017a). Entry *Butanol* in the PubChem compound database CID=263. Available online at: https://pubchem.ncbi.nlm.nih.gov/compound/263 (Accessed on February 18, 2017)

[35] National Center for Biotechnology Information. (2017b). Entry *Decan* in the PubChem compound database CID=15600. Available online at: https://pubchem.ncbi.nlm.nih.gov/compound/15600 (Accessed on February 18, 2017)

[36] National Center for Biotechnology Information. (2017c). Entry *Eicosane* in the PubChem compound database CID=8222. Available online at: https://pubchem.ncbi.nlm.nih.gov/compound/8222 (Accessed on February 18, 2017)

[37] Øgendal, L. (2013). Light scattering demystified: Theory and practice. Available online at: http://www.nbi.dk/~ogendal/personal/lho/lightscattering_theory_and_practice.pdf (Accessed on July 12, 2017)

[38] Rongchai, K. & Collings, N. (2012). High temperature condensation particle counter (HT-CPC). Available online at: http://www.nanoparticles.ch/archive/2012_Rongchai_PR.pdf (Accessed on July 21, 2017)

[39] Rongchai, K. & Collings, N. (2013). High temperature condensation particle counter (HT-CPC): A novel device for nanoparticle emission measurement. Available online at: http://www.nanoparticles.ch/archive/2013_Rongchai_PO.pdf (Accessed on July 21, 2017)

[40] Sorensen, C. M., Gebhart, J., O'Hern, T. J., & Rader, D. J. (2011). Optical measurement techniques: Fundamentals and applications. In: *Aerosol measurement* (3rd ed.). Hoboken: Wiley, pp. 269–312.

[41] Spurny, K. R. (2000). Atmospheric condensation nuclei PJ Coulier 1875 and J. Aitken 1880: Historical review. *Aerosol Science & Technology*, *32*(3), pp. 243–248.

[42] Thorlabs. (2016). *Data sheet to laser diode module CPS532*. Product sheet.

[43] Tschöke, H., Graf, A., Stein, J., Krüger, M., Schaller, J., Breuer, N., Engeljehringer, K., & Schindler, W. (2010). Diesel engine exhaust emissions. In: K. Mollenhauer & H. Tschöke (Eds.), *Handbook of diesel engines*. Berlin: Springer, pp. 417–485.

[44] TSI. (2015). Nano enhancer model 3777: Theory of operation, application note 3777-001 (A4). Available online at: http://www.tsi.com/uploadedFiles/_Site_Root/Products/Literature/Application_Notes/3777_Nano_Enhancer_Theory_of_Op_3777-001_A4-web.pdf (Accessed on February 18, 2017)

[45] U.S. EPA. (2009). Integrated science assessment (ISA) for particulate matter: Final report Dec 2009. Available online at: http://ofmpub.epa.gov/eims/eimscomm.getfile?p_download_id=494959 (Accessed on July 20, 2017)

[46] Wang, J., Flagan, R. C., & Seinfeld, J. H. (2002). Diffusional losses in particle sampling systems containing bends and elbows. *Journal of Aerosol Science*, *33*(6), pp. 843–857.

[47] World Health Organization. (2006). Health risks of particulate matter from long-range transboundary air pollution. Available online at: http://apps.who.int/iris/bitstream/10665/107691/1/E88189.pdf (Accessed on July 12, 2017)

[48] World Health Organization. (2013). Health effects of particulate matter: Policy implications for countries in eastern europe. caucasus and central asia. Available online at: http://www.euro.who.int/__data/assets/pdf_file/0006/189051/Health-effects-of-particulate-matter-final-Eng.pdf (Accessed on July 12, 2017)